


Università degli Studi di Milano
Università Cattolica del Sacro Cuore

Scuola di Dottorato in
Fisica, Astrofisica e Fisica Applicata

Dipartimento
Matematica e Fisica

Dottorato di ricerca in
Fisica, Astrofisica e Fisica Applicata

Ciclo XXIV

Time Resolved Optical Measurements on different Carbon Nanotubes Architectures

settore scientifico disciplinare: FIS/03

Tesi di Dottorato di:
Gianluca Galimberti

Coordinatore: Prof. **Marco Bersanelli**
Tutore: Dr. **Gabriele Ferrini**

A.A. 2010-2011

To Anna, Marco, Giovanni, Chiara Maria

Contents

CHAPTER 1

INTRODUCTION

In this thesis I will study ultra-fast electronic dynamics in several architectures of Carbon Nanotubes, unaligned, vertically or horizontally aligned Single Wall and Multi Wall. Charge transfer and linear and non-linear excitonic interactions will be analyzed with time resolved optical techniques.
This thesis represents the initial step of a wide project whose ultimate goal is to improve the efficiency of photovoltaic devices based on Single Wall Carbon Nanotubes (SWCNT) or Multi Wall Carbon Nanotubes (MWCNT). In order to address this aim, heterogeneous systems are considered, in which different Carbon Nanotubes (CNT) architectures are combined with nanoparticles or organic groups. Starting from the basic systems and adding in subsequent steps the different components up to the complete devices, the project is to study, for each step, the optical response.

The choice of CNT is motivated by the fact that in these last twenty years the carbon based materials have been among the main actors of the fundamental match played in the research field on the solar cells and sensor devices. In particular the CNT have marked the expanding world of nanotechnologies.
CNT are tubular structures made by rolled-up graphene layers. The direction along which the graphene foil is rolled defines the CNT chirality, i.e. the rotational and translational symmetry characterizing the carbon tube, and the diameter of the CNT.
The CNT can be SWCNT, with only one graphene layer rolled-up in a tube of diameter ranging from 0.5 nm to 2 nm, or MWCNT which are composed by a multiple-concentric tubes with an outside diameter from 2 nm to 150

nm [1].
Some of the CNT principal properties can be resumed in the following points.

a The circumferential boundary conditions of the electronic wave vector perpendicularly to the CNT long-axis create a peaked structures in the electronic Density of States (DOS), i.e. the Van Hove Singularities (VHS). In the SWCNT these peaked structures are well separated and SWCNT can be either semiconducting or metallic, depending on their diameter and chirality. In the MWCNT, because of the larger diameters, the VHS are energetically much more dense.

b The dynamics of the CNT excited carriers can be described by two approaches. The first one interprets the optical transition in an uncorrelated, single particle model. The other one takes into account the multiparticles correlations. The high Coulomb interaction, characteristic of one-dimensional systems [2, 3] allows an excitonic description of the CNT optical response.

c The CNT electrical conductivity [4] is closely connected with their graphitic structure and with their one-dimensional nature. The result is a high current density that can be carried by these systems. Moreover the CNT geometrical configuration enhances the current direction control. Finally the one-dimensional character is also related to a variety of exotic and intriguing phenomena, like Luttinger liquid and superconductivity behavior, as shown by systems derived by CNT [5].

d CNT are extremely reactive carbon allotropes mainly because of two characteristics: the tubular structure results in an increased π orbital misalignment and the large specific surface area available for the reactions with different functional groups [6].

e The mechanical properties, depending on the strong C=C double bonds exhibit a the high strength and a large elastic modulus.

All these properties are principally connected to the unique CNT one-dimensional character, which makes them extraordinary systems in order to address the technological needs in improving the device performances.
In effect CNT can be employed in a large range of technological applications, from sensor devices to energy storage and photovoltaic cells [4, 6].
In particular concerning the photovoltaic technology, the CNT are materials

suitable to face several among the principal fundamental and technological challanges at stake. These issues can be resumed in the following points:

1 enhancing the device absorbance and extending it to a larger range of the visible frequencies,

2 avoiding the immediate recombination of the photo-excited electron-holes pairs,

3 increasing the photoexcited carries transport to a collecting electrode.

Concerning the first one, the optical transitions between the VHS, in valence and conduction bands, characterizing the CNT optical behavior, can increase the absorbance selectively at visible and near infrared photon wavelengths. Moreover in the excitonic description of the photo-excited SWCNT, recent measurements have revealed Multiple Exciton Generation (MEG) effects corresponding to an increase of absorption in the violet region.
The second issue represents the most crucial challenge for the CNT-based devices. In fact to address it, composite systems have to be considered, in which the charge transfer between heterogeneous components can prevent the electron-hole recombination. Several hybrid materials have been realized with CNT as a crucial component, by exploiting their high chemical reactivity. For examples hybrid materials as SWCNT-TiO_2 revealed a doubled value of the Incident Photon to Charge Carrier Efficiency (IPCE) compared to the pure TiO_2 [6]. In composite systems of MWCNT with nanoparticles electron-donor groups the IPCE have been measured with very promising results, opening the possibility of further improvements through a change of the electron donor groups [7]. The researches around this hybrid compounds, in which CNT are combined with organic and inorganic groups, is growing [6].
Regarding the third issue, the SWCNT reveal outstanding electrical and thermal conductivity [8], and in MWCNT systems the relevant number of shells may promote multi-channel transport pathways, resulting in a further increase of the electrical conductivity [9].
From this summary overview about the state of art on CNT, what emerges is that these systems represent in general a challenge for the physical research and the engineering perspectives.
In order to increase our knowledge on the CNT systems and to enhance their technological application possibilities, a growing effort, in these last years,

has been focused to the improve of chirality selectivity. This is justified by the possibility of studying the CNT optical response under well controlled electronic conditions and by the need of selecting semiconducting or metallic SWCNT, depending on their intended use [4]. Indeed, semiconducting and metallic CNT present different performances, the former used in applications involving charge transfer processes, the latter as interconnecting components because of the conductive character. Although this research is meaningful, an other field of studies has to be addressed. All the optical devices in fact contain CNT ensembles, where often semiconducting and metallic tubes are present and combined with several other systems (nano-particles, molecules, metallic connector, substrate...). Therefore it is essential to undertake an experimental analysis of the complex CNT ensembles as a prior step toward a deeper understanding of the composite systems.
In this framework another choice is necessary. To improve the performances of the photovoltaic systems, the most common and really interesting strategy is advance by trial, combining different component and searching for better response. But clearly this is no longer sufficient. The device efficiency is really an overall response, taking into account the responses of the single components. Therefore a fundamental knowledge of the charge carriers dynamics, charge transfer and charge transport into and between the different parts of the whole system is absolutely necessary in order to achieve the goal of increasing the efficiency, choosing the better configuration and the most useful components.
Therefore the aims of this thesis are as follows.

- The first aim is to undertake an experimental analysis of the complex CNT ensembles.
  The idea developed in this thesis is to consider, as basic systems, CNT ensembles in specific architectures, i.e. CNT bundled unaligned, vertically aligned, horizontally aligned. In fact analyzing the optical behavior of different controlled CNT architectures could allow a rational choice of the better CNT ensembles to be combined with other useful groups in order to increase the device performances.

- The second aim is to more deeply analyze the fundamental dynamics involved in these CNT architectures. The mechanism of interactions between the excited charge carriers will be studied in order to understand how to improve the device efficiency. To catch the charge carriers dynamics in femtosecond temporal regime, time resolved optical tech-

niques, employed here, are certainly powerful tools.
With these techniques the ultrafast charge interactions and inter-tube charge transfer processes in the different CNT architectures can be resolved. In particular this analysis should point out what are the CNT ensembles with a smaller degree of photo-excited electron-hole recombination and with a greater possibility to enhance the photon-current conversion efficiency.
Moreover time resolved measurements allow to distinguish between linear and non-linear responses of the photo-excited CNT systems. In the non-linear regime the temporal evolution of the photo-excited population depends on the square of the population density with two consequences on the photon-current conversion efficiency: the processes of annihilation between two excitonic states corresponds to a non-linear effect, resulting in a lower charge availability for current generation. But the non-linear processes can also be the fingerprint of Multiple Exciton Generation, which represents an important improvement in the absorption efficiency for the solar cells devices [10].

- In the choice of the CNT architectures particular attention will be applied to MWCNT ensembles. Indeed an open challenge is a deeper understanding of the MWCNT behavior. They represent a significantly challenging system and as yet no coherent understanding of their properties exists. The more and more promising performances, shown for example by systems of MWCNT and metallic nanoparticles, require to disentangle key theoretical issues. The transport properties have to be identified. Moreover MWCNT have revealed optical behavior with both HOPG-like and SWCNT-like character. The evidence of the excitonic nature of the charge carrier dynamics in MWCNT can open new theoretical and technological perspectives. The comparison between static optical response and transient optical response of these materials can be crucial in order to address the last two issues.

- The previous item indicates that a large effort has to be done in order to disentangle crucial questions still not clear. Certainly the researches made on the CNT are closely connected to the more general field of the study on carbon based materials and in particular on the graphene and graphite compounds. For this reason at the end of the present work I report significant results obtained on High Oriented Pyrolitic Graphite (HOPG).

- As illustrated at the beginning of this introduction, this thesis represents the initial step of a wider project whose ultimate goal is to consider heterogeneous systems, in which the different analyzed CNT architectures are combined with nanoparticles or organic groups. Starting from the basic systems and adding in subsequent steps the different components up to the complete devices, it will be very useful for each step to study the optical response. On some composed systems, preliminary results have been obtained. CNT composed with ZnO nanorods and CNT decorated by metallic nanoparticles are considered. All these composed systems have applications as photo-sensor devices or as a basis for solar cells.

The outline of the thesis is given below.
In the chapter 2 a description of the experimental set-up is presented. In particular two pump and probe experimental set-ups are illustrated, in which we are able to change the pump fluence in two different ranges (high fluence from 10 to 80 mJ/cm^2 and low fluence from 0.1 to 0.8 mJ/cm^2). The pump and probe are both at 1.55 eV photon energy. Otherwise the pump energies can be tuned from 0.8 eV to 4.1 eV in order to match a resonant transition in the photo-excited CNT electronic structure. Moreover as probe pulse we can use the supercontinuum ranging from 1 eV to 2 eV and allowing a simultaneous measurement in time and frequency domain.
In chapter 3 after an introduction to the SWCNT electronic structure and to the photo-excited charge carrier dynamics in these compounds, the results obtained on unaligned bundles SWCNT, already published in Carbon journal [11], are shown.
In the chapter 4 a brief analysis of the MWCNT electronic properties, evidencing the main issue already open, is reported. Then the measurements on horizontally aligned MWCNT, varying the pump and probe polarizations and with both pump and probe photon energies at 1.55 eV, are discussed (they represent the contents of a paper that has been submitted to ACS Nano). A new result is obtained about the electronic structure of the MWCNT, which presents peaked structures under 3 eV.
In chapter 5 the time resolved measurements on vertically aligned SWCNT and MWCNT are shown, with the pump and probe photon energy at 1.55 eV. At the end of the chapter an optical measurement with supercontinuum as a probe on SWCNT is briefly discussed. The results here obtained lend

support to the conclusions shown in chapter 3.
In chapter 6 the measurements on horizontally aligned MWCNT with a pump energy varying from 0.8 eV to 4.2 eV are shown, along with IPCE measurements in the range from 1 eV to 2 eV. A resonance effect is observed, confirming the presence of peaked structures also in MWCNT system. Moreover an evident difference between the spectra with pump photon energy around 1 eV and those with pump photon energy around 4 eV could be explained with non linear effect as Multiple Exciton Generation. This analysis can reveal if MEG effects are present also on the MWCNT and this result could represent the start step for a big improvement in the photo-voltaic performances of hybrid systems based on MWCNT.
In chapter 7 with the same experimental set-up as in the chapter 6, I present the results obtained on HOPG, revealing an intriguing effect of band gap renormalization (the contents of this chapter have been published on JACS [12]).
In the Conclusion, a summary of the main results is reported. Among these, the preliminary results obtained on hybrid systems as CNTs and ZnO or CNT with metallic nanoparticles is reported and the future research lines are cited.

List of acronyms:
Single Wall Carbon Nanotube(s): SWCNT
Multi Wall Carbon Nanotube(s): MWCNT
Carbon Nanotube(s): CNT
Highly Oriented Pyrolytic Graphite: HOPG
Van Hove Singularity(ies): VHS
Photobleaching: PB
Photoabsorption: PA
Exciton-Exciton Annihilation: EEA
Multiple Exciton Generation: MEG
Incident-Photon-to-electron Conversion Efficiency: IPCE
Density of States: DOS
Radial Breathing Modes: RBM
Band Gap Renormalization: BGR
Traveling Optical Parameter Amplifier: TOPAS
Supercontinuum: SC

Publications
The second part of the chapter 3 is from

G. Galimberti, S. Pagliara, S. Ponzoni, S. Dal Conte, F. Cilento, G. Ferrini, S. Hofmann, M. Arshad, C. Cepek, and F. Parmigiani. The photoinduced charge transfer mechanism in aligned and unaligned carbon nanotubes. Carbon, 49(15):5246-5252, December 2011 [11].

The second part of the chapter 4 has been submitted on ACN Nano Journal in December 2011.

The chapters 5 and 6 represent the contents of papers in preparation.

The chapter 7 is from

S. Pagliara, G. Galimberti, S. Mor, M. Montagnese, G. Ferrini, M. S. Grandi, P. Galinetto, and F. Parmigiani. Photoinduced $\pi - \pi*$ band gap renormalization in graphite. Journal of the American Chemical Society, 133(16):6318-22, April 2011 [12].

CHAPTER 2

EXPERIMENTAL SETUP

2.1 INTRODUCTION

Two different experimental set-ups have been used. The high fluence set up scans the 10 - 40 mJ/cm^2 fluence regime at 1 KHz repetition rate, with a tunable pump photon energy varying from 0.8 eV to 4.1 eV, while the low fluence setup allows 0.1 to 0.8 mJ/cm^2 pulse, at higher repetition rate variable from 54.3 MHz to single shot and at a photon energy of 1.55 eV.

2.2 HIGH FLUENCE SETUP, TUNABLE PUMP ENERGY

2.2.1 The laser systems

The light source of this setup is an amplified Ti:Sapphire laser system (Fig. 2.1). The pulses wavelength is centered around 790 nm with a temporal width about 150 fs and energy per pulse $\approx$ 600 μJ. The repetition rate is 1 KHz, therefore the output power is 0.6 W, and the peak power is 4×10^9 W. As shown in Fig. 2.2 in the right part, the beam coming from the regenerative amplifier is splitted by a beam splitter in two different beams, the pump and the probe. 70% of the original beam is sent through the pump line, as much more power is required to operate the parametric amplifier, while the remaining 30% is really sufficient for the probe line.

2.2.2 The pump and probe lines

The probe line described in Fig. 2.2 is long enough to have the same length as the pump line. In effect the transit of the pump through the Traveling Optical Parameter Amplifier (TOPAS) corresponds to more than 2 m of travel

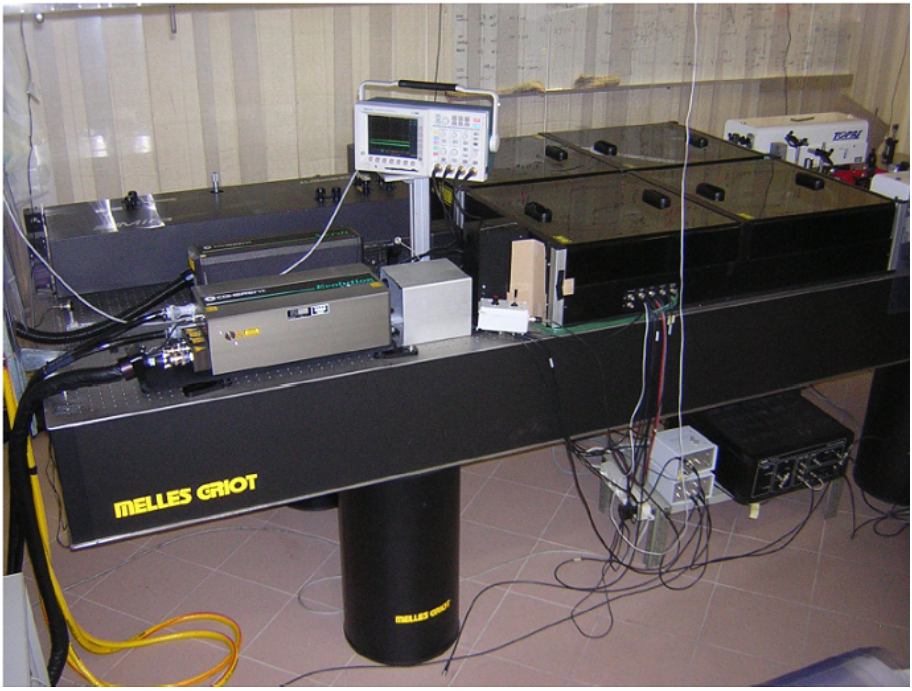

Figure 2.1: Photo of the system used to generate the source beam of the high fluence setup.

and this distance has to be covered by the probe beam. The probe line is characterized by a sledge which allows to change significantly the probe line length, when the temporal coincidence between pump and probe has to be found. The polarizer with the $\lambda/2$ plate allows the control of the probe fluence and polarization direction. A final lens of 200 mm reduces the probe spot size to a diameter of about 10 μm.
The pump line is more complex. The first step of the pump line is a TOPAS. This is the key component of the setup because it allows a tunable pump photon energy. The input of the TOPAS is a 300 - 350 mW pulsed beam at 790 nm and with 150 fs pulses, the output is tunable from 1150 nm to 1600 nm, the time length of the pulses is 150 fs and the power is about 40 mW. All the optical elements after the TOPAS have been chosen in order to minimize

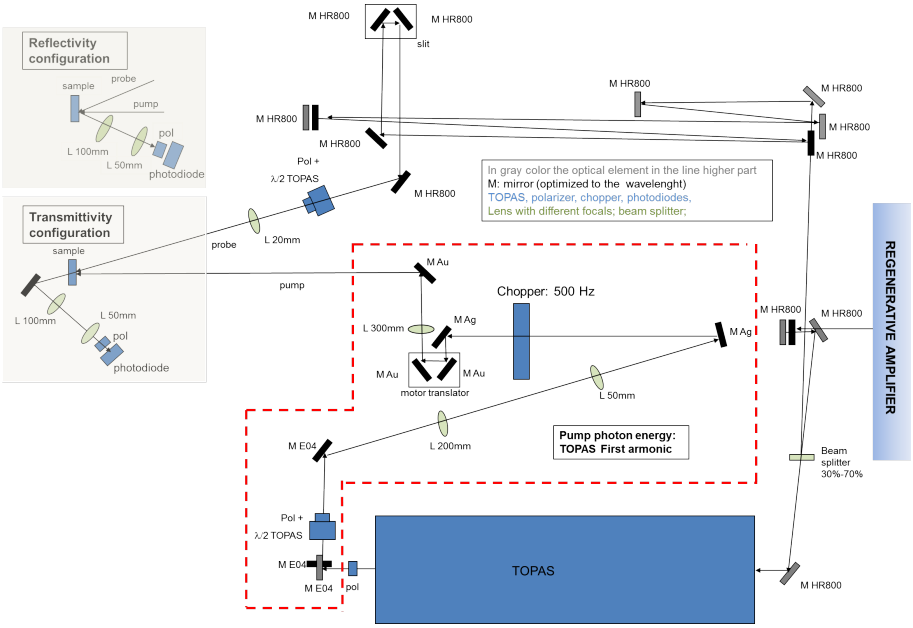

Figure 2.2: Schematic representation of the high fluence pump-probe setup.

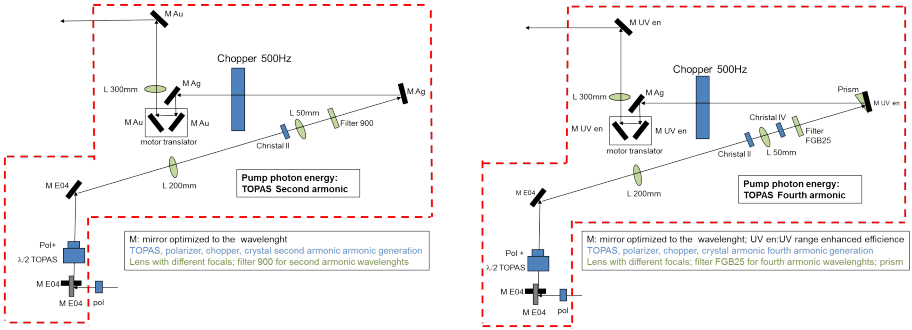

Figure 2.3: Schematic representation of the first part of the high fluence pump-probe line for the second and the fourth harmonics generation.

the power losses, as indicated in Fig. 2.2 and in Fig. 2.3.
The polarizer with the $\lambda/2$ plate allows the control of the pump fluence and enables the transit of the signal pulse, stopping the idler component.
When the pump photon energies correspond to the TOPAS first harmonics, no other non-linear crystal is necessary.
In order to obtain the second harmonic a non-linear crystal is placed in the focus of a telescope of two lenses. Then a filter cuts the first harmonic and lets pass only the second harmonic.
For the production of the fourth harmonic another non-linear crystal is necessary. Moreover a suitable filter reduces the second harmonic fluence and a dispersive prism splits the fourth harmonic from the second harmonic beam.
In the case of the fourth harmonic, a set of mirrors with UV enhanced reflection efficiency are used. This type of measurements is really complicated by the need to avoid excessive losses that could over reduce the pump fluence. In general the high non linearity of this set up system requires great care in carrying out the experiment.
The last lens on the pump line makes the diameter of the pump spot on the sample about 80 μm, larger than the probe case, facilitating the spatial coincidence.

2.2.3 Time resolved reflectivity and transmittivity configurations

The pump pulse, whatever the harmonic is, passes through the chopper element, that reduces the number of pulses from $1000/sec$ to $500/sec$. The chopper is synchronized with the acquisition electronic system. In this way the photodiode acquires one transmitted/reflected probe pulse without excitation of the pump and one transmitted/reflected probe pulse from the sample excited by the pump pulse, making then the difference between the two signals. In the left part of the Fig. 2.2 the two final steps of the pump-probe line for the transient transmittivity and for the transient reflectivity are reported.

2.3 LOW FLUENCE SETUP, SUPERCONTINUUM PROBE

2.3.1 The laser systems

In the low fluence setup the light source is a Ti:Sapphire mode-locked laser oscillator. The output pulses wavelength is centered at 790 nm (1.55 eV) and the temporal length is of about 120 fs FWHM. The output energy is 50 nJ

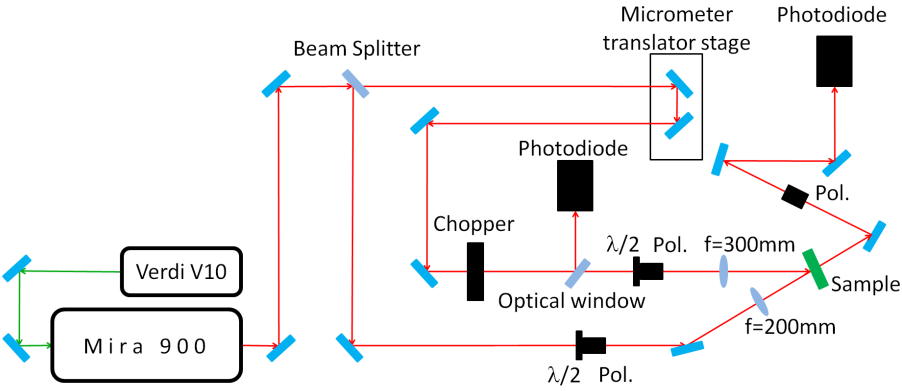

Figure 2.4: Schematic representation of the low fluence pump-probe setup.

per pulse at a repetition rate variable from 54.3 MHz to single shot. With respect to the high fluence set up, the pump fluence is lower, ranging from 0.1 mJ/cm^2 to 0.8 mJ/cm^2. The use of a tunable repetition rate laser source allows us to avoid the experimental problem of average heating effects. The pump fluence ranges from 0.1 mJ/cm^2 to 0.8 mJ/cm^2. Low-pump-fluence pulses were obtained at a repetition rate of 540 kHz to maximize the signal-to-noise ratio. The high repetition rate of this setup allows a lock-in acquisition resulting in a high resolution in the $\Delta T/T$ spectra with respect to the high fluence setup. Moreover a much wider delay time spectra acquisition is also possible.

2.3.2 The pump and probe lines

The low fluence setup schematic representation is shown in Fig. 2.4. The cavity dumper output beam is split into two different beams, the pump and the probe, via a T=70% R=30% beam splitter. The pump beam passes through a delay line composed by a mirror assembly mounted on a computer controlled micrometer translator stage. The minimum displacement step of the translator stage is 0.1 μm, resulting in a delay time resolution of 0.66 fs. The next step of the pump line is a mechanical chopper, followed by a half-waveplate and a polarizer, that allow the variation of the pump polarization and intensity. A f = 300 mm lens is then used to focalize the

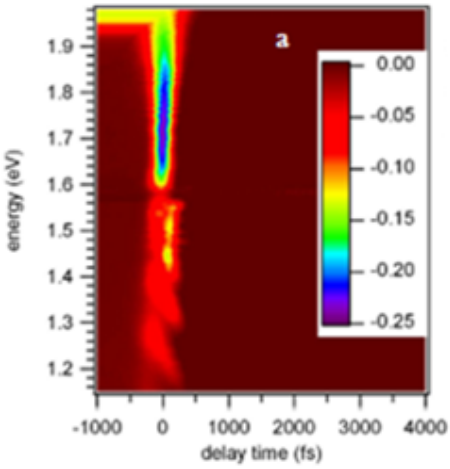

Figure 2.5: Characterization of the supercontinuum pulse.

beam on the sample. (As in the high fluence setup, the sample is not perfectly on the pump beam focus, in order to facilitate the spatial superposition of the pump and the probe beams.) A fused silica optical window is located between the mechanical chopper and the waveplate-polarizer assembly in order to collect its small reflection via a photodiode and feed the lock-in amplifier reference with the correct chopper modulation phase. The probe beam passes through a half-waveplate and polarizer assembly that allow to change the probe polarization and intensity on the sample.
A f = 200 mm lens is used to focalize the probe beam.

2.3.3 Time resolved reflectivity and transmittivity configurations

The reflectivity or transmittivity signal from the photodiode is sent to the lock-in amplifier input. As mentioned before, a pump beam reflection modulated by the mechanical chopper is used as reference phase for the lock-in. The reflectivity or transmittivity signal is modulated by the presence or absence of the pump beam, and the amplitude of this modulation is proportional to the change of the sample transmittivity. Since the modulation is in phase with the chopper reference, it is easily extracted by the lock-in amplifier and

acquired by a National Instruments M-Series interface board. The acquisition software holds these values and the corresponding delay times since all the desired scans over the selected delay time window are performed. The acquired values are then automatically averaged and the result is logged together with the delay times. This averaging procedure further increases the signal to noise ratio. The static transmittivity is assumed to be the DC component [10] of the transmittivity signal which is also detected by the lock-in amplifier. This acquisition system allows the detection of a 1×10^{-5} $\Delta T/T$ signal.

2.3.4 The supercontinuum generation

The generation of the supercontinuum corresponds to a production of a large spectrum light pulse, obtained by the propagation of high power excitation pulses into a medium with non-linear optical properties. The medium is a photonic crystal fiber. In this fiber the dielectric index of the cladding is smaller than the index of the core, because of holes in the cladding along all the fiber length. By engineering the geometry of these holes the dispersion properties can be useful modified. The four mechanisms, which produce the supercontinuum generation, are the self phase modulation, the scattering Raman process, four wave mixing and the solitonic fission [13, 14]. In Fig. 2.5 the characterization of the supercontinuum signal (see also Chapter 2 [14, 11]) is reported. The photon energies contained in the pulse are ranging from 1.0 eV to 2 eV, the temporal width is about 120 fs. In the range from 1.0 eV to 1.5 eV, a noise is present connected with the solitonic structure of the pulse.
The fiber is mounted on a swing that allows to change the tilt to facilitate mating. For focusing the laser beam on the fiber we used a aspherical lens with focal length 4.5 mm, mounted on a translator to optimize focus position. This parameter is essential for a good light alignment into the the fiber. After the fiber, there is an achromatic doublet with a focal length of 10 mm and optimized for working wavelengths in the range of 650-1050 nm. This is also mounted on a micrometer translator, in order to parallelize the laser beam.

CHAPTER 3

EXCITON DYNAMICS IN UNALIGNED AND VERTICALLY ALIGNED SINGLE WALL CARBON NANOTUBES

3.1 SWCNT ELECTRONIC STRUCTURE AND DYNAMICS

3.1.1 SWCNT electronic structure

The SWCNT electronic structure is well described in several text books and scientific papers. In this first part of chapter 3, I want to stress only some crucial aspects.
The SWCNT electronic structure combines in itself two different characters: at the same time solid and near-molecular behavior. In fact a single carbon nanotube can be thought as a single layer of graphene rolled up along one particular direction [15]. As depicted in Fig. 3.1 the circumferential direction (perpendicular to the CNT long-axis) corresponds to the numbers (n_1, n_2), multiplying the graphene basis vectors $\mathbf{a}_1$ and $\mathbf{a}_2$. The (n_1, n_2) parameters define the CNT chirality, i.e. the direction in the graphene plane along which the layer is rolled up. There are two particular directions, evidenced in Fig. 3.1, armchair and zigzag, and the others, between these two, correspond to chiral SWCNT.
The (n_1, n_2) defines also the cylinder diameter according to this formula $d = \frac{a}{\pi}\sqrt{n_1^2 + n_1 n_2 + n_2^2}$. The diameter ranges from a fraction of a nanometer to several nanometers.

As shown in Fig. 3.2, the structure of a SWCNT is specified by the chiral vector $\mathbf{C}_h = n_1\mathbf{a}_1 + n_2\mathbf{a}_2$ along the circumferential direction and by the translator vector $\mathbf{T} = \frac{2n_2+n_1}{d_R}\mathbf{a_1} - \frac{2n_1+n_2}{d_R}\mathbf{a_2} = t_1\mathbf{a}_1 + t_2\mathbf{a}_2$ along the CNT

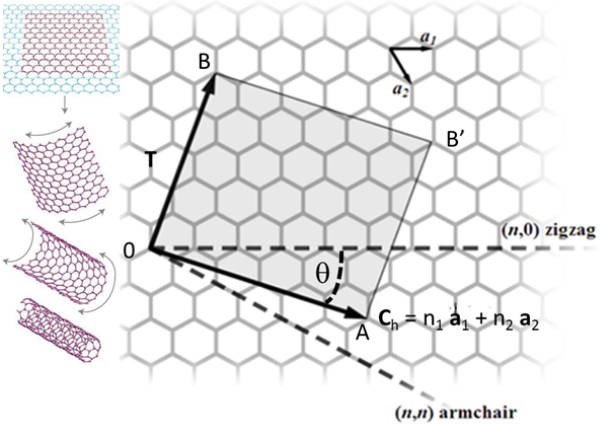

Figure 3.1: In a single graphene layer the circumferential line and the axis line (perpendicular to the circumferential)are indicated. The principal directions, armchair and zigzag, and an example of a chiral direction are reported. In left part the rolled-up layer is shown [15].

long-axis, where d_R is the greatest common divisor of $(2n_1 + n_2)$ and $(2n_2 + n_1)$ for a (n_1, n_2) nanotube. $OAB'B$ is the bi-dimensional unit cell of the nanotube. Starting from these elements the corresponding bi-dimensional reciprocal space can be defined. In particular it is useful to define $\mathbf{k}_\parallel$ or $\mathbf{k}_z$ as a reciprocal lattice vector parallel to the CNT long-axis and $\mathbf{k}_\perp$ as the reciprocal lattice vector along the circumferential direction. Along the tube circumference the vector $\mathbf{k}_\perp$ is quantized according to the boundary condition

$$m \cdot \lambda = |C_h| = \pi \cdot d \Leftrightarrow k_{\perp,m} = \frac{2\pi}{\lambda} = \frac{2\pi}{|C_h|} \cdot m = \frac{2}{d} \cdot m \qquad (3.1)$$

where m is an integer taking the values $-q/2 + 1, ...0, 1, ..., q/2$ and q is the number of graphene hexagons in the nanotube unit cell. The k_z can assume continuous values.

The CNT electronic properties closely depend on (n_1, n_2). The CNT electronic structure can be calculated in the zone folding approximation: the dispersion of the electronic band for the k-line parallel to the CNT axis is calculated from the energy dispersion of the graphene along the same direction,

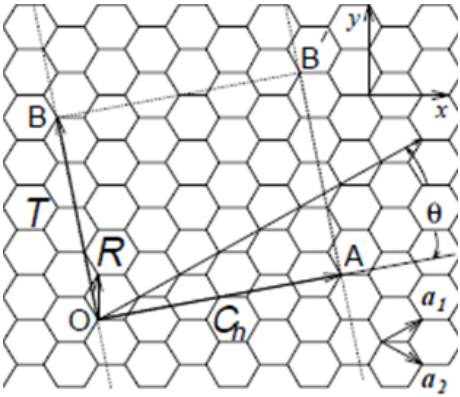

Figure 3.2: In a single graphene layer the chiral vector and the transaltor vector are shown [1].

whereas, along the circumference, the boundary conditions on the electronic wave functions enable only a discrete number of $k_\perp$ values each corresponding to a definite m value.
In particular, SWCNT can be either metallic or semiconducting, metallic if one allowed k-line passes through the K-point in which the DOS is different from zero at the Fermi Level, semiconducting if the k-line does not contain the K-point (Fig. 3.3).
In Fig. 3.4 an example of band dispersion is reported. Along the k_z line

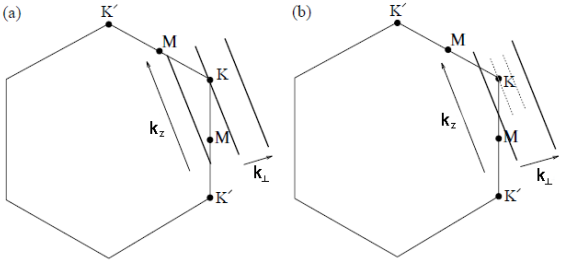

Figure 3.3: (a) Metallic case. (b) Semiconducting case

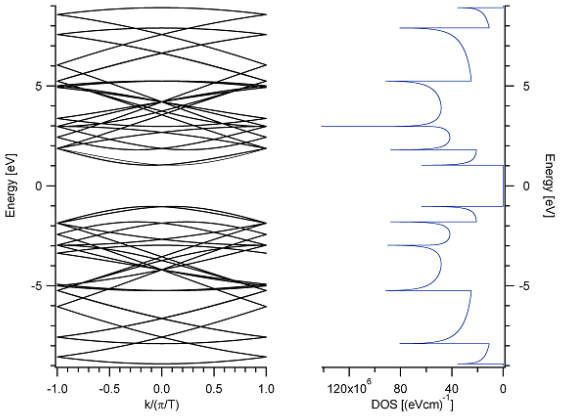

Figure 3.4: Example of CNT band structure in zone folding approximation. In the left energy dispersion versus the k vector parallel to the CNT axis. In the right panel the corresponding DOS characterized by the VHSs.

(parallel to the CNT long-axis) the energy dispersion is that of the HOPG, but for the same k_z values there are different quantized $k_\perp$, each corresponding to a different band. When the dispersion curve reveals a flat behavior, in the DOS a peak appears. Therefore the same k_z line is characterized by several peaked structures, called Van Hove Singularities (VHS). The density of states for one dimensional electronic bands is given by

$$n(E) = \frac{2}{q|k_\parallel|} \sum_i \int dk_z \delta(k_z - k_i) |\frac{\partial E(k_\perp, k_z)}{\partial k_z}|^{-1} \tag{3.2}$$

where k_i is given by $E - E(k_\perp, k_z) = 0$. As reported in [1], according to some calculations, the derivative can be expressed as

$$|\frac{\partial E(k_\perp, k_z)}{\partial k_z}|^{-1} \propto \frac{|E|}{\sqrt{(E)^2 - E_m^2}} \tag{3.3}$$

where $E_m \propto |3m - n_1 - n_2|$. It is clear that the the density of state diverges for some energy values.
A VSH in the valence band with a definite m number corresponds to a VHS in the conduction band with the same m number. The optical transition

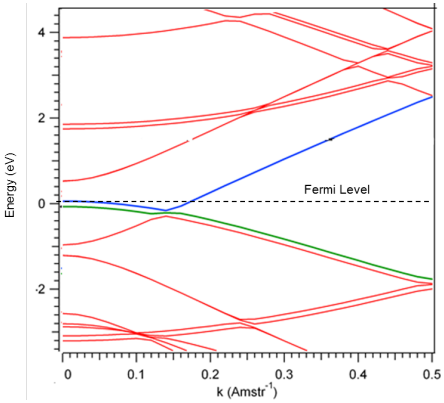

Figure 3.5: Band structure ab-initio calculation (with ABINIT program) of the (5,0) SWCNT. The presence of a band at the Fermi level shows that this SWCNT is a metallic tube even if the zone folding approximation expects a semiconducting behavior.

between them are favored according to the dipole selection rules [1]. The high density of states for different energies represent a favorable condition for the presence of excitonic states. We will return to this point later, but now we underline that these excitonic states can reveal a localized character, quite as in the molecular energetic levels [16, 17].
This mingling of solid and molecular properties makes the SWCNT extremely interesting systems from a theoretical and a technological point of view.
This analysis based on the zone folding approximation represents a too strong approximation when the tube has a small diameter and the wall curvature has to be considered. For example in a zone folding approximation for the (5,0) SWCNT, a semiconducting behavior with zero DOS at Fermi energy level is predicted, but the curvature effect [18, 19] leads to strong $\sigma - \pi$ hybridization, modifying the band structure and giving a metallic character to this CNT. In Fig. 3.5, for a (5,0) CNT, the ab-initio calculation, that I performed with Abinit program (http://www.abinit.org/) during the present thesis work, takes into account many-body effects. The metallic behavior evidences that the curvature produces different results compared to the zone folding approximation.
The many body character affects also the description of the SWCNT optical response. In SWCNT the excitonic effects are strongly increased, first of

all because of the reduced dimensionality which in general favors a smaller separation between the photo-excited electron and the corresponding hole and an increase of the Coulomb force. The second reason, typical of the SWCNT case, is connected to the configuration of the electric field which holds together the electron and hole pair. In effect the electric field is located principally outside the tube where the dielectric screening is reduced and therefore the interacting force is increased. [3].
The absorption spectra have been simulated taking into account the excitonic effect revealing a significative modification of the response compared to the case without many-body effects and the experiments confirm this result [3, 20, 21, 18, 19]. Moreover in the last years the time resolved optical measurements are described in terms of excitonic behavior [22, 23, 24].
In this thesis the excitonic description will be principally assumed.

3.1.2 SWCNT electronic dynamics

Several research activities have been devoted to the problem of the photo-excited carrier dynamics in SWCNT. Focusing on photon excitation energies in the infrared-visible range, I try to resume this vast theoretical and experimental field identifying two main topics:

1− the two models by which the photo-excited charge carrier dynamic is described, single particle and excitonic model;

2− the two optical responses to the exciting pulse, i.e. linear and non-linear, observed in the excitonic model.

1− The studies up to 2004 focus principally on the electron-electron and electron-phonon dynamics. In particular time resolved photoemission measurements have been interpreted introducing an internal thermalization of the photoexcited electron gas due to the electron-electron scattering processes. The excited electron population has a kinetic energy ranging from 0 eV (just above the Fermi level) up to 2 eV, revealing a corresponding decay time which decreases from 200 fs to 10 fs. A much slower electron-phonon interaction, described with the two temperature model, develops on a picosecond time scale producing a cooling of the thermalized electron gas [25, 26].
In a more general framework, as described in ref. [1], the charge carriers dynamics can follow different relaxation paths. When the second VHS, in semiconducting CNT, is involved, the intraband scattering process takes place in

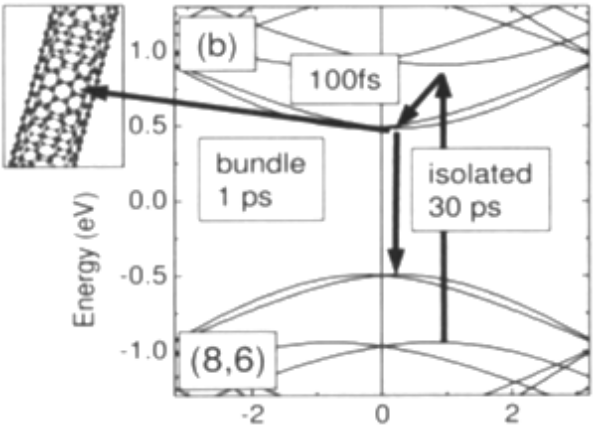

Figure 3.6: Scheme of the possible charge carriers dynamics in SWCNT [27]

100 fs, bringing the excited electron from second to the first VHS in conduction band. The decay time from this first VHS is of the order of some pico-seconds. In particular in time resolved photoluminescence experiments [28, 24] on isolated CNT, a decay time of several tens of ps have been measured [24]. When the CNT are not isolated, also inter-tube charge carriers relaxation channels open [25, 1, 29], with a time constant of about 1 ps. This intertube decay process is considered a reason of the photoluminescence quenching, together with the various impurities constituting traps states for the excited electron-hole pair [27].
A summary diagram is reported in Fig. 3.6.
Since about 2005, the results of the time resolved optical measurements have been interpreted taking into account the interaction between electron and hole, within an exciton model framework [22, 30, 16, 31, 32, 33].

In this context in semiconducting SWCNT the electron excited in conduction band and the corresponding hole in the valence band represent a unique excited state, which can be described as shown in Fig. 3.7. In the left part of the figure, the indexes -1,-2,-3 indicate the m numbers characterizing the discretized $k_\perp$ and the associated VHS in conduction band, the indexes 1,2,3 the corresponding VHS in valence band. An optical transition can promote one electron to the ith VHS in conduction band from the correspondent VHS

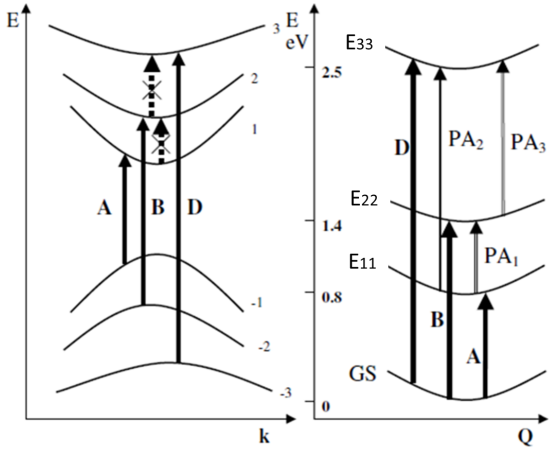

Figure 3.7: At the left part the simplified band dispersion for a semiconducting tube. In the right part the correspondent excitonic transition, described in the text [22].

in valence band. Therefore an excitonic state is built with an electron in the conduction VHS and the hole in the valence VHS and this state is defined E_{ii}. For example transition A in the left panel of the Fig. 3.7 is from the ground state to E_{11} excitonic state. The transition between ground state (GS) and E_{ii} excitonic state correspond to Δm=0. These transitions are possible, according to the selection rules, with the electric field polarization parallel to the carbon nanotube axis [1].
The photo induced transition between E_{ii} and E_{jj} levels corresponds to the excitation of an electron from a VHS already in an excited state in conduction band to an higher state and the creation of the hole in the corresponding valence subband (see for example the transitions of Photo-Absorption PA_i in the right panel of the Fig. 3.7). Also this transition PA_i corresponds to Δm=0 and can take place with field polarization parallel to CNT axis. The photon energy can be transferred to the system, according to the conservation laws, only taking into account the whole e-h exciton system and its binding energy.
Other possible transition are E_{ij} in which the electron and the hole of the excitonic state belong to VHS (in conduction and valence band respectively) with different m number and therefore the Δm$\neq$0. The transition generat-

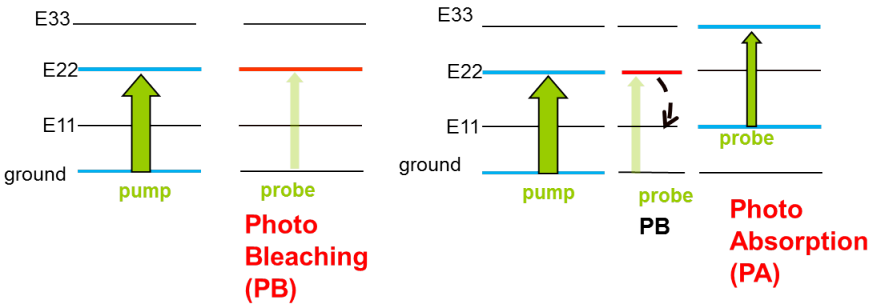

Figure 3.8: In the left panel the picture of photo bleaching process. In the right panel the photo absorption process.

ing such excitonic states are possible only with an electric field polarization perpendicular to the CNT axis.

As described in Fig. 3.8 the possible processes connected to the excitonic transitions can be a photo-bleaching (PB) and a photo-absorption (PA) process. In the photo-bleaching process, shown in the left side of Fig. 3.8, the pump pulse promotes charge carriers from the ground to an excited state and the absorption of the probe pulse, at the same photon energy, decreases because of the final state filling effect, with a corresponding enhancement of the probe transient transmission values. In the second process, described in the right part of Fig. 3.8, the pump pulse creates excitons from ground to an higher excitonic states, as, for example, E_{22}, that suddenly, in a few tens of femtoseconds, decay on the E_{11} state, as described in literature [30]. If the probe polarization complies with the selection rules and the photon energy is resonant with the transition $E_{11} \rightarrow E_{33}$, the probe pulse promotes excitons from the E_{11} state to a higher excitonic level E_{33}. In the transient transmission spectra this process corresponds to an enhancement of the probe absorption (photo-absorption effect).

2− The processes described above are linear processes, in which the fluence of the exciting pulse is proportional to the excited density population.

Non-linear excitonic processes have been studied and well described in literature on spatially confined systems, as nanocrystal [34]. In the last years they have been measured also on the carbon nanotubes, with very promising perspectives [10]. Generally, in the non-linear excitonic processes, the descrip-

tion of the carrier population dynamical evolution involves a quadratic term of the population itself. For example under high exciton density conditions the population temporal behaviour is determined by the scattering process between two excitons, called exciton-exciton annihilation (EEA), which creates a single exciton state at a higher energy allowed by the conservation laws. In SWCNTs different models have been studied in order to describe the EEA event. Principally it is a rate equation approach containing an exciton population quadratic term [2]. Other methods are developed in which the probability of scattering between two excitons is proportional to the mobility of the exciton along the carbon nanotube axis [35]. Finally the EEA has been described also trough an exponential function with a characteristic time around 1 ps [10].
Non-linear processes are also involved when the correspondence between one exciting photon and one excited exciton is lost. In this case one photon at energy n-times larger than the first level E_{11} can generate n-excitons on the E_{11} levels. The Multiple Exciton Generation (MEG) is realized. The great importance of these studies is connected with the efficiency of the photon-current conversion in photovoltaic devices.
In the next paragraphs I will consider the linear processes described above on the bundled unaligned SWCNTs. In the next chapters on aligned MWCNTs and SWCNT I will discuss also the non-linear phenomena.

3.2 BUNDLED UNALIGNED SWCNT

3.2.1 Abstract

In this section the paper published in Carbon journal is reported [11].
Using time-resolved reflectivity measurements on unaligned and aligned bundled single wall carbon nanotubes with a pump energy of 1.55 eV, quasi-resonant with the second Van Hove Singularity of semiconducting tubes, a positive sign of the transient reflectivity is detected in unaligned nanotubes. In contrast a negative sign is detected in aligned nanotubes. This discovery addresses a long-standing question showing that in unaligned nanotubes the stronger intertube interactions favor the formation of short-lived free charge carriers in semiconducting tubes. A detailed analysis of the transient reflectivity spectral response shows that the free carriers in the photo-excited state of semiconducting tubes move towards metallic tubes in about 400 fs.

3.2.2 Introduction

In these last years a significant effort has been addressed to identify the carbon nanotube (CNT) orientation most suitable for CNT-based electronic devices. The performance of these devices, ranging from field effect transistors to nano-photovoltaic systems, strongly depends on non equilibrium carrier transport and on charge transfer mechanisms from semiconducting to metallic nanotubes [8, 15, 36, 37] Therefore, a correct understanding of intertube interactions and charge transfer mechanisms is a key issue for a significant advance of the technology of CNT-based devices. Here, by performing time resolved reflectivity measurements on aligned and unaligned single wall carbon nanotube (SWCNT) bundles we unveil the physical mechanism at the basis of the charge transfer from semiconducting to metallic tube. A large number of studies have shown that at equilibrium [38, 39, 40], the intertube interactions in SWCNT bundles are weak and similar to the coupling between adjacent graphene planes in 3D crystalline graphite or the interball coupling found in solid C_{60}. This weak intertube coupling is dominated by the van der Waals interactions with a nonzero covalent bonds contribution. This behavior has a significant influence on the vibrational [38, 39, 41, 42, 43, 44] and electronic states of carbon nanotubes [45, 46, 47].
Nonetheless, the effect of the intertube interactions in bundled CNTs, relevant to charge transfer mechanisms, remains unclear. A number of theoretical studies have been performed to address the effects of intertube interactions in bundled nanotubes. These studies suggest that the dominating intertube van der Waals interactions, while promoting the nanotube bundling, have the effect of energy shifting and broadening the optical transitions. In particular, the broadening of the absorption spectral features, in bundled nanotubes, originates from the intertube electronic properties perpendicular to the tube axis. Moreover, the curvature of the nanotube wall in CNTs induces a downshift of the conduction bands by enhancing the $\sigma-\pi$ hybridization [39, 27, 48] Although these mechanisms are well understood, the absence of a strong luminescence in CNT bundles remains unclear. This is a key question concerning the charge transfer processes since it has been argued that the non-radiative channel, quenching the radiative channel (fluorescence), can originate from possible charge transfer from the semiconducting to the metallic tubes [27] Nevertheless, this is still an open question and optical spectroscopies in the time domain, with a suitable time resolution, might reveal the changes of the optical properties induced by nonradiative mechanisms [25, 22, 33, 30].

Recently, this kind of experiments have been performed on CNT with a well defined chirality. However, making CNT with a defined structure and with intertube interactions not affected from other atomic species (contaminants, surfactants or molecule) still remains a major challenge [29, 49] In this frame-

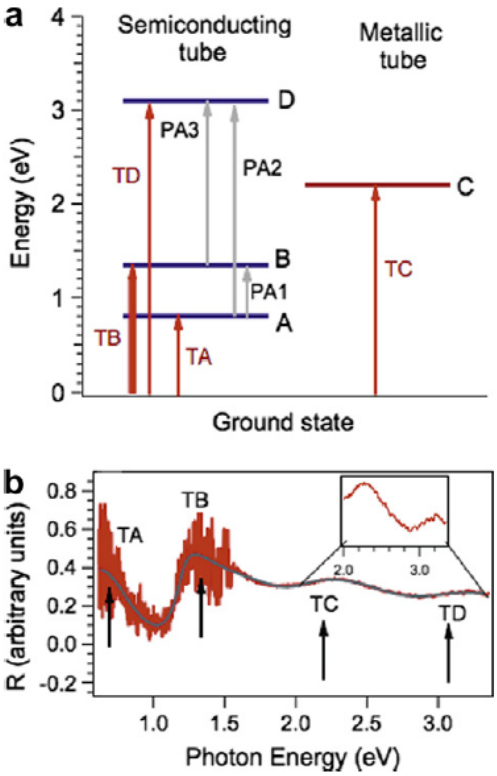

Figure 3.9: (a) Schematic electronic structure of both semiconducting and metallic unaligned bundled SWNT. The energy positions of the bands (A, B, C and D) are estimated by the reflectivity spectrum reported in (b). The arrows TA, TB, TC and TD indicate the transitions from the ground state to unoccupied states. PA1, PA2 and PA3 refer to photoabsorption processes induced by the laser pump nearly resonant with TB transition.

work, in order to highlight the dependence of the charge transfer channel on the bare intertube interactions, time-resolved reflectivity measurements in

the femtosecond timescale have been carried out on aligned and unaligned SWCNT bundles with different chirality, grown in the same experimental conditions [50]. The experiments have been performed by using a conventional one-color pump-probe set-up (pump and probe both at 1.55 eV), along with a novel pump-probe set-up in which the probe is a broadband white light pulse (supercontinuum) [14]. By using the supercontinuum pulse as a probe, it is possible to achieve spectral resolution: this allows to detect in the frequency domain the relaxation dynamics of the carriers excited through a resonant absorption transition into the conduction band. By setting the pump frequency quasiresonant with the second Van Hove singularity of the carbon compounds a positive sign of the transient reflectivity is detected in unaligned nanotubes, whereas a negative transient reflectivity is detected in aligned nanotubes. This important difference demonstrates that in unaligned nanotubes the stronger intertube interactions favor the formation of shortliving free charge carriers in semiconducting tubes that decay through a charge transfer nonradiative process toward the metallic tubes. A detailed analysis of the transient reflectivity spectral response shows that the free carriers in the photoexcited state of semiconducting tube transfer to the metallic tubes in about 400 fs. The important results emerging from our findings are: (i) bundling and unalignement induce strong intertube interactions yielding a free-electron mobility of the excited carriers in semiconducting tube; (ii) the photoinduced charge delocalization favors the charge transfer from semiconducting to metallic tube.

3.2.3 Experimental

Sample preparation

Aligned and unaligned CNT bundles were synthesized in the Analytical Division of the TASC-IOM-CNR laboratory, where the catalyst depositions and Chemical Vapor Deposition (CVD) processes are performed in an ultra high vacuum experimental apparatus (base pressure $< 1 \cdot 10^{-10} mbar$). In this apparatus it is possible to control the chemical state of the catalyst (before and after the growth) via X-ray photoemission spectroscopy (XPS) and to monitor all the CVD parameters (i.e. precursor gas purity, pressure and pressure gradient, sample temperature, gas fluxes, etc.). Pure aligned and unaligned SWNT bundles were grown via CVD technique by using the same CVD parameters [50]. Only the precursor gas pressure has been changed in order to obtain aligned and unaligned bundles. SWCNT were characterized

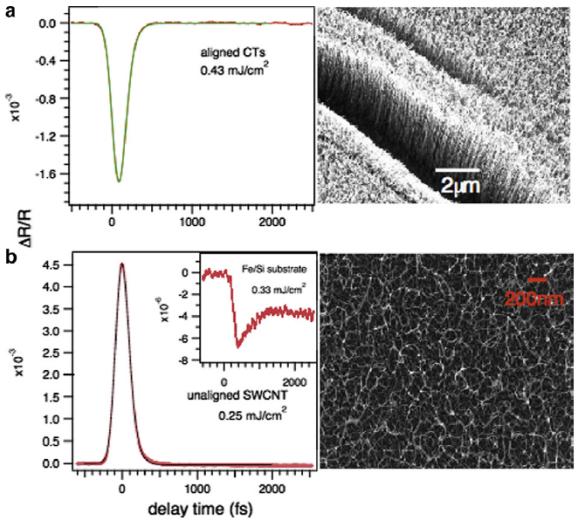

Figure 3.10: One-color ($h\upsilon$ = 1.55 eV, fluence of 0.2 mJ/cm^2) transient reflectivity spectra collected on both aligned (a) and unaligned (b) SWCNT. The TR spectrum of the substrate is also reported (inset in (b)) in order to exclude its contribution on the TR signal of unaligned bundles. The spectra of unaligned and aligned SWCNT are well fitted with one exponential curve convoluted with a gaussian (representing the laser pulsewidth). The SEM images are also reported.

by microRaman and SEM measurements (see 3.2.6 paragraph).

Laser system Time-resolved reflectivity

Time resolved measurements have been performed with two laser systems, to investigate different pump fluence regimes. An amplified 1 kHz Ti:Sapphire laser system, producing 150 fs, 1.55 eV light pulses, permits to excite the samples with pump fluences in the range 10-100 mJ/cm^2, whereas with a cavity-dumped Ti:Sapphire oscillator, producing 120 fs, 1.55 eV light pulses, the samples have been excited with pump fluences ranging from 0.1 to 0.8 mJ/cm^2. The incidence angle of the laser pump is about 5° with respect to the sample normal direction. This laser system is also equipped with a supercontinuum generation unit [14], to collect TR spectra with both time and frequency resolution, with an energy range from 1.1 to 2.0 eV. (see

paragraph 3.2.6).

3.2.4 Results and discussion

Because of the one-dimensional nature of the electronic bands, the density of states of SWCNT exhibits a series of characteristic Van Hove Singularities (VHSs) detectable in the near IR and visible spectral regions (Fig. 3.9a). Fig. 3.9b shows a representative reflectivity spectrum, collected on unaligned SWNT bundles. Four structures located at about 0.8 eV (TA), 1.35 eV (TB), 2.2 eV(TC) and 3.1 eV (TD) are clearly detected. The features TA,TB and TD are assigned to the inhomogeneously broadened interband optical transitions from the valence subbands to their respective conduction subbands in semiconducting SWCNT as schematically shown in Fig. 3.9a. Instead, the band TC is assigned to an interband transition in metallic SWCNT [25, 22]. When the photon pump energy is resonant with a VHS, a transient photobleaching is usually expected in the one-color time-resolved optical spectroscopies. Absorption of the pump pulse excites electrons into conduction band, creating holes in the valence band. Until these carriers relax, transient filling effects on the final states are observed. For the photobleaching effect, the transient signal is positive in transmittivity and negative in reflectivity (such as in the absorption) [22, 33, 30, 51]. Fig. 3.10 shows the one-color transient reflectivity on unaligned SWCNT bundles (Fig. 3.10b) together with the spectrum acquired on aligned SWCNT bundles (Fig. 3.10a). While the negative TR signal on aligned SWCNT reveals the photobleaching process in agreement with literature [22, 33, 30, 52], the positive TR signal on unaligned SWCNT is the fingerprint of a new relaxation channel that increases the reflectivity. We attribute the positive TR signal to a free-electron like character of the carriers excited in the B band of semiconducting tubes. The TR negative sign of the substrate including the catalyst nanoparticles suggests that the contribution of the substrate (inset in Fig. 3.10b) is negligible. Moreover, the different orientation of the laser polarization with respect to the CNT axis in the unaligned and aligned bundles can not justify a different sign in the transient optical response. At this pump photon energy, the VHS optical transitions are excited only with an electric field parallel to the tube axis. Due to the near-normal incidence of the laser pump, we expect strong excitation mainly in the unaligned bundles, where the laser polarization, in a statistical sense, can be found parallel to the tube axis [53]. However, also in the vertically aligned bundles the excitation of the VHS transitions

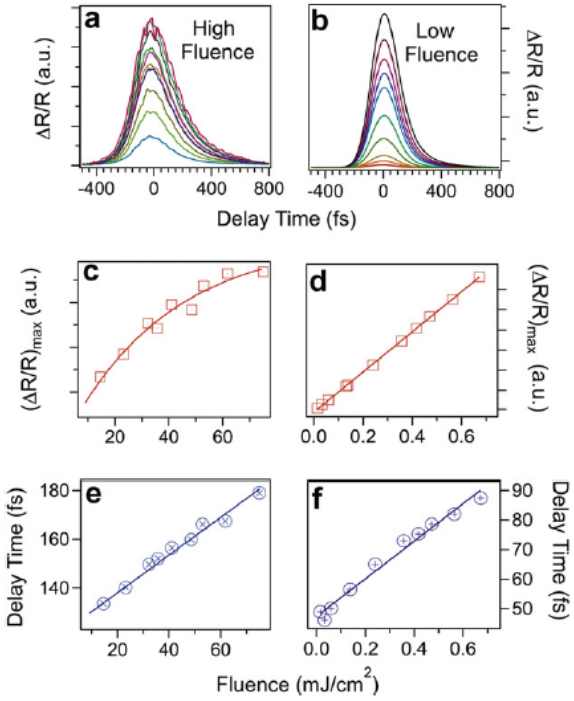

Figure 3.11: (a and b) One-color transient reflectivity spectra collected on unaligned SWCNT bundles by changing the pump laser fluence. The spectra are collected at different fluence regimes: high fluence (from 10 to 80 mJ/cm^2) and low fluence (from 0.1 to 0.8 mJ/cm^2). (c and d) Pump fluence dependence of the maximum of the transient reflectivity spectra and (e and f) of the relaxation time, estimated by fitting the spectra with one exponential decay curve convoluted with a gaussian. The solid curves represent the best fit of these data with a linear (d, e and f) and an exponential curve (c).

cannot be excluded even at near normal incidence, considering the imperfect alignement of the CNT that prevents them to be perfectly normal to the incident electric field of the pump beam. As a consequence, the laser pump excites the same VHS transition in both samples, the only difference being the excitation intensity. In agreement with literature [53, 54, 1], due to the dependence of absorption efficiency on the relative CNT - electric field orientation, we conclude that only the density of the photoexcited carriers and

not the sign of the transient reflectivity is affected by the excitation of the VHS transitions. The positive TR sign can be rationalized considering that in the aligned SWCNT the intertube interactions are comparable with the van der Waals interactions among the graphene layers in graphite, whereas in unaligned SWCNT the intertube interactions are changed by both the curvature and the spatial anisotropy. In particular, the modified intertube interactions induce an overlap between the $\pi - bands$ of adjacent tubes by allowing the delocalization of the electrons photoexcited in the VHS. Usually, the presence of VHS or, alternatively, of the strongly bound excitons inhibit the free-carrier mobility yielding a localization of charge carriers on a length scale of $\approx 100nm$ [16]. The modified intertube interactions in the unaligned bundles, on the contrary, delocalize the carriers excited in these bands, inhibiting the photobleaching and favouring the free-electron mobility. The delocalized charge optical response is expected to behave as a Drude electron gas. In this case the imaginary part of the dielectric function can be written:

$$\varepsilon_2 = \omega^2\tau/\omega(1+\omega^2\tau^2) \tag{3.4}$$

where $\omega_p^2 = (Ne^2)/(\varepsilon_0 m)$ is the plasma frequency, N the carrier density, e and m the charge and the mass of the electron, e_0 the vacuum dielectric constant. For an ideal free-electron metal, the reflectivity approaches unity below the plasma frequency. Above the plasma frequency, the metal is transparent and the reflectivity decreases rapidly with increasing frequency. When free-electron carriers are created by the laser pump, the Drude-like behaviour of the carriers enhances the reflectivity. Therefore, the transient reflectivity, which is the reflectivity signal of the probe modified by the presence of the laser pump, is positive and it can be directly related to the CNT orientation (aligned or unaligned SWCNT bundles). To further support this finding, TR measurements on films with different CNT density, length and substrates have been performed. The TR positive signal shows no dependence on these sample characteristics (see paragraph 3.2.6). Moreover, to rule out spurious effects such as nonlinear processes and sample damage the experiments have been repeated varying the laser fluence from 10 to 80 mJ/cm^2 and from 0.1 to 0.8 mJ/cm^2 (shown in Fig. 3.11a and b). In Fig. 3.11c and d the dependence of the maximum of the TR signal on the pump laser fluence is shown. For pump fluence ranging from 0.1 mJ/cm^2 to 0.8 mJ/cm^2 (Fig. 3d), TR signal linearly increases with fluence, whereas the saturation effect takes place (Fig. 3.11c) above 40mJ/cm^2.

To estimate the carrier density excited (N(E)) in the $\pi*$ band the following

formula can be used [55]

$$\int_0^\infty N(E)dE = (1-R)F\alpha/h\upsilon \tag{3.5}$$

where $h\upsilon$ is 1.5 eV, the reflectivity R = 0.4 and the absorption coefficient $\alpha = 2 \times 10^5\ cm^{-1}$. Therefore at a laser fluence F = $40mJ/cm^2$, the initial photo-carrier density is $20 \times 10^{21} cm^{-3}$. This value is comparable (including non-linear optical processes that become important at this high pump fluence) with the carriers density from 0 to 1 eV ($6.5 \times 10^{21} cm^{-3}$) observed in graphite [55]. This result proves that at the pump intensity used in this experiment and at a photon frequency quasi-resonant with the second VHS a very high density of carriers can be excited in the π^* band of the semiconducting tube. To obtain information about the dynamics of the excited state carriers, the spectra reported in 3.11a and 3.11b are fitted with exponential curves convoluted with a Gaussian representing the laser pulse width.

The TR spectra of both aligned and unaligned SWCNT bundles are well fitted by one exponential curve with a decay time ($\approx 100fs$) comparable with the laser pulse width (3.11a and 3.11b). Moreover, the dependence of the relaxation time on the fluence (3.11e and 3.11f) excludes radiative recombination processes [31]. This result is in agreement with the dynamics of the bundles reported in literature [33, 1] and it can be justified considering that in CNT the carrier dynamics strongly depend on the excited state. In particular, when electrons are excited in the first VHS of the semiconducting tubes (A) the lifetime is $\approx 1ps$ [33], whereas in the second (B) the lifetime is $\approx 130fs$. Meanwhile, the luminescence from isolated CNT has a longer lifetime ($\approx 30ps$) than that on unaligned bundles. This can be explained considering that the carriers excited into the second VHS relax very rapidly to the band gap of the semiconducting tube (intraband scattering). Then in isolated nanotubes the electron and the hole recombine across the band gap, whereas in bundled nanotubes the tunneling into nearby metallic tubes or into semiconducting tubes with a smaller band gap turns off the luminescence. The excited carriers in the metallic tubes, as shown in time-resolved photoemission experiments [25, 56, 26], lose their energy rapidly, therefore quenching the luminescence of CNT bundles efficiently [25, 56, 26, 27]. In this experiment, the presence of a fast relaxation channel on unaligned SWCNT bundles confirms that electrons are excited in the second VHS. This behavior is compatible with a free character of the excited carriers in the semiconducting tubes that favors the charge transfer towards metallic tubes and semicon-

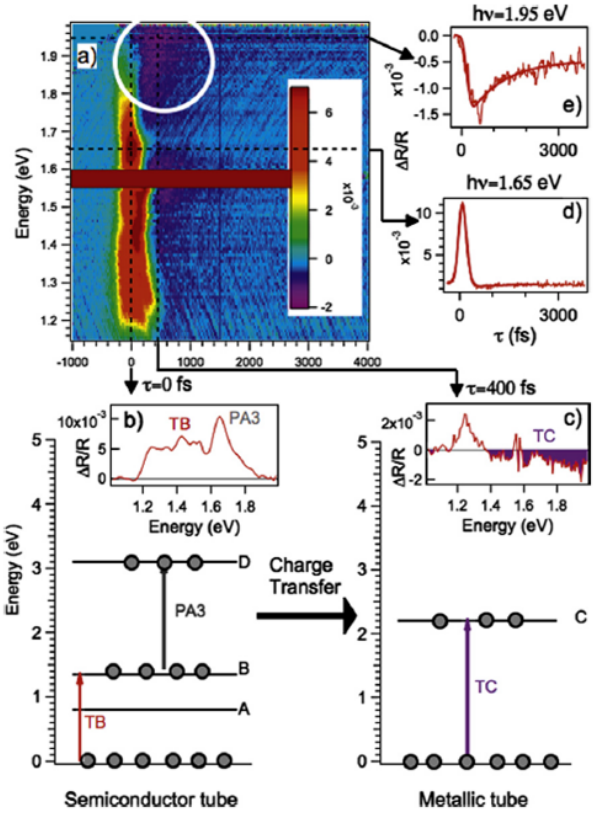

Figure 3.12: (a) 3D image of the time resolved reflectivity spectrum collected on unaligned SWCNT bundles by using the supercontinuum probe and a $h\upsilon = 1.55$ eV pump. On the bottom a scheme of the charge transfer. At $\tau = 0$ the carriers are excited in the B band of the semiconducting tubes by the laser pulse. Some of the carriers are excited by the same pulse into the D band (PA3 transition in (b)). After 400 fs (c), carriers in the excited-states of semiconducting tube move towards the metallic tube and a negative TR signal due to TC transition appears in the probe spectrum. On the right, image profiles extracted at photon energies of the probe corresponding to PA3 (d) and TC transitions (e).

ducting tubes with smaller energy gap. The mechanisms so far described can be understood in more details looking at the optical response of photoexcited

SWNT in both the time and frequency domains. In these experiments the pump photon energy is 1.55 eV, whereas the probe covers an energy range from 1.1 to 2 eV (Fig. 3.12a). In SWCNT, a photobleaching process is usually correlated with different photoabsorption channels [22]. In particular, carriers excited in the B band rapidly decay on A giving rise to PA1, PA2 and PA3 photoabsorption processes, where carriers are photoexcited from A to B (PA1), from A to D (PA2) and from B to D (PA3) (see Fig.3.9a). By considering the reflectivity spectrum collected on bundled SWCNT sample (Fig. 3.9b), the photoabsorption channels could appear at 0.6 eV (PA1), 2.3 eV (PA2) and 1.7 eV PA3). The 3-dimensional (3D) TR spectrum is shown in Fig. 3.12a together with different extracted line profiles at fixed delay times (Fig. 3.12b and c) or photon energies (Fig. 3.12d and e). The broad red line at about $h\nu = 1.55$ eV (Fig. 3.12a) covers the laser pump scattered by the sample. The image profile at delay time $\tau = 0$ fs (Fig. 3.12b) shows two positive features. The first, broadband and centered at 1.4 eV, is the TB transition; its positive signal confirms the free-electron character of the excited carriers discussed in one-color TR at 1.55 eV. This band appears structured due to the noise in the measurement. The second positive feature at 1.65 eV is ascribed to the PA3 photoabsorption process.
Electrons are excited by the probe from the B and to the D band in the pulsewidth. This picture is confirmed by the lack of relaxation processes before the photoabsorption (PA3 appears at $\tau = 0$ fs in Fig. 3.12b). To analyze the relaxation dynamics of the PA3 channel, the line profile at $h\nu = 1.65$ eV is shown (Fig. 3.12d). From the fitting with exponential curves, the PA3 decay results very fast and after a pump-probe delay of about 400 fs, a negative TR signal with a long decay time is observed. In the 3D spectrum, a dark-purple zone corresponding to a negative TR signal is evident around the point $h\nu = 1.95$ eV, $\tau = 400$ fs (Fig. 3.12e). This negative zone extends up to 2 eV and appears after $\tau = 400$ fs. In the reflectivity spectrum of Fig. 3.9b, the feature at about 2 eV has been ascribed to the TC transition in the metallic tubes. As the pump photon energy at 1.55 eV is unable to excite any transition in the metallic tube, the presence of this photobleaching channel, which implies a filling of the C band, is the evidence of a charge transfer from the semiconducting to the metallic tube. These observations can be interpreted considering that the pump laser excites a population in the B band of the semiconducting SWCNT. Some of the delocalized carriers are excited by the same pump pulse in the D band. By calculating the area of the TR spectrum at $\tau = 0$ fs (Fig. 3.12b), the intensity of the PA3 photoabsorption

process can be estimated resulting in a value comparable with that of free-carriers excited in the B band. Because of their mobility, the carriers transfer from the semiconducting to the metallic tube within 400 fs, giving rise to a photobleaching of the TR when the probe photon energy is nearly resonant with the TC transition. The lack of the B and C band photobleaching in the reflectivity spectrum reported in literature [22] confirms that the two mechanisms are mutually exclusive and that only the free-electron behavior of the excited carriers permits to switch on the semiconducting- metallic charge transfer. The slow relaxation dynamics of the C photobleaching (about 2 ps, see image profile at $h\nu = 1.95$ eV of Fig. 4e) agrees with the dynamics of the photobleaching channels reported in literature on SWCNT [30]. To perform a quantitative study of the TR spectrum at $\tau = 0$ fs, a differential dielectric function model has been fitted to the time resolved reflectivity data,

$$\Delta R/R = (R_{ex}(\varepsilon_{ex}) - R_{eq}(\varepsilon_{eq}))/R_{eq}(\varepsilon_{eq}), \tag{3.6}$$

where R_{ex}, ε_{ex}, R_{eq}, ε_{eq} are the excited and equilibrium reflectivity and dielectric function, respectively.
The ε_{eq} has been calculated by fitting Req (Fig. 3.9b) with a sum of Lorentz oscillators which represent the transitions TA, TB, TC, TD. According to the differential dielectric function model, for reproducing the transient reflectivity spectrum, it is necessary to modify the fitting parameters of the Lorentz oscillators or to add new oscillators. In our case, to properly fit the differential spectrum $\Delta R/R$ (Fig. 3.12b),we need to add one Drude and one Lorentz oscillator, the first to take into account the free-electron mobility of the photoexcited carriers in the B band, and the second to reproduce the PA3 photoabsorption at 1.7 eV. The presence of solitonic structures in the supercontinuum affects the fitting accuracy of the line profile at $\tau = 0$ fs with the differential model. However it is possible to extrapolate a value for the plasma frequency in the Drude model 6.3 of $4 \times 10^{15} sec^{-1}$ (2.5 eV), that corresponds to a carrier density of $4 \times 10^{21} cm^{-3}$. This value, compared with the carrier density excited by the laser pump $2 \times 10^{20} cm^{-3}$ for a pump fluence of 0.2 mJ/cm^2 (3.3), confirms the delocalized character of the carriers excited in the B band of semiconducting tubes.

3.2.5 Conclusion

Time-resolved reflectivity measurements demonstrate that intertube interactions in bundled unaligned SWCNT induce a free-electron character to

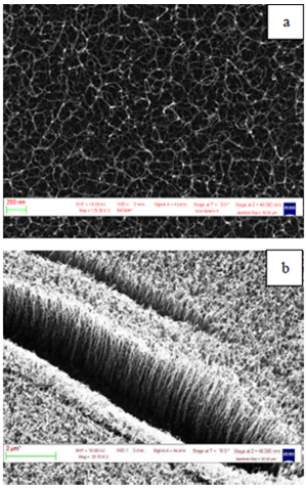

Figure 3.13: SEM measurements on SWCNT bundle unaligned (top) and bundled vertically aligned (bottom)

the photoexcited carriers favoring a charge transfer from semiconducting to metallic tube. This finding paves the road to new and important technologies closely connected to the intra- and inter-tube conductivity.

3.2.6 Materials on line of the Carbon paper

Sample Preparation

Aligned and unaligned CNT bundles (Fig. 3.13a, Fig. 3.13b) were synthesized in the Analytical Division of the TASC-IOM-CNR laboratory, where the catalyst depositions and CVD processes are performed in an ultra high vacuum experimental apparatus (base pressure $< 1 \times 10^{-10}$mbar). In this apparatus it is possible to control the chemical state of the catalyst (before and after the growth) via Xray photoemission spectroscopy (XPS) and to monitor precisely all the CVD parameters (i.e.: precursor gas purity, pressure and pressure gradient, sample temperature, gas fluxes, etc.). The CVD processes were done on thin films of 150 nm thermally grown SiO_2 support layer on polished n-type Si(100) substrates, on 10 nm thick Al_2O_3 support layers grown via magnetron sputtering on the previous film and on 30 nm

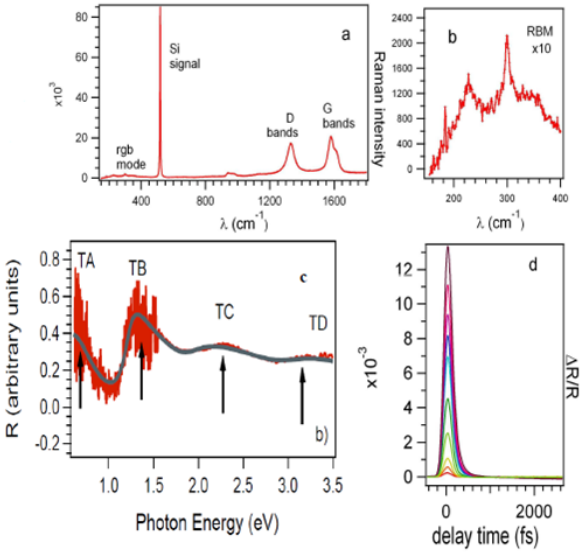

Figure 3.14: On bundled unaligned SWCNT Raman spectra with RBG mode (top), Static Reflectivity (left bottom) and Transient Reflectivity (right bottom)

TiN films grown via ALD on Si substrates. We used Fe as catalyst, and acetylene as the precursor gas. Fe catalyst films were deposited in-situ by sublimation from heated filaments (Aldrich, 99.9 per cent purity) at a growth rate of ∼0.6 nm/h. The deposition rate was obtained from the attenuation of the photoemission peaks of Al 2p for the Al_2O_3 support layer and Si 2p for the SiO_2 support layer. Samples were clamped between two Ta contacts and heated by direct heating. Fe films were always monitored by XPS to detect the presence of contaminants. We operate in the following parameters window: ∼0.6-8 nm Fe film thickness, $4 \times 10^{-8} - 10^{-3}$ mbar C_2H_2 pressure (≈4 sccm) and 580-600°C growth temperature. A typical CVD route consists of a preliminary out-gassing of the substrate at 550-600°C, followed by Fe deposition at room temperature, and successive ramping-up to the chosen growth temperature. The aligned CNT carpets were grown in the above experimental apparatus using the same experimental conditions but increasing significantly the growth pressure (C_2H_2 flux during the CVD process:

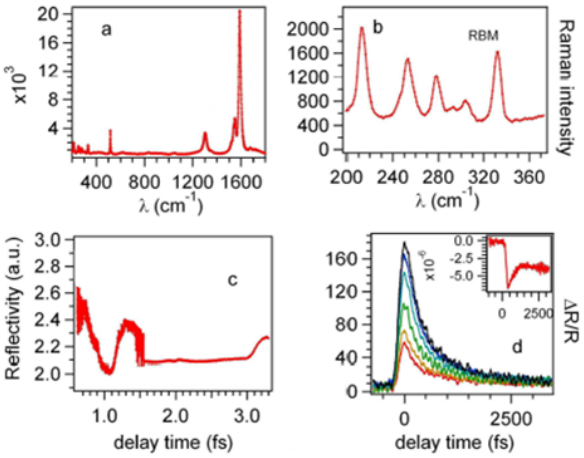

Figure 3.15: On bundled unaligned SWCNT (second thicker sample) Raman spectra with RBG mode (top), Static Reflectivity (left bottom) and Transient Reflectivity (right bottom

50sccm). In order to exclude extrinsic effects, residual solvents or chemical treatments during the CNT synthesis have been avoided.

Sample Characterization

All samples were characterized ex-situ, by Scanning Electron Microscopy and Raman spectroscopy. In particular, the transient reflectivity measurements were collected on two kinds of unaligned SWNT samples, more and less dense. In Fig. 3.14a the microRaman spectrum carried out on the more dense unaligned CNT sample with a He-Ne laser source (λ=633 nm) is shown. The D and G bands and the signal from the Si substrate are marked. The prominent D band in the thicker sample is usually ascribed to defects. The prominent RBMs (Fig. 3.14b) are detected at 225 cm^{-1} and 300 cm^{-1}. By using the relation $\omega_{rgb} = B + \frac{A}{d^n}$ with A = 234 cm^{-1} and B = 10cm^{-1}, the estimated diameters of the nanotubes [57] are between 0.8 nm and 1.2 nm, with an average value of about 1nm. This result is consistent with the static reflectivity measurement. In fact by following the Kataura scheme [15] it is possible to evaluate the diameter from the energy positions of the features

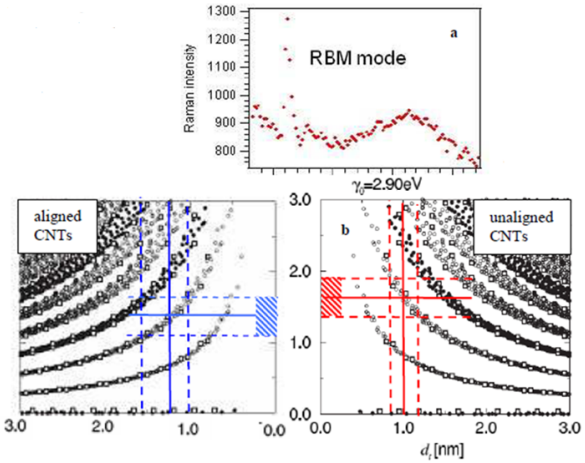

Figure 3.16: RBM for the bundled vertically aligned SWCNT (top panel). In the bottom, Kataura scheme for bundled vertically aligned SWCNT and bundled unaligned SWCNT.

in the reflectivity spectrum (Fig. 3.14c) ascribed to interband optical transitions from various valence subbands to their respective conduction subbands (see also Fig. 3.12a). Therefore the complex energy structure of this sample, related to the presence of different diameter and chiralities, is described by the reflectivity spectrum peaks, in which energy transitions are clearly recognizable and a photobleaching effect can be predictable for a pump photon energy of 1.5eV resonant with the second transitions. The one-color transient reflectivity (1.55eV) at different pump fluences is shown in Fig. 3.14d: the signal results to be positive for all the analyzed samples, excluding a photobleaching effect. As reported in the paper, the transient reflectivity indicates that the relaxation dynamics are determined by a single, very fast, process. In Fig. 3.15 the characterization of the less dense CNT unaligned samples is reported. The Raman spectrum with a He-Ne laser source (λ=633 nm) (Fig. 3.15a) indicates a better quality of these samples. The G band is more structured whereas the D band is less intense. As reported in Fig. 3.15d, the transient reflectivity is still positive, suggesting that the sign of time resolved reflectivity is independent on the SWCNT density and on the presence of defects. In Fig. 3.15b the RBM modes are in an interval comparable to that of the more dense sample and corresponding to a diameter range between

0.8nm and 1.2nm. Also in this case an average diameter is about 1.0nm [57]. In Fig. 3.15c the static reflectivity shows the same prominent structures of Fig. 3.14c. The flatness of the spectrum in the 2-3eV range has to be ascribed to the weakness of the signal due to the lower density of the sample. In this case, the transient reflectivity spectrum results well fitted by two relaxation dynamics. The faster dynamic time is consistent with the value reported for the more dense SWCNT samples, while the slower dynamic can be influenced by the substrate (inset in Fig. 3.15d) In In Fig. 3.16a we report the microRaman characterization of the vertically aligned SWCNT (SEM image in Fig. 3.13b) with a He- Ne laser source (λ=532 nm), evidencing the presence of the RBM. One sharp peak and one more large structure are shown, corre-

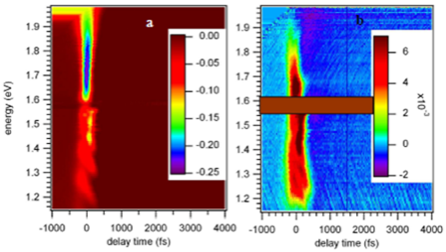

Figure 3.17: Supercontinuum characterization in the left. ΔR/R on SWCNT unaligned with Supercontinuum as a probe in the right

sponding in this case to a diameter range from 1 to 1.6nm, larger than in the unaligned case. Using the Kataura scheme in order to compare in particular the second vHS transition in the two cases, we obtain the scheme reported in Fig. 3.16b. It is evident that in both cases, with a pump and probe energies of 1.55eV, we should expect a photobleaching effect and it is what we get in the case of aligned CNT, but not on the unaligned CNT sample.

Experimental Set Up

The one-color time-resolved reflectivity (TR) measurements have been performed with an amplified Ti:Sapphire laser system producing 150 fs, 1.55eV light pulses. The output energy of 600mJ/pulse at 1 kHz of repetiton rate permits to excite the sample with pump fluences ranging from 10-100 mJ/cm^2. The supercontinuum [14] probe reflectivity measurements have been per-

formed with a cavity-dumped Ti:Sapphire oscillator producing 120 fs 1.55eV light pulses. The output energy is 50 $nJ/pulse$ at repetition rates tunable from 5.43 MHz to a single shot. By setting the repetition rate at 100 kHz, the samples have been excited with pump fluences ranging from 0.1 to 0.8 mJ/cm^2. In Fig. 3.17b the transient reflectivity measurements by using a supercontinuum as a probe is reported along with the supercontinuum characterization (Fig. 3.17a). The supercontinuum pulse has been characterized by performing a two-photon absorption experiment in a ZnSe crystal. By comparing the two spectra, it is clear that the structures, below 1.55eV, are solitonic structures characteristic of the supercontinuum.

CHAPTER 4

VAN HOVE SINGULARITIES AND EXCITONIC EFFECTS ON HORIZONTALLY ALIGNED MULTI WALL CARBON NANOTUBES

4.1 INTRODUCTION

In the present chapter, I describe the optical transient response of an horizontally aligned MWCNT system. The property of this architecture is to allow a very high control on the angle between the light polarization direction and the CNT long-axis and this possibility unveil new and important perspectives as described in the next paragraphs. In general the MWCNT represent a very intriguing system with several open theoretical issues. At the same time they are also very promising materials in a large field of technological applications.
Like in the SWCNT case, several works are devoted to the study of the MWCNT, in scientific papers and text-books. In this first part of the present chapter, as in the previous for the SWCNT, I do not want to discuss all the aspects of this large research field, but only to underline some crucial points that frame our research.

4.2 AN INTRODUCTION TO THE MWCNT SYSTEM

4.2.1 MWCNT: open issues

One of the most evident character of the MWCNT is the complexity of the electronic structure, because of the simultaneous presence of several nested

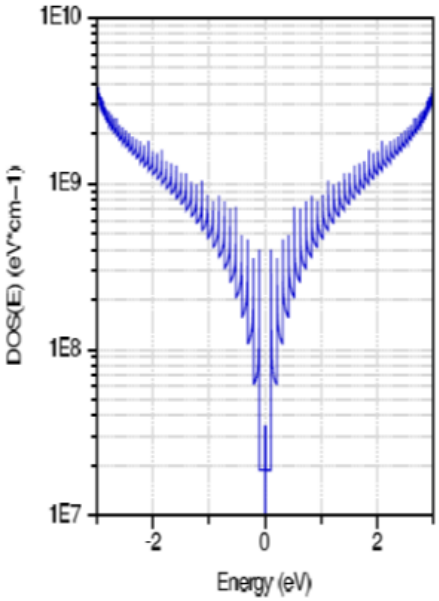

Figure 4.1: Density of States of a (90,90) SWCNT

SWCNT in each MWCNT. Since a single tube, contained in the MWCNT system, can have a large diameters (also tens of nanometers), the DOS, like that reported in Fig. 4.1, presents several energetically close VHS. The first question is whether the MWCNT optical response, in the visible range, is similar to that of the HOPG, because of the large number of VHS washing away the structured peaks, or rather the one-dimensional character makes the MWCNT optical response really different from that of HOPG and similar to that of SWCNT.
In the tight-binding model and gradient approximation [58], the result is that the superposition of the coaxial nanotubes makes VHS peaks disappear, except for the common plasmonic structures. The featureless optical behavior results therefore similar to the HOPG case. In this context in the reference [59], an individual MWCNT is handled as a solid anisotropic cylinder with an effective dielectric tensor, whose components are derived from the HOPG dielectric constant tensor.

In further ab-initio theoretical studies, focused on the MWCNT static dielectric constant [60], the difference between the longitudinal response, that is the sum of the contribution from the SWCNT constituting the multi wall system, and transverse response, dominated by the outer few layers, is considered.
Moreover angle-resolved photoemission measurements and density functional calculations of the electronic band dispersion reported in [61], reveal dispersionless behavior of the band perpendicular to the CNT axis, indicating a very weak inter-tube interaction.
Therefore the general results of these approaches are summarizable in two main points:

- the featureless behavior of the optical response in the visible range,
- the low interaction between the differing shells constituting the MWCNT system.

However these first conclusions have been questioned in other works. In the paper [62] the small inter-tube interactions are supposed to give a contribution by no means negligible to the electronic structure, opening a band gap at the Fermi Level. Moreover in the Density Functional Theory approach [63] the interaction between the two shells of a Double Walled Carbon Nanotube is calculated and, by generalizing this result, in the MWCNT a static charge transfer from the outer shell to the inner one is expected.
Also the featureless HOPG-like behavior is questioned. Several works evidence experimental results and theoretical predictions which suggest the presence of structured peaks under 3 eV. Measurements of photocurrent and of electron energy loss show that the electronic density of MWCNT is considerably different from that of HOPG and suggest the presence of singularities, due to the reduced dimensionality [7, 64, 65]. In particular, electron energy loss calculations predict interband relaxation channels in MWCNT [66].
Other results of photoluminescence and static transmission measurements have been reported in which the VHS seem to play a crucial role in the MWCNT optical response [67, 68]. In my opinion the particular processing to which the MWCNT were subjected in these experiments prevents definitive conclusions, but, at the same time, from all these results it is further confirmed that the electronic structure of the MWCNT is still a crucial and open question. Moreover the theoretical description of the nonlinear susceptibility χ^3 is essentially missing [69, 70].

Addressing the questions described above is essential not only from a theoretical point of view, but also to rationalize the very promising response of the MWCNT in photovoltaic devices, as it will be explained in the next paragraph.
Among the HOPG-like or the SWCNT-like character, another important question has been long time addressed and absolutely is still to be solved, i.e. the character of the conductivity in MWCNT. It is a very intriguing challenge involving different and promising perspectives, also concerning the superconductivity behavior revealed in the MWCNT systems [71, 72, 5]. But here I want to underline only one question among the others. The conductivity in MWCNTs is enhanced because of the presence of several shells, representing a multi channels for the flow of the current [9, 73], and it is very useful property because in the photovoltaic devices an enhanced conductivity can represent a great benefit.

4.2.2 MWCNT: challenging materials

The MWCNT represent a very promising challenging materials for a several technological applications [74, 59, 7]. Concerning the photovoltaic devices, as described before, it is known that

- the enhanced conductivity in MWCNT, described before, represent a huge benefit;
- the advantage of the MWCNT film is that they can be produced cheaper than the SWCNT film [75].

The main crucial issues to be addressed are resumed in the following points.

- Are there VHS under 3 eV? Do they affect the absorption and represent a significant factor in raising the photovoltaic devices efficiency? Together with the facilitated conductivity, can the VHS presence explain the MWCNT IPCE larger than SWCNT case under visible irradiation? [65]
- The interaction of the MWCNTs with substrate (for example Si as in [64]) or with nanoparticles donor group (for examples copper as [7]) enchances the IPCE value. What are are mechanisms that justify this behavior?

Is it possible to choose the geometrical configuration of the MWCNT film in order to improve the photovoltaic performances? This last question has been yet addressed as in [76].

All these issues are pushing toward a further studies. To address these questions, we have performed a series of experiments reported in the next paragraph and in chapters 5 and 6. In the following paragraphs in particular I will report our paper that has been submitted to ACS Nano.

4.3 MWCNT TRANSIENT TRANSMITTIVITY

4.3.1 Abstract

High-resolution time-resolved transmittivity measurements of horizontally aligned free-standing multi-wall carbon nanotubes reveal an exciton-like and non-linear behavior that has hitherto been observed only for single-walled nanotubes. The exciton relaxation channels are rationalized using a rate equation model that describes the dependence of the transient signal on the probe polarization. Further the coexistence of linear and non-linear terms is quantitatively confirmed. The data allows for a much more detailed understanding of the complex electronic structure of multi-wall carbon nanotubes and their functionality in optoelectronic applications than previous studies.

4.3.2 Introduction

An understanding of optical transitions and the underlying electronic structure of carbon nanotubes is of central importance to their characterization and numerous potential optoelectronic applications. For single-wall carbon nanotube the density of states, dependent on the chirality and dominated by Van Hove singularities (VHS), is well defined and the excitonic nature of the optical transitions is well explored. Conversely multi-walled carbon nanotubes (MWNT) represent a significantly more challenging system and as yet no coherent understanding of their properties exists. The presence of multiple concentrically nested nanotubes, each with different chirality, complicates the electronic structure. Theoretical and experimental studies predict similarities between the electronic properties of SWCNT and MWCNT, however conflicting reports also suggest electronic properties approaching that of graphite [64, 77]. At the same time multiple shells enhances electrical conductivity due to the several distinct transport pathways [73, 9, 7, 76] and results in high absorption cross-sections and large spectral absorbance

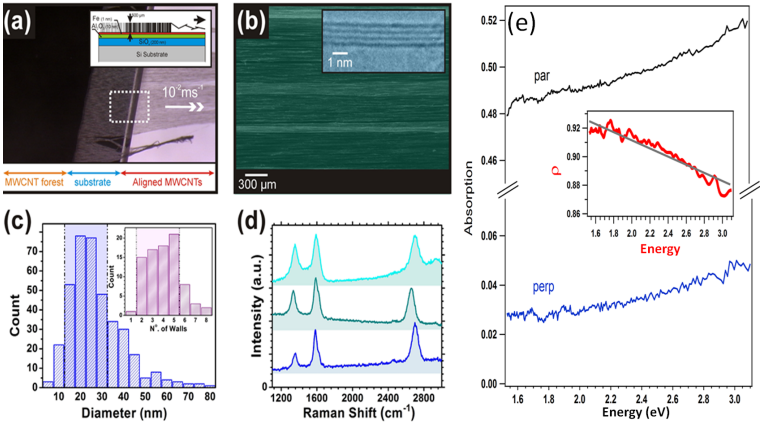

Figure 4.2: (a) Optical micrograph of a vertically aligned MWCNT forest during membrane extrusion. Insert: Cross-section schematic of the catalyst wafer. (b) SEM micrograph of an aligned MWCNT membrane (300 μm). Insert: HR-TEM micrograph showing the graphitic walls of the thermal chemical vapour deposited MWCNT (scale bar 1 nm). (c) Histograms showing the outer diameter and number of graphitic walls (Insert). Highlighted areas denote the mean $\pm$ 1 S.D. (d) Raman spectra (633 nm, 3 mW) of the as-grown MWCNT forest (top) and an extruded membrane (middle, bottom). Negligible variation was noted in the acquired spectra across samples . (e) Static absorption measurements for light polarized parallel (par) and perpendicular (perp) with respect to the MWCNT longaxis. Static polarization (ρ) as a function of energy.

over the entire visible spectrum [74, 59]. Such characteristics make MWNT extremely promising in photovoltaic cell applications [7, 6], in particular in combination with different electron donor groups. Indeed, their incident-photon-to-current efficiency (IPCE) have been found to be much higher than that of SWNT [7]. Key to such future device applications, however, is a more detailed understanding of their electronic and optical properties. Here, we use time-resolved optical spectroscopy to unambiguously reveal exciton-like behavior in MWCNTs which was masked in previous static spectroscopic studies. By performing monochromatic transient transmittivity in the near-infra-red (790 nm), we demonstrate that the electronic structure of MWCNT is marked by the presence of multiple VHS and the electron dynamics trace an exciton relaxation response typical of semiconducting SWCNT. We use highly aligned suspended MWCNT films to negate detrimental contributions from the substrate. Horizontal alignment ensures that the probed electronic

structure is unaffected by variable sample features, such as nanotube curvature [11]. Photobleaching and photoabsorption channels, typical of SWCNT exciton dynamics [30], are clearly identified in the transient response. Moreover, non-linear effects, only measurable when the probability of creating two or more excitons per nanotube is non-negligible, are also present [78]. By tuning the probe polarization we reveal linear photoabsorption and non-linear exciton-exciton annihilation in MWNTs.

4.3.3 Sample preparation and experimental set-up

MWCNT were synthesized by thermal chemical vapor deposition in a commercially available cold-wall reactor (Aixtron Ltd.). Vertically aligned nanotube forests were grown from 200 nm thermally oxidized Si substrates magnetron sputtered and thermally evaporated with 10 nm Al_2O_x and 1 nm Fe, respectively. These bilayer catalysts were heated to 700 $C^{\circ}(5C^{\circ}/s)$) under 8 sccm C_2H_2 diluted in 192 sccm H_2 (25 mbar). Aligned, free-standing thin films were fabricated by solid-state pulling at a rate of $\sim 10^{-2}m/s$, as illustrated in the insert of Fig. 4.2a, using a similar technique as reported elsewhere [79]. To ensure the probed characteristics are associated expressly with the MWCNT, no post-growth chemical processing was performed. Figure 4.2b shows a scanning electron micrograph (SEM) of an aligned, free-standing MWCNT films. A high-resolution transmission electron micrograph (HR-TEM), showing the graphitic walls, is given in the insert of Fig. 4.2b. The as-grown MWCNT were 500 μm long, 25 ± 13 (S.D) nm in diameter and consisted of 2-5 graphitic walls (Fig. 4.2c). Figure 4.2d shows the 633 nm (3 mW) Raman spectra (Renishaw InVia) of the extruded aligned-nanotube at multiple positions on the membrane evidencing the films high uniformity.
The use of free-standing, well aligned horizontal MWCNT, permits strict control over the relative angles between the MWCNT and the incident polarization whilst simultaneously avoiding detrimental substrate optical interference effects. Herein 'perpendicular-polarized' is defined as the light polarization perpendicular to MWCNT long-axis and 'parallel-polarized' where the polarization parallel to the MWCNT long-axis.
A Ti:Sapphire cavity-dumped, mode-locked laser oscillator was employed throughout. The output pulse was centered at 790 nm (1.55 eV) with a pulse width of 120 fs (FWHM). The output energy was 50 nJ (per pulse) for variable repetition rates from 54.3 MHz to a single shot. Mean heating effects were obviated using a tunable repetition rate. The pump fluence

ranged from 0.1 to 0.8 mJ/cm^2. Low fluence measurements were obtained at a repetition rate of 540 kHz to maximize the signal-to-noise ratio. A lock-in acquisition technique was employed to provide high transient transmittivity signal ($\Delta T/T$) resolution.

4.3.4 Results and discussion

In MWCNT the large number of nested nanotubes smear out the VHS, resulting in an electronic structure tending toward that of Highly Oriented Pyrolitic Graphite (HOPG) [77, 58, 64]. Static absorption measurements, performed using an ultraviolet-visible near infra-red spectrometer, are shown in Fig. 4.2e. When the incident polarization is parallel to the MWCNT long-axis (denoted 'par'), the absorption is substantial compared to the perpendicular case (denoted 'perp'). No particular absorption peaks, characteristic of VHS, are present in agreement with a HOPG-like electronic structure. Nevertheless, an indication of the presence of VHS can be obtained by estimating the polarisability, ρ of the system as defined as [74, 53]:

$$\rho = \frac{\Lambda_{//} - \Lambda_{\perp}}{\Lambda_{//} + \Lambda_{\perp}} \tag{4.1}$$

where $\Lambda_{//}$ is the absorbance for incident beam polarization parallel and $\Lambda_{\perp}$ perpendicular to the MWCNT long-axis, and $I/I_0 = e^{-\Lambda}$, where I is the intensity of the transmitted beam and I_0 is the incident intensity.
As for SWCNT [53], ρ (insert, Fig. 4.2e) linearly decreases with photon energy (1.55 - 3 eV), suggesting the existence of VHS under 3 eV. In fact, with respect to the spectrum at 3 eV, absorption at the VHS strictly depends on the selection rules, leading to increased anisotropy under 3 eV.
In order to unambiguously evidence VHS in the electronic structure of the MWCNT, we have performed monochromatic transient transmittivity measurements.
Figure 4.3 depicts a typical transient transmission (ΔT/T). The pump and the probe excite at 1.55 eV with a fixed pump fluence of 0.25 mJ/cm^2 (10^{15} photons/cm^2). Figure 4.3a shows the transient transmittivity collected by fixing the pump polarization parallel to the MWCNT long-axis and, conversely, by changing the probe polarization, from parallel to perpendicular to the MWCNT long-axis. Two dynamics dominate the presented response. The first positive dynamic, at short delay times (< 150 fs), is consistent with photobleaching, in agreement with such effects noted in SWCNT [11, 52, 54].

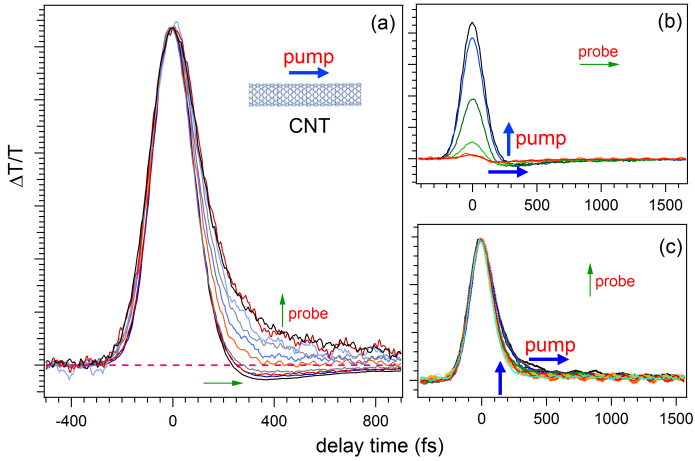

Figure 4.3: (a) Monochromatic transient transmittivity ($\Delta T/T$), at 1.55 eV, collected with the pump polarization parallel to the nanotubes long-axis and the probe polarization varying from the parallel to perpendicular. The incident fluence was 0.25 mJ/cm^2, corresponding to 10^{15} photons/cm^2. The sign of the second dynamic depends only on the probe polarization and varies continuously from negative (probe polarization parallel to MWCNT long-axis) to positive (probe polarization perpendicular to MWCNT long-axis). Spectra are normalized to the maximum response of the positive signal, excluding coherent-artefacts. Non-normalised dependence of $\Delta T/T$ with probe polarization parallel (b) and perpendicular (c) to the MWCNT long-axis, respectively. The pump polarization rotation does not affect the sign of the second dynamic.

Charge carriers are promoted by the pump from the ground state, to an excited state, and the absorption of the probe, at the same photon energy, decreases due to final state filling, with a corresponding enhancement of the probe transient transmission. The intensity of this photobleaching feature, for a constant pump fluence, is affected by coherence effects that strongly enhance the signal when the pump and probe polarizations are parallel to one another [29, 80].
The second dynamic ($>$ 150 fs) occurs over a temporal range independent of any coherence effects and, unlike the first dynamic, depends strongly on the probe polarization. In particular, the sign of this second response is negative when the probe polarization is parallel to the MWCNT long-axis and positive when it is perpendicular to it. By rotating the probe polarization relative to

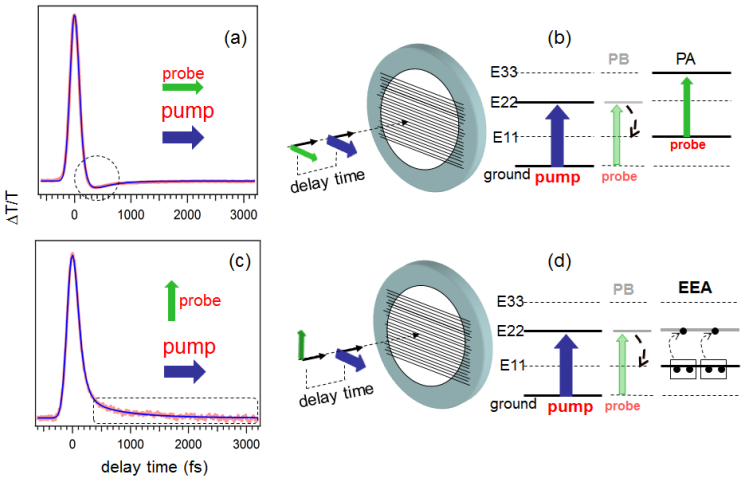

Figure 4.4: (a) $\Delta T/T$ for pump and probe polarizations parallel to the MWCNT long-axis. Best fit (blue) of the experimental data (red) as modeled by eq.3. Schematic of the relaxation channels (photobleaching PB and photoabsorption PA) rationalized in the proposed model as illustrated in (b). (c) As in a, $\Delta T/T$ signal (red) and fitting (blue) for pump polarization parallel and probe polarization perpendicular the MWCNT long-axis. (d) Schematic of the relaxation channels.

the MWCNT long-axis, from 0° (parallel-polarized) to 90° (perpendicular-polarized), the second dynamic changes in sign continuously from negative to positive. To clearly evidence this behavior the transient transmittivity signals (Fig. 4.3a) have been normalized to the maximum $\Delta T/T$ value of the photobleaching channel. The shape of the transient response is unmodified by this normalization. The change of sign depends exclusively on the probe polarization. To exclude a pump polarization contribution, in Fig. 4.3b with parallel-polarized probe, the pump polarization is rotated (at intervals $\pm$ 10°), obtaining a variation of the second dynamic intensity. The magnitude of this second dynamic is consistently negative for all polarizations. Similarly, fixing the probe perpendicular-polarization (Fig. 4.3c), the rotation of the pump polarization changes the intensity of the second dynamic, thereby maintaining the positive sign. In both cases, for pump fluences $\leq$ 0.25 mJ/cm^2, the intensity of the second dynamic follows the laser pump absorption that depends on the polarization of the laser pump with respect

to the MWCNT long-axis [74]. To derive some insight into this surprising dependence of the second dynamic on the probe polarization, we consider the origin of the negative sign (Fig. 4.4a). According to SWCNT [30, 33], we assume that the MWCNT have an exciton-like behavior. Then the relaxation channels are as illustrated in Fig. 4.4b.

The pump generates excitons from the ground to a higher excitonic state (E_{22}), that within a few tens of femtoseconds decay to lower energy state (E_{11}) [30, 33]. If the probe polarization complies with the selection rules, the probe pulse promotes excitons from E_{11} to another higher energy state (E_{33}). In the transient transmission spectra this process corresponds to an enhancement of the probe absorption (photoabsorption) producing the negative $\Delta T/T$ response [30, 33, 81]. While the MWCNT positive photobleaching response is consistent with the HOPG behavior, the negative response excludes the HOPG-like relaxation channels.

With a parallel-polarized pulse only the component of the dielectric constant parallel to the MWCNT long-axis is probed, corresponding to the component of the HOPG dielectric constant perpendicular to the graphite c-axis [82, 83, 59]. Under equivalent experimental conditions (Fig. 4.3), the HOPG transient response reveals photobleaching only. Two exponential decays, ascribed to electron-electron and electron-phonon relaxation, are clearly evidenced, in good agreement with the two temperature model [12, 55, 82]. At much higher pump fluences, a sign inversion in the transient optical response for HOPG has been reported and attributed to the structural deformation of the inter-plane distances due the presence of the so-called strongly-coupled-optical-phonons [84]. However, in MWCNT, such structural deformation can be excluded. The structural oscillations of the graphitic walls, observed in SWCNT, depends critically on the pump polarization thereby giving rise to periodic oscillations, not present in our measurements (Fig. 4.3) [22,34].

For MWCNT, the dependence of the negative dynamic on the probe polarization can be understood by considering the excitonic behavior and the dipole selection rules [1]. When the probe is parallel-polarized, the photoabsorption corresponds to $\Delta m = 0$, where m is the quantum number identifying the VHS sub-bands [85]. This photoabsorption channel (Fig. 4.3b and Fig. 4.4a) suggests that, as expected by prior consideration of SWCNT with a diameter of 1.5 nm [1], VHS are present also in MWCNT and give rise to defined optical transitions at energies < 3 eV. This result corroborates recent measurements reported elsewhere in the literature where it was shown that the VHS play an important role in the electronic behavior of MWCNT

[65, 64, 66].
The exciton behavior is also confirmed by considering the temporal trends of the proposed dynamics. By fitting $\Delta T/T$ (Fig. 4.3b) with a Gaussian function (representing the laser pulse) convolved with two exponential decays, we have estimated the relaxation times for the photobleaching and the photoabsorption channels. The decay time, at the different probe polarizations, is approximately 60 ± 20 fs, consistent with the decay time for the $E_{22} - to - E_{11}$ decay in SWCNT ($\sim 40 fs$). The second photoabsorption process develops after 150 fs and has a recovery time of the order of hundreds of femtoseconds [30].
As shown in Fig. 4.4c, when the probe is perpendicularly-polarized the sign of the second dynamic varies. In this case, according to the dipole selection rules, the polarization of the probe quenches the photoabsorbtion cross-section revealing alternative exciton relaxation channels created by the pump in the E_{22} state, as discussed below.
Figure 4.4d shows that the first stage of the process is equivalent to that described in Fig. 4.4b. Excitons are promoted by the pump from the ground state to E_{22} state, which induces photobleaching and a fast decay from the E_{22} to the E_{11} state. Due to the high pump fluence ($10^{14} - 10^{15}$ photons/cm^2) and the long decay time of the E_{11} state (few picoseconds) [1], excitons annihilate and repopulate the E_{22} state. This process, known as exciton-exciton annihilation (EEA), increases the transmittivity of the probe resulting in a second photobleaching channel.
Non-linear excitonic effects are well studied on spatially confined systems, such as nanocrystal [34], and have been more recently reported in SWCNT [51, 10]. In high density exciton conditions, scattering processes can annihilate two excitons promoting another exciton at a higher state, conforming to the conservation laws. In SWCNT many different models have been proposed to describe such EEA events, the most common of which is based on the rate equation approach containing an exciton population quadratic term [51, 2, 32]. Recently, in more sophisticated methods, the probability of scattering between two excitons has been found to be proportional to the mobility of the exciton along the nanotubes long-axis [35, 86]. EEA events can be approximated also by an exponential decay with a characteristic time of around 1 ps [10]. The interpolation (Gaussian convoluted with two exponential curves) of the transient transmittivity (Fig. 4.3c) gives a decay time of the second dynamic of around 1 ps, in agreement with [10]. In order to unambiguously demonstrate that the positive second dynamic is the result of an

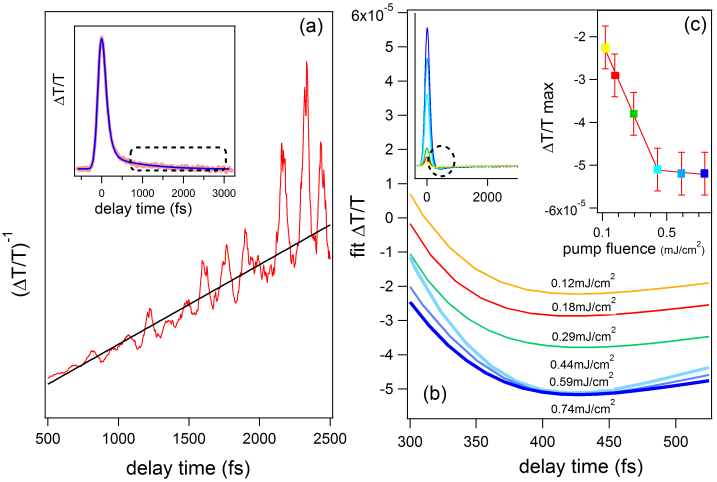

Figure 4.5: (a) $(\Delta T/T)^{-1}$ (extracted from the insert) as a function of the delay time for delays of 0.5-2.5 ps. Data fitted by linear interpolation. Spectra collected with pump polarization parallel and probe polarization perpendicular to the MWCNT long-axis. (b) Interpolated $\Delta T/T$ (Insert) as a function of increasing pump fluence. The saturation effect of photoabsorption channel (second negative dynamics) is shown in (c) by plotting the maximum value of the $\Delta T/T$ relative to the photoabsorption effect versus the pump fluence.

EEA process, in Fig.4.5a the inverse of the transient transmission $(\Delta T/T^{-1})$ is plotted as a function of the delay time. The quadratic dependence of the exciton population temporal evolution on the population itself implies that [51, 10].

$$(\frac{\Delta T}{T})^{-1} \propto \Delta t \tag{4.2}$$

where Δt is the delay time between pump pulse and probe pulse. The linear behavior shown in Fig. 4.5a confirms the non-linear character of the second dynamic, when the probe is perpendicular-polarized.
To elucidate the photoabsorbtion promotion mechanism, rather than EEA in the second dynamic, in Fig. 4.5b the dependence of the photoabsorption channel on the pump fluence (top-left insert) is shown by fixing the probe polarization parallel to the MWCNT long-axis. By increasing the fluence, saturation is clearly noted, as highlighted in some detail in Fig. 4.5c where

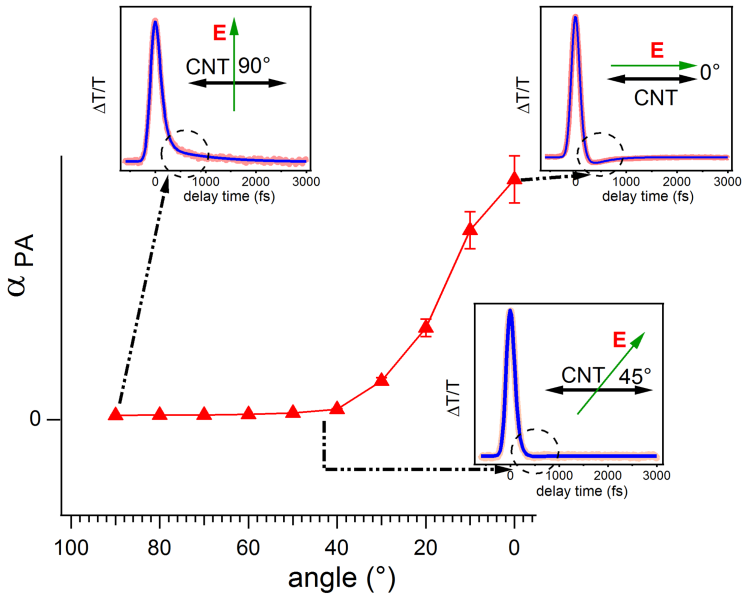

Figure 4.6: Photoabsorption coefficient (eq.3, eq.4) as a function of the angle between the probe polarization and the MWCNT long-axis. When the probe polarization is perpendicular to the MWCNT long-axis, photoabsorption is quenched (top left insert). Photoabsorption becomes non-zero around 45° (bottom right insert) and reaches a maximum when the probe polarization is parallel to the MWCNT long-axis (top right insert).

the photoabsorption (maximum) versus the pump fluence is plotted. As the non-linear EEA channel quadratically increases with fluence, the probability of the probe revealing this non-linear effect increases much more rapidly than the linear photoabsorption. Thus, the latter mechanism saturates. Photoabsorption is then quenched by rotating the probe polarization from parallel to perpendicular and/or by increasing the pump fluence. In this second case, the enhanced exciton density, corresponding to an increased EEA process, repopulates the E_{22} state whose relaxation is described by the second positive dynamics (insert of Fig. 4.5a).

To rationalize our findings, we propose a rate equation model to interpret the physical processes depicted in Fig. 4.4. The temporal evolution of the excitons on the E_{22} state (N_2) and on the E_{11} (N_1) are then determined by

$$\begin{cases} \dfrac{dN_2}{dt} = A \cdot Gauss(t) - B \cdot N_2 + \dfrac{C}{2} \cdot N_1^2 & (4.3) \\ \dfrac{dN_1}{dt} = B \cdot N_2 - D \cdot N_1 - C \cdot N_1^2 & (4.4) \end{cases}$$

where E_{22} is populated by the Gaussian pump $(\sigma\sqrt{2\pi})^{-1}e^{-\frac{t^2}{2\sigma^2}}$ and depopulated by the second term (-BN_2) with B^{-1} corresponding to the N_2 decay time ($E_{22} \rightarrow E_{11}$). The third term (C$N_1^2/2$) represents the population of the E_{22} state due to the annihilation of the excitons on the E_{11} state. In agreement with the first rate equation, the E_{11} state is populated by the relaxation of the excitons from the E_{22} state (BN_2) and depopulated by the relaxation on the ground state (-DN_1) and the annihilation process (-CN_1^2). The $\Delta T/T$ signal has been interpolated, in a non-perturbative approach, by the expression:

$$\frac{\Delta T}{T} \propto N_2 - \alpha_{PA} N_1 \tag{4.5}$$

where α_{PA} is proportional to the magnitude of the photoabsorption.
The transient responses, given in Fig. 4.4a and Fig. 4.4c, for the parallel- and perpendicularly-polarized probe, are well interpolated by the proposed model (fit denoted in blue, data in red). In the fitting procedure, the C parameter, that represents the EEA weight, was fixed as the pump fluence did not change throughout the measurements. The fitted mean B^{-1} value, for different spectra, is 60 ± 20 fs. This value is consistent with the 40 fs reported for the $E_{22} \rightarrow E_{11}$ decay time in SWCNT [16] and with the result previously obtained by interpolating the data with two exponential curves. For the perpendicularly-polarized probe spectra the D^{-1} decay time is a few picoseconds, corresponding to the long decay of the lower E_{11} excitonic state. In the case of parallel-polarized probe spectra (with negative photoabsorption dynamic) D^{-1} results in a few hundreds of femtoseconds, as reported in the literature for the photoabsorption recovery time in SWCNT [16].
In Fig. 4.6, the fitted α_{PA} value, representing the photoabsorption weight, is shown as a function of the angle between the probe polarization and MWCNT long-axis. $\alpha_{PA} = 0$ when the angle is 90° because the selection rule prevents photoabsorption. Increasing the component of the probe polarization along the MWCNT long-axis, $< 45°$, the photoabsorption, again in agreement with the dipole selection rules, starts to increase, reaching the maximum value

when the polarization direction is along the MWCNT long-axis. The excellent fitting of the data with the proposed rate equation model represents compelling evidence for the exciton-like behavior in MWCNT.

4.3.5 Conclusion

Using high-resolution time resolved transmittivity measurements carried out on horizontally aligned free-standing MWCNT, we have shown that the electronic structure of such systems are governed by excitons generated at the VHS and are extremely similar to more simple semiconducting SWCNT. The revealed exciton relaxation channels are rationalized using a rate equation model that describes the dependence of the transient signal on the probe polarization and the coexistence of linear and non-linear terms is quantitatively confirmed. The presented empirical evidence not only provides a deeper understanding of the so-far unconfirmed and complex electronic structure of MWCNT, but also an important support to studies on the SWCNT-like behavior of MWCNT, invoked to explain the performances of many MWCNT-based electronic devices.

CHAPTER 5

OPTICAL RESPONSE OF THE VERTICALLY ALIGNED SINGLE AND MULTI WALL CARBON NANOTUBES

5.1 INTRODUCTION

In this chapter we present an analysis of the optical transient response of vertically aligned SWCNT and MWCNT.
The aim is to demonstrate that these CNT architectures reveal a transient optical behavior similar to that of MWCNT horizontally aligned, supporting the new results shown in chapter 4.
On vertically aligned SWCNT and MWCNT, the transient reflectivity $\Delta R/R$ will be considered. Considering $\Delta R/R$ proportional to the change of the imaginary part of the dielectric function [12], therefore, as reported in this chapter, a photobleaching process corresponds to $\Delta T/T$ with a positive sign and to $\Delta R/R$ with a negative sign.
The first part of the chapter is a further discussion of the vertically aligned SWCNT sample (defined here sample A), already presented in chapter 3.
Then the optical response of a different vertically aligned SWCNT sample (defined sample B) will be analyzed.
As explained before, in this chapter 4, transient reflectivity $\Delta R/R$ is measured. The negative sign of the optical response is confirmed, as reported in chapter 3 for the vertically aligned SWCNT, but, at the same time, this other interesting insights about this CNT architecture are evidenced.
Measurements of the MWCNT vertically aligned reflectivity complete the framework.

At the end the transient reflectivity spectra obtained with a supercontinuum as a probe are shown and briefly discussed.

5.2 VERTICALLY ALIGNED SWCNT

5.2.1 Monocromatic pump-probe on SWCNT vertically aligned

Figure 5.1 shows a scheme of the experimental set-up for $\Delta R/R$ measurements on vertically aligned CNT. The experiment was made in the configura-

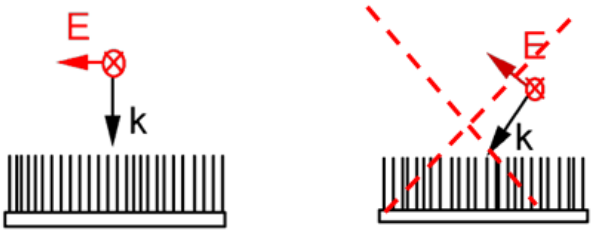

Figure 5.1: Left panel: experimental set up in normal incidence. Right panel; possible set up with a non-zero polarization component parallel to the CNT long-axis, not employed for the high light scattering.

tion shown in the left panel, with the pump and probe polarization directions perpendicular to the vertically aligned CNT long-axis. The right panel shows the possible configuration to obtain also a polarization component parallel to the CNT long-axis. In this case, whit the pulse polarization parallel to the incident plane, the electric field vector has a component along the CNT axis. However rotating the angle between the sample normal and the beam propagation direction, the light scattering was increased, making it very hard to collect any reflected signal.
Really the CNT vertically aligned samples had two characteristics increasing the difficulties of the reflectivity measurements: the high light scattering, that complicates the collection of the reflected beam, and the high absorption power. This "black-body" character, in particular in some of the employed samples, decreased the static reflected signal intensity under the instrument sensibility. Indeed our data of the static reflectivity are not useful because of the noise above the low signal intensity.

In Fig. 5.2a the ΔR/R for the sample A is reported, with the pump and probe polarizations both perpendicular to the CNT long-axis and with the

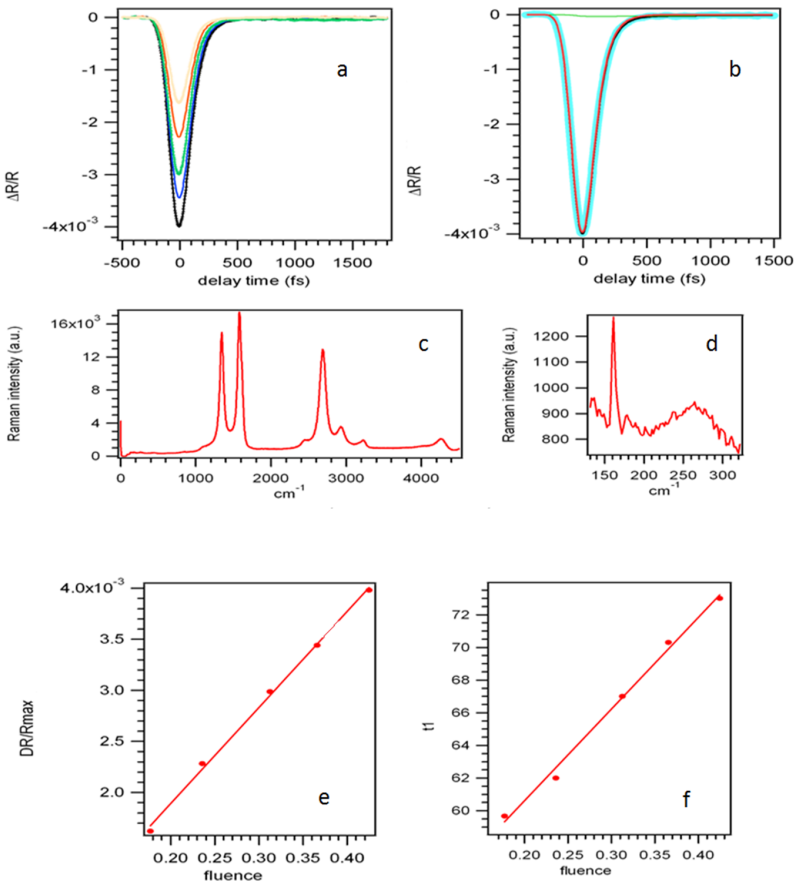

Figure 5.2: **(a)** ΔR/R on SWCNT vertically aligned at different pump fluences. **(b)** fit on ΔR/R. **(c,d)** Raman spectra. **(e,f)** Behavior of ΔR/R max and of t_1 decay time versus pump fluence (mJ/cm^2).

pump fluence ranging from 0.2 mJ/cm^2 to 0.4 mJ/cm^2.
An evaluation of the maximum number N_0 of exciting photons per pulse gives $10^{14} < N_0/cm^2 < 10^{15}$. The absorption efficiency, which depends on the light polarization and is difficult to estimate, can decrease these values, but they represent an upper limit giving interesting information.

Following the approach reported in ref. [35], an estimate of the phonon temperature can be done and, in correspondence to the maximum number of photons $N_0/cm^2 \approx 10^{15}$, we obtain $\Delta T \approx 100$ meV. Supposing that this energy is totally transferred by scattering to the exciton state, characterized by an exciton binding energy of some hundreds of meV, we conclude that at our fluence the excitonic states are not thermally broken. Therefore the excitonic picture can be used in order to grasp the physical process (for a further discussion see also chapter 6).

As discussed in Chapter 3, the negative sign of the $\Delta R/R$ for vertically aligned SWCNT is opposite to the positive sign of the unaligned case and this result is confirmed also at different pump fluences.
As already shown in chapter 3, the negative response can be interpreted as a photobleaching effect on the E_{22} excitonic state. In fact the Raman spectra shown in Fig. 5.2d indicate that the diameters range from 1 nm to 1.6 nm, corresponding to values of the VHS energetic positions around 1.5 eV, that can be populated by the exciting photon energy of 1.55 eV (see also chapter 3 [11]).
In order to give a quantitative analysis of these results, a good fit is obtained with only one exponential curve convoluted with a gaussian (Fig. 5.2b), representing the exciting pulse. A second exponential curve, representing an eventual second dynamic, is not necessary in order to give a good interpretation of the data.
Comparing this behavior with the optical transient response of the horizontally aligned MWCNT discussed in chapter 4, I observe that for the pump and probe polarization directions perpendicular to the CNT long-axis the second dynamic disappears in both cases.
Moreover the resulting decay time has an average value of around (65 +- 15) fs (Fig. 5.2f) and is still consistent with the decay time from the second excitonic level E_{22} to the first one E_{11}, reported in literature [30] and discussed in chapter 4 for MWCNT. The linear trend of the decay time against pump fluence (Fig. 5.2f) leads to exclude radiative processes. Indeed with the probe at the same energy of the the pump resonant with the second VHS, the relaxation from E_{22} is measured and the radiative decay is quenched.
Figure 5.2e shows the behavior of the $\Delta R/R$ maximum value versus the pump fluence. This result does not evidence a saturation in the considered excitation range ($\approx 10^{14} N_0/cm^2$).

Further important details can be retrieved considering the transient reflectivity measurements of a different SWCNT vertically aligned sample (sample

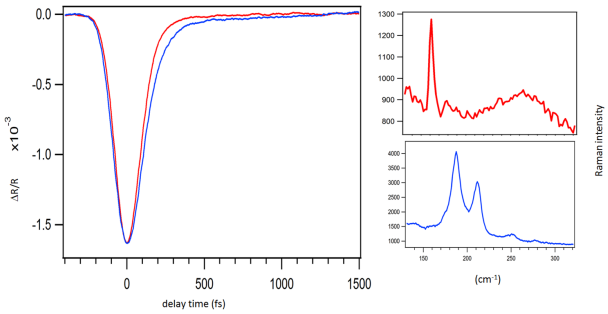

Figure 5.3: The comparison between transient reflectivity response of the sample A (with only one dynamic) and of the sample B (with two dynamics). In the right panel the correspondent BRM spectra.

B). In Fig. 5.3, we report the comparison between $\Delta R/R$ of the sample A (red color) and of the sample B (blue color), with the pump and probe energy of 1.55 eV. The respective Raman spectra are shown. In the sample B the second dynamic is evident. Why do the two similar samples, measured in similar experimental set up, show different behavior? The reason can be ascribed to the presence of a non-linear excitonic effect in sample B characterized by a more increased absorption than sample A. In order to explain this argument, the two Raman spectra, reported in Fig.5.3, have to be analyzed. In sample A the RBM are principally located around 160 cm^{-1} (peaked structure) and 270 cm^{-1} (broad structure) corresponding to diameters 0.9 nm and 1.55 nm. In the Kataura scheme [15] these diameters indicate second VHS energies of about 1.25 eV and 1.7 eV. Therefore the second VHS in the SWCNT ensemble may certainly be populated by the 1.55 eV photon energy, but they are not exactly in resonance with this energy.
On the contrary, in sample B, the RBM are located around 185 cm^{-1} and 215 cm^{-1} corresponding to diameters of 1.4 nm and 1.2 nm. In the Kataura scheme second VHS energies are of about 1.25 eV and 1.5 eV, closer to 1.55 eV. Therefore in this case, even if the pump polarization is perpendicular to the CNT axis, the resonance condition results in a greater population effect and consequently the second dynamic is evident. Even though a quantitative estimate is not calculated, this qualitative analysis seems to be consistent with the Raman measurements evidence.
In order to discuss the nature of the second dynamic in sample B, the results

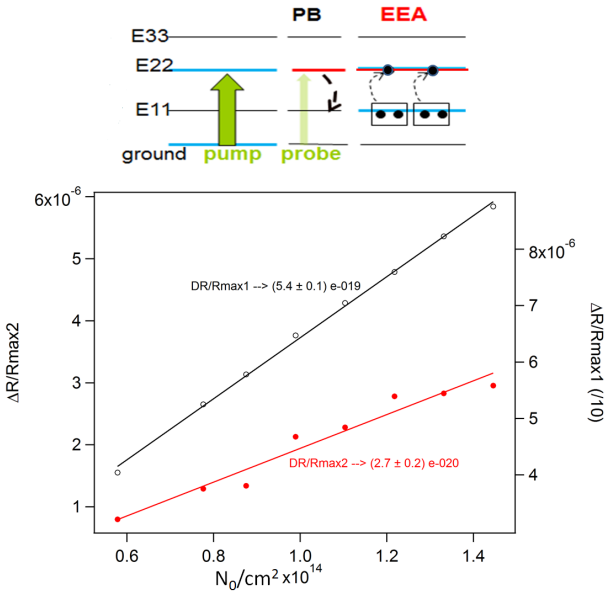

Figure 5.4: open black dots represent $|\Delta R/Rmax|$ of the first negative dynamics revealing a linear behavior (black line) on SWCNT vertically aligned (sample B). Filled red dots represent $|\Delta R/Rmax|$ of the second negative dynamics still revealing a linear behavior (evidenced by the red line) on the same sample.

on the vertically aligned SWCNT are compared with those achieved on the horizontally aligned MWCNT reported in chapter 3. In that case, when the probe polarization is perpendicular to the CNT long-axis, a first decay of (60 +- 20) fs is followed by a second positive dynamic, of about 1 ps. I will show in the following that the response of the vertically aligned SWCNT is quite similar. As illustrated in top panel of Fig. 5.4, after the photobleaching effect and the decay of the excitons from the E_{22} to E_{11}, the exciton-exciton annihilation (EEA) process occurs in E_{11}. During this EEA two excitons annihilate giving rise to one exciton in E_{22}, repopulating it and generating the slower positive response, i.e. a second photo-bleaching effect.
In order to confirm this picture and give a more quantitative support, the spectra are fitted with a gaussian convoluted with two exponential curves. The first dynamic is (100 $\pm$ 10) fs, larger than that of the sample A, but

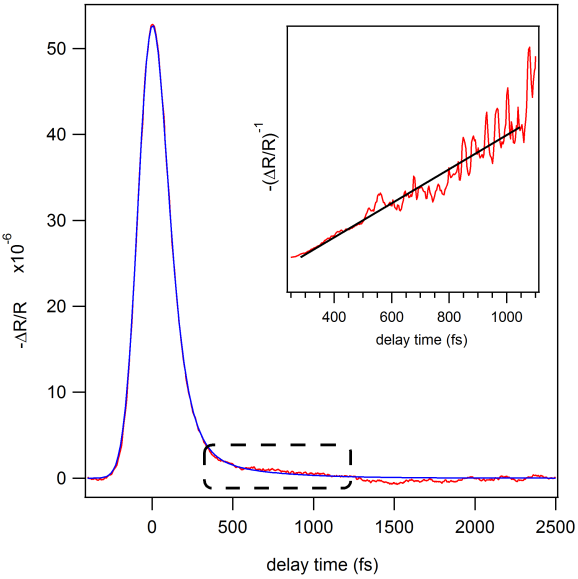

Figure 5.5: the $-\Delta R/R$ fit with the rate equation ; in the inset the $-(\Delta R/R)^{-1}$ linear behavior.

anyway in the pulse temporal width and consistent with (70 ± 20) fs. The second longer decay is (0.75 ± 0.15) ps, consistent with the 1 ps result obtained on MWCNT and in literature [10].
The first photo-bleaching peak intensity ($\Delta R/Rmax$) is about 100 times larger than the second one and this can be explained considering that the second process, even if favored by the resonance condition between the photon energy and the second VHS energy position, is partially quenched by the perpendicularity of the pump polarization to the CNT long-axis.
Moreover, we performed a scan of the transient response against the pump fluence. A rough evaluation of the photon number N_0/cm^2 is reported on the abscissa (Fig. 5.4). The open black circles represent the $\Delta R/R$ maximum value of the first dynamic, whereas the filled red circles the $\Delta R/R$ maximum value of the second non-linear process.

The trend of the first dynamic is linear not evidencing any saturation or non linear effect. This behavior is consistent with the literature results. In

ref. [2] the pump photon excites the E_{22} state. In one case the probe photon energy is chosen in order to capture the transient transmittivity response of the same E_{22} state, in a second measurement the probe energy is chosen to capture the transient transmittivity of the E_{11} state. For the E_{11} state, which is characterized by a life time of the order of some ps, the $\Delta T/T$ maximum vs the photon number reveals a saturation effect. In the case of pump and probe resonant with the E_{22} state, the relaxation channels are so efficient as prevent effect of saturation and a linear trend is revealed.
In our case we excite the E_{22} state and probe the same level. Then, concerning the first photobleaching dynamic, for the N_0/cm^2 comparable to the literature case, we obtained a linear trend, as expected.

Concerning the second photobleaching dynamic, its intensity is about two orders of magnitude smaller than the first one, the value depending on the measured zone of the sample, which can differ from the others because of the alignment degree of the CNT in the vertical direction. These small intensities make a quantitative study more difficult. Nonetheless also for the second dynamic we observe a linear behavior. If the more intense first response does not reveal a saturation effect, this should be true also for the second response. In fact the number of excitons from E_{11} to E_{22} is less than one half of the excitons originally excited by the pump pulse.
The difference between the slopes of the $|\Delta R/R|$max against N_0/cm^2 curve for the first and the second dynamics can give further information. The ratio is ~ 20. In an ideal process, with the CNT isolated and not interacting with other tubes in bundles, for each couple of excitons excited in E_{22} state and relaxed on E_{11}, only one exciton is promoted back in the second state. In this case the ratio between the two slopes should be ~ 2. But in the real situation, especially in the case of the CNT bundles, it is known that there are more decay channels from the E_{22} compared to the isolated CNT [1] and they represent different pathways reducing the relaxation process to E_{11}. This can justify the large difference between the two slopes. Therefore enhancing the number of photons, the corresponding increase of the second photobleaching process is reduced compared with the first one, because less excitons decay on E_{11} than those excited by the pump on E_{22}. Moreover not all the excitons into the E_{11} state are involved in the EEA process, but partially they decay from E_{11} to the ground state.
In order to confirm the non linear origin of the second photobleaching process, the $|\Delta R/R|$ signal is interpolated with the same rate equation employed

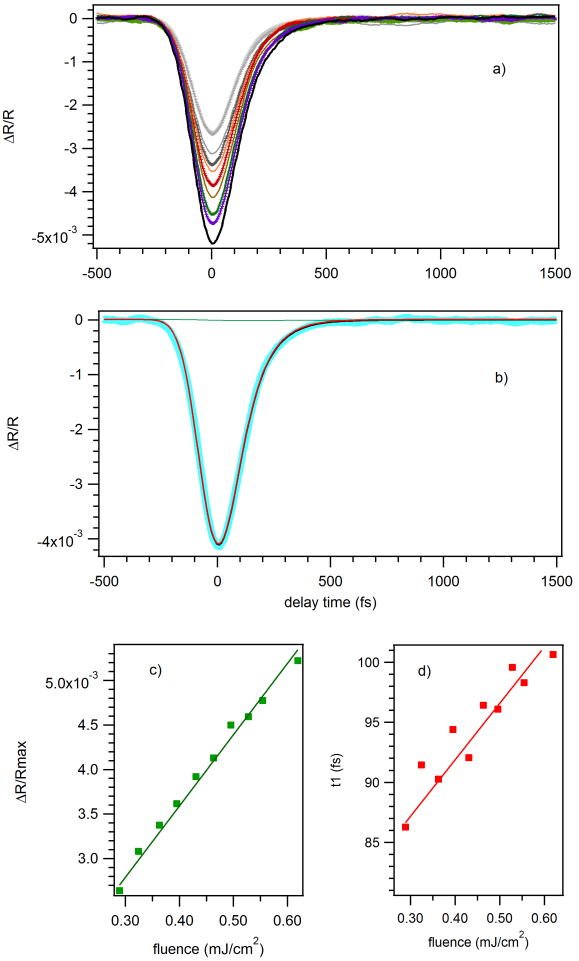

Figure 5.6: **(a)** ΔR/R on MWCNT vertically aligned at different pump fluences. **(b)** fit on ΔR/R. **(c)** Behavior of ΔR/R max and **(d)** behavior of t_1 decay time versus pump fluence.

in chapter 4,

$$\begin{cases} \dfrac{dN_2}{dt} = A \cdot Gauss - B \cdot N_2 + \dfrac{C}{2} \cdot N_1^2 & (5.1) \\ \dfrac{dN_1}{dt} = B \cdot N_2 - D \cdot N_1 - C \cdot N_1^2 & (5.2) \end{cases}$$

where

$$|\frac{\Delta R}{R}| \propto N_2 - \alpha_{PA} N_1 \tag{5.3}$$

whit α_{PA} representing a coefficient taking into account the weight of the photoabsorption effect in the spectrum measurement.
In Fig. 5.5 the fit is reported, evidencing a good result and confirming the non-linear model. The decay times are consistent with those determined by the simpler model with two exponential curves, already discussed.
Moreover we consider the inverse of the $|\Delta R/R|$ against time. As reported in literature [2] if the rate equation describing the process contains the term $\frac{dN}{dt} \propto$ -γ N^2 , then $(|\Delta R/R|)^{-1} \propto \Delta t$. As in chapter 4 for the MWCNT horizontally aligned, we still obtain the same result. In Fig. 5.5 $(|\Delta R/R|)^{-1}$ against time is shown and the linear behavior is evident, even if the fluctuations at these low signal intensity prevent an extension of the considered temporal range.
These results correspond to an important further corroboration of those reported in chapter 4: the MWCNT and the SWCNT transient optical response, in the infrared excitation regime, is quite similar.

5.2.2 Monocromatic pump-probe on MWCNT vertically aligned

In order to confirm the important correspondence between SWCNT and MWCNT in vertically and horizontally aligned configuration, MWCNT vertically aligned are also analyzed. In Fig. 5.6, the $\Delta R/R$ measurements also on MWCNT vertically aligned is reported, in the set up described in Fig. 5.1, with pump and probe polarization perpendicular to the CNT axis. Confirming the obtained results, also in this case the negative response can be attributed to a photobleaching effect.

The $\Delta R/R$max against the pump fluence does not reveal any saturation behavior. The fit procedure evidences only one exponential decay whose average value is about (95 +- 10) fs, consistent with the (70 +- 20) fs value. This confirms what we obtained above.

In order to have an overview of the obtained results, a resume is now useful. On MWCNT horizontally aligned, discussed in chapter 4, in a transient transmittivity measurement whit the probe polarization perpendicular to the CNT long-axis, a second dynamic, evidencing non-linear excitonic effects, can appear only if the absorption is strong enough and this is verified when the

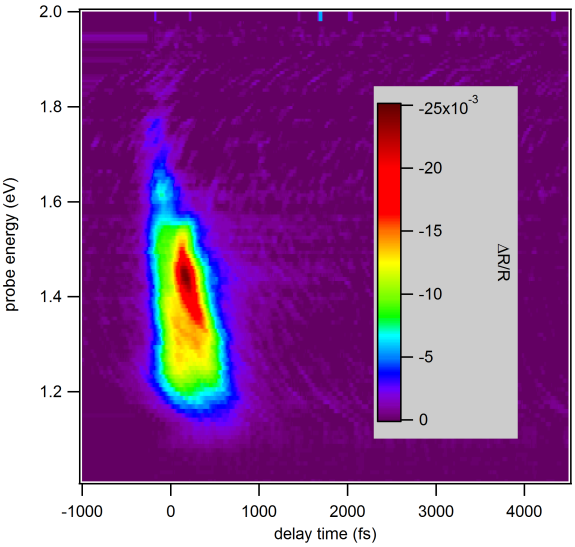

Figure 5.7: ΔR/R on SWCNT vertically aligned with Supercontinuum as a probe.

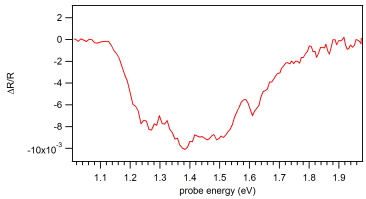

Figure 5.8: ΔR/R versus probe energy at delay time tau=0.

pump polarization is parallel to the CNT long axis. Reversely when the pump polarization is perpendicular to the CNT long-axis, the second dynamic is quenched.
In vertically aligned MWCNT measurements pump and probe are both perpendicular to the CNT long axis and coherently with the former interpretation the second dynamic is not revealed.
Concerning the measurements on vertically aligned SWCNT, the pump and

probe polarizations are both perpendicular to the CNT long axis. In this case the second dynamic is quenched when the pump energy is not resonant with the second VHS (sample A), conversely it is present when the pump is resonant (sample B), because in this last case the absorption is sufficient to generate non-linear effects.
This analogy between the horizontally or vertically aligned MWCNT and vertically aligned SWCNT not in resonance with the pump, suggests that the VHS although present also in MWCNT, are much less pronounced than in the SWCNT case. This is the reason why the MWCNT electronic structure can be interpreted as HOPG-like or SWCNT-like [64, 77].

5.2.3 Supercontinuum probe on SWCNT vertically aligned

In order to confirm the transient optical negative response at different probe photon energies we performed measurements with a supercontinuum probe, as already done in the unaligned SWCNT case, described in chapter 3. The result is reported in Fig. 5.7. Everywhere the response is clearly negative. In particular in Fig. 5.8, the $\Delta R/R$ value for different energies at delay time $\tau <$ 100 is reported. (In chapter 3 it is possible to find a deeper explanation of the supercontinuum spectra). There is no evidence of any particular structures and the negative response returns to zero around 2 eV.
Therefore a deeper study of the vertically aligned SWCNT, performed with the supercontinuum as a probe, confirms the dramatic difference in transient optical response compared to the unaligned SWCNT case.

5.2.4 Conclusion

The results obtained above clearly support the interpretation of the optical response of horizontally aligned MWCNT given in chapter 4. The MWCNT show an optical response very similar to that of SWCNT. Among the measured enhanced conductivity of the multi shell structure, the presence of structured peaks under 3 eV could represent an important improvement toward the understanding of high efficiency of solar cell devices based on MWCNT. Moreover the system of horizontally aligned MWCNT allows a great control of the angle between the polarization light and CNT long-axis, much more difficult in the vertically aligned configuration [53, 54].

CHAPTER 6

TRANSIENT TRANSMITTIVITY ON HORIZONTALLY ALIGNED MULTI WALL CARBON NANOTUBES WITH TUNABLE PUMP ENERGY

6.1 INTRODUCTION

This chapter contains a further analysis of the horizontally aligned MWCNT optical response, already introduced in Chapter 4. In the first section the results of three different experimental techniques will be presented, i.e. transient transmittivity $\Delta T/T$ with probe at 1.55 eV and pump energy tuned from 1.5 eV to 2.0 eV; $\Delta T/T$ with pump fixed at 1.55 eV and supercontinuum as a probe ranging from 1.2 eV to 2 eV; at the end, Incident to Photon Charge Carrier Efficiency (IPCE) measurements in which MWCNT are excited by continuum light from 1 eV to 3 eV. These measurements suggest the existence of peaked structures in the MWCNT optical response below 3 eV, confirming the previous results. In the second section the exciton behavior in the MWCNT under high laser fluence will be briefly discussed. Then the data, taken with the pump energies tuned from 0.8 eV to 4.1 eV, will be shown and interpreted in a rate equation framework. The hypothesis of the Multiple Exciton Generation (MEG) in MWCNT will be explored.

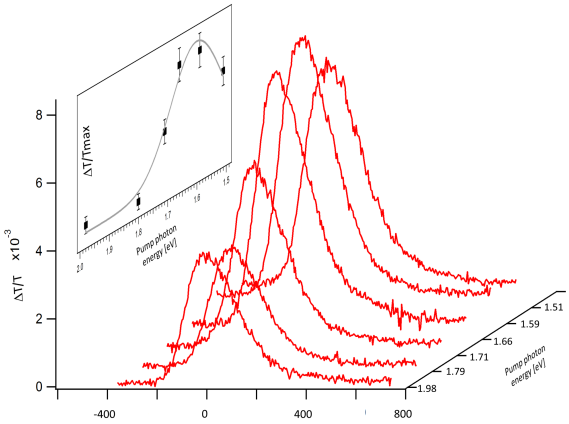

Figure 6.1: Transient transmittivity on horizontally aligned MWCNT with pump energy tuned from 1.5 eV to 2.0 eV evidencing a resonance around 1.6 eV.

6.2 SWCNT-LIKE BEHAVIOR AND PHOTOVOLTAIC EFFICIENCY OF MWCNT

Varying the pump photon energies in time resolved optical experiments allows to analyze the response of the system when excited at different energies. When the pump photon energy is in resonance with a particular optical transition, the transient optical behavior may vary. Therefore tuning the pump energy it is possible to identify the presence of structured features in DOS and to study the ultra-fast relaxation dynamics. Moreover this technique allows to discriminate if the effect of the pump excitation is mainly structural or principally due to an electronic excited population contribution. In chapter 7 a deeper analysis of these concepts is reported, applied in particular on HOPG study [12]. In this section the $\Delta T/T$ spectra with pump energy ranging from 1.5 eV to 2.0 eV and the probe at 1.55 eV are shown. The aim is to verify the existence of structured peaks in this energy regime.

In Fig. 6.1 on the horizontal axes the pump and probe delay time and the pump energies are represented. Each spectrum corresponds to a different pump energy. On the vertical axis, the $\Delta T/T$ is reported. In the graph on the top-left, $\Delta T/T$ maximum values ($\Delta T/T_{max}$) versus pump photon energy are reported. The $\Delta T/T_{max}$ behavior can be described with a gaussian-like

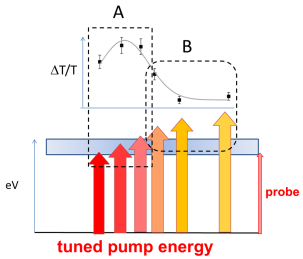

Figure 6.2: Schematic of the photobleaching process with energy pump tuned from 1.5 eV to 2.0 eV and the probe energy at 1.55 eV

trend, with a maximum around 1.6 eV.
In order to interpret this trend, it can be useful to remember two concepts. First the photobleaching effect depends on the intensity of the excitation, which is determined by the pump fluence or by the resonance condition between the pump photon energy and a particular electronic transition. In our case the pump fluence is kept constant.
Second, as discussed in ref. [55, 12], when the pump excites a material at a definite energy, the excited population spreads in a range of energies of the Brillouin zone. In absence of particular structures, the maximum of the optical response is achieved when the probe energy coincides with the pump energy, because in this case the maximum of the photoexcited population is intercepted. If the probe energy is larger or smaller than the pump energy, the probe intercepts only a tail of the photoexcited population, giving rise to a decreased optical response. For example for a pump energy smaller or larger than the probe energy of about 100 meV, in absence of resonances, the optical response is expected to be of the same intensity.
In the light of these preliminary considerations the trend shown in Fig. 6.1 can be qualitatively interpreted with the aid of Fig. 6.2. The probe energy is fixed at 1.55 eV and the pump energies vary from a value under 1.55 eV to values above 1.55 eV. Considering that the pump at 1.51 eV and at 1.59 eV are both near the probe energy, if no resonance exists, the trend should not reveal a structure reported in part A of the figure. Moreover at the enhanced energetic distance of 1.66 eV a decreasing optical response is not present, whereas, as explained above [55, 12], if the pump energy is higher than the probe energy, then the optical response should decrease. This last

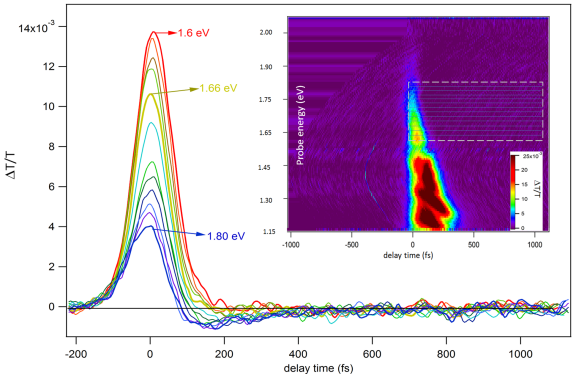

Figure 6.3: (a) Line profiles of the supercontinuum probe, at energies from 1.6 eV to 1.8 eV, on horizontally aligned MWCNT. (b) With supercontinuum probe, the $\Delta T/T$ versus the delay time between pump and probe and the variable probe energy. In the box the lines correspond to the spectra at different probe energies reported in (a)

explanation can instead justify the trend revealed in part B of the Fig. 6.2. In conclusion the global trend of the $\Delta T/T_{max}$ is consistent with a resonance around 1.6 eV.

This first qualitative result is consistent with the conclusions of the previous chapters and is confirmed also by the measurements reported below.

In Fig. 6.3 the transient transmittivity with a supercontinuum as a probe and the pump photon energy at 1.55 eV is reported. The pump fluences are comparable to those used in the experiment reported in chapter 4, that is 0.3 mJ/cm^2. The excitation determined by the pump fluence, as already discussed in chapter 5, allows an excitonic description of the optical response. The probe polarization direction is parallel to the CNT long-axis and in this configuration a retarded photoabsorption was found for pump and probe both at 1.55 eV (see the second dynamics discussed in chapter 4). The pump polarization direction is at 30° from the CNT long-axis, in order to enhance the absorption effect (maximum in the parallel configuration) and, at the same time, to decrease the coherent artifact, which appears when pump and probe polarizations are parallel.

In Fig. 6.3a the $\Delta T/T$ versus delay time is shown for different values of the probe energy, ranging from 1.6 eV to 1.8 eV. The considered spectra are taken from the evidenced zone in the graph of Fig. 6.3b, where the $\Delta T/T$

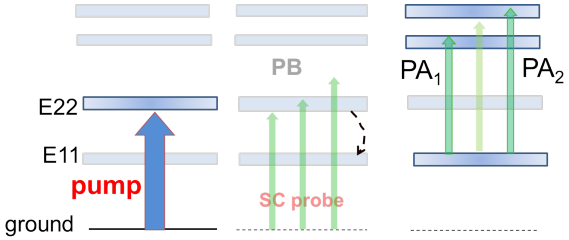

Figure 6.4: Schematic of the selective photoabsorption of the probe pulse.

intensity is reported against the delay time between pump and probe and the probe energies. The energy at 1.55 eV is not taken into account because of the presence of the pump pulse scattering in the photodiode arrays and the energies under 1.55 eV are not considered because the structured solitonic peaks characteristic of the supercontinuum pulse make unclear the analysis of the optical response in the first two hundreds of femtoseconds. The spectra corresponding to probe energies over 1.8 eV, though not conflicting with the results shown below, are not considered as affected by an increasing noise. All the spectra reported in Fig. 6.3a reveal a photobleaching initial response, which decreases in intensity as the probe energy increases above 1.55 eV (pump energy). This behavior means that when the system is excited by a pump energy at 1.55 eV also the states above the transition at this energy are partially populated causing a bleaching effect on probe absorption. Considering the region above the 1.8 eV of probe photon energy in Fig. 6.3b, we note that this effect is quenched when the energy difference between pump and probe exceeds ~ 0.4 eV. This $'expanded'$ photobleaching effect has been already found in the other transient optical measurements on different systems with supercontinuum as a probe and the pump energy at 1.55 eV.
Now it is interesting to analyze the second dynamics. In fact Fig. 6.3a clearly shows that when the probe energy ranges from 1.6 eV to ~ 1.7 eV, the global signal reveals only one positive dynamics, whereas, with the probe energy ranging from 1.7 eV to 1.8 eV, a second negative response appears, which can be interpreted as a photoabsorption, consistently with the model discussed in chapter 4. In fact the shape of the global transient optical response can be fitted with the same interpolating procedure used in chapter 4 and

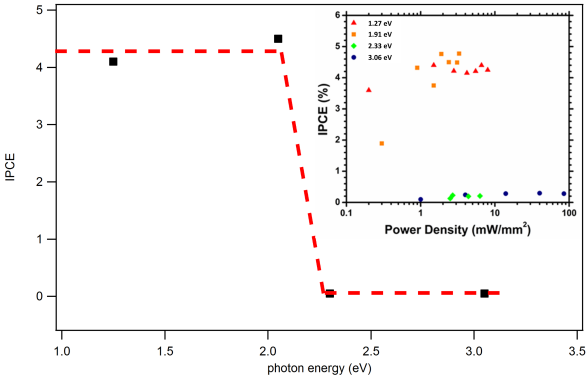

Figure 6.5: IPCE measurements for different photon incident energies. In the insert the same IPCE at different powers of the incident light.

based on the equation

$$\begin{cases} \dfrac{dN_2}{dt} = A \cdot Gauss(t) - B \cdot N_2 + \dfrac{C}{2} \cdot N_1^2 & (6.1) \\ \dfrac{dN_1}{dt} = B \cdot N_2 - D \cdot N_1 - C \cdot N_1^2 & (6.2) \end{cases}$$

Thus, referring to the discussion reported in chapter 4 about the meaning of this second photoabsorption process, now I offer an interpretation for the different behavior of the second dynamics at different probe energies. Figure 6.4 represents a schematic of the process. After a photobleaching effect on the E_{22} state for all the considered probe energies, the excitons decay in the E_{11} state in the first 100 fs. Then the photoabsortion can take place. PA_1 indicates the photoabsorption already measured with the probe energy at 1.55 eV and discussed in chapter 4. This process is indicated in the picture shown in the Fig. 6.4, but it is not detectable here, because at this energy, as already explained, the pump scattering into the photodiode arrays prevents the possibility to perform the measurement. For probe energies larger than 1.55 eV on the contrary it is here evident that the photoabsorption is initially quenched and this can be interpreted supposing that for these probe energies there is not a level with which the probe can be in resonance. Whereas, for probe energies from 1.7 eV to 1.8 eV, we assume that a state is available for a transition from the E_{11}, giving rise to the PA_2 process. This interpretation

means that also in the range above 2 eV the DOS of the MWCNT is structured, with energetically close and not pronounced peaks. Without evidence of this DOS character in static measurements, it is very difficult to quantify these transitions. For example it would be necessary to know the energetic position of the E_{11} level. Aware of these open issues, nonetheless it can be stated that the body of the experimental evidences, obtained with different experimental techniques and confirmed on several systems (see also chapter 4 and 5), allow a coherent interpretation toward the structured character of the MWCNT electronic structure [64].
In order to further confirm this analysis another experimental evidence can now be considered. Measurements of IPCE (Incident Photon to Charge carrier Efficiency) on horizontally aligned MWCNT have been performed (work done at the University of Cambridge by M. Cole). Since our final aim is to increase the photovoltaic performances of devices based on MWCNT, these preliminary results assume particular importance in the framework of our research. As shown in Fig. 6.5 it is evident the IPCE is consistently different from zero for the two exciting photon energy values under $\sim$ 2.3 eV and abruptly goes to zero for the two values over 2.3 eV. As the IPCE could be associated with an enhanced absorption efficiency and the structured features can promote it, this result can be interpreted as a further evidence of the fact that under 2.3 eV the horizontally aligned MWCNT reveals a SWCNT-like character. Moreover in the insert of Fig. 6.5 the same measurements at different powers of the incident light are shown, confirming the same behavior. It will be necessary to complete this analysis in order to understand if the IPCE rises again above 3 eV and in general in order to obtain information about the IPCE response in other light energy ranges.
In conclusion these results represent a coherent framework able to give a consistent interpretation of the MWCNT structure, but, at the same time, they are the first step toward the photovoltaic characterization of these very promising MWCNT systems.

6.3 NON-LINEAR EXCITONIC DYNAMICS ON MWCNT

The analysis of $\Delta T/T$ on horizontally aligned MWCNT with a pump energy variable from 0.8 eV to 4.1 eV and the probe energy fixed at 1.55 eV are presented (see chapter 2 for the description of the experimental set up). The preliminary question to be addressed concerns the possibility of using an excitonic description of the optical response also at high pump fluences

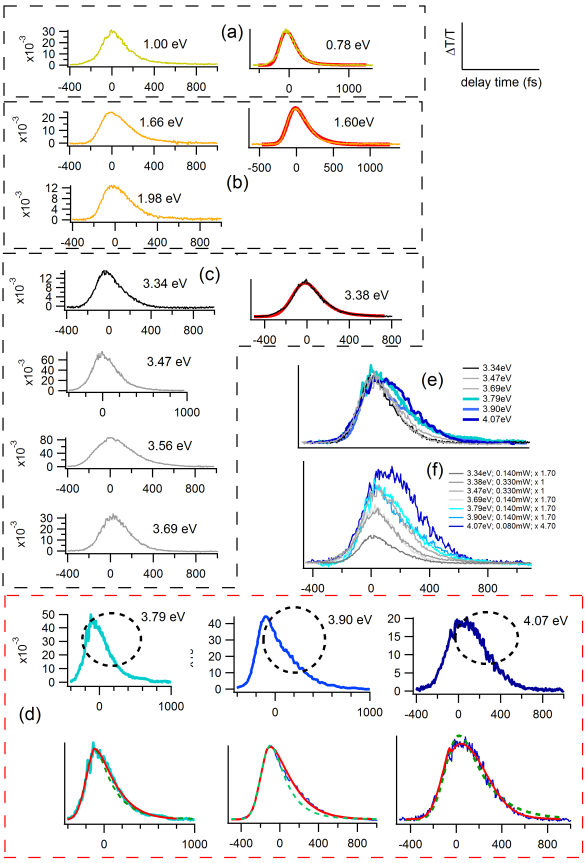

Figure 6.6: All the spectra have pump-probe delay time (fs) on the x-axis and the $\Delta T/T$ on y-axis. $\Delta T/T$ with pump in the 0.8-1.0 eV range (a); in the 1.5-2.0 eV range (already discussed in the previous section) (b); in the 3.3-3.7 eV range (c). At the right side of each section a spectrum fitted with an exponential curve is reported. (d) The three spectra at 1.79, 1.90 and 4.1 eV are shown, with the corresponding fits at the bottom, evidencing a behavior not reproducible with a simple exponential curve, but with a more complex fitting procedure (see text). (e) The spectra from 3.3-4.1 eV are reported with the same height. (f) The same spectra normalized at the same pump fluence.

employed in this experimental set up. Then the different $\Delta T/T$ spectra

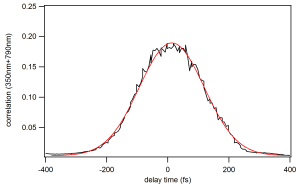

Figure 6.7: Cross correlation between the pulses at 4.07 eV and the 1.55 eV photon energies.

obtained in the 0.8-1.0 eV, 1.5-2.0 eV, 3.3-4.1 eV range of the pump photon energy are compared. The experimental evidence is compatible with the existence of Multiple Exciton Generation also in the MWCNT system. If confirmed, this last result could be relevant toward the improving of the photovoltaic efficiency of the MWCNT based devices. Because of the initial character of this research, other measurements will be necessary.

6.3.1 Thermal exciton breakdown under high laser irradiation

In order to operate the Traveling Optical Parameter Amplifier (TOPAS), the high fluence set up is employed (see chapter 2). For a pump power of 0.2-1 mW, the fluences are of the order of $5 - 20 mJ/cm^2$. The energy deposited in the MWCNT is large. Therefore the two issues to be addressed are

1 is it possible to give an estimate of the binding energy of the excitonic states in MWCNT?

2 is the thermal energy deposited into the MWCNT system sufficient to destroy the excitonic state excited by the pump pulse?

Both the questions represent an open issue and a strong challenge.
Regarding the first question, an evaluation of the exciton binding energies in SWCNT has been done by theoretical modeling, static and transient optical measurements [3, 19, 87, 22]. Depending on the SWCNT chirality, the binding energies range from $\sim$ 0.4 eV to $\sim$ 1 eV and strongly affects the optical response. Moreover the influence of the dielectric environment on the excitonic binding energy has been measured [21].
Instead, a study of the excitonic behavior in MWCNT, foreseen in this thesis, up to now is missing. In ref. [88] the expression fo the binding energy

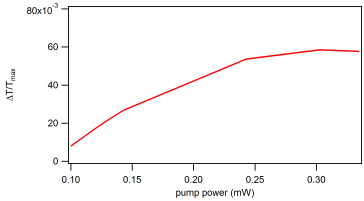

Figure 6.8: Pump power scan for the $\Delta T/T$ with a pump photon energy at 3.5 eV

for a SWCNT is done. But about MWCNT, all the following questions are completely open. Are the formula of the ref. [88] still valid? How the interaction between different shells modifies the Hamiltonian of electron and hole considered for SWCNT? And more, what are the roles of the dielectric constant and the effective mass? How many parameters influence the exciton binding energy in MWCNT? We know that all these points represent strong challenges and really intriguing research directions. For now we assume that the excitonic binding energy is around 0.3-0.4 eV, near to the SWCNT case.

Concerning the second question, as already discussed in chapter 5, in SWCNT a relation between thermal excitation and exciton binding energy has been studied [35]. Using this model, I have shown that, with the pump intensity employed in the low-fluence set up, the deposited thermal energy is well under the supposed binding energy of the excitonic state in MWCNT. But in the high fluence set-up, the conditions change. In order to get insight into this question, I analyze more deeply the references [35, 89]. In these works the excitation fluence is assumed to be transformed to phonon temperature enhancement ($\Delta Temp$). Following ref. [89] this $\Delta Temp$ represents a maximum temperature difference in the approximation of an instantaneous generation of hot phonon population. A $\Delta Temp$ of about 110 K is found in correspondence of 0.03 mJ/cm^2 light power. This $\Delta Temp$ leads to $\sim$ 35 meV. As the considered exciton binding energy is $\sim$ 400 meV, therefore the considered laser fluence is not able to break the excitonic state.
In this framework at our fluence of $\sim 5 - 20 mJ/cm^2$, the corresponding phonon energy should be from 1 eV to some eV, and, in particular for the highest values, a breakdown of the excitonic state should occur. However, in my opinion, there are several issues not clear in the MWCNT case. For example we have to understand if the approximation of a hot phonon population instantaneous generation is present also in the MWCNT case. The dynamics

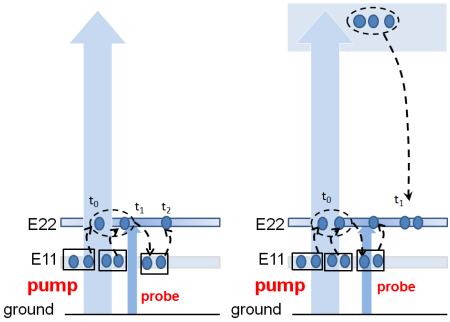

Figure 6.9: Schematic of the two hypotheses of MEG effect on MWCNT

in our measurements are very fast and it is not clear if, in the MWCNT, the interaction with a phonon population occurs in this temporal range.
Moreover a further effect should be considered. In ref. [90] the MWCNT thermal conductivity is discussed, evidencing, in particular, a high thermal dissipation, because of the heat radiation even for very low temperature gradients. An estimate of the thermal radiation, using the model reported in the ref. [90], is necessary. Moreover, in ref. [91] the high stability of the SWCNT excitonic state under high laser irradiation ($\sim 1mJ/cm^2$) is measured. In our case an evaluation of the energy deposited on the single nanotube composing the overall multi wall system has to be formulated. In addressing all these issues, I could find that a smaller number of photons are deposited on single CNT composing the MWCNT system.

Therefore, an understanding of these open points can decide if the excitonic model can be employed also in a high pump fluences regime ($\sim 10mJ/cm^2$). The previous considerations are not conclusive and they rather represent possible research directions toward a deeper analysis of the MWCNT. The importance of these aims will be more clear in the following sub-section.

6.3.2 Exciton behavior model on horizontally aligned MWCNT

The $\Delta T/T$ spectra with a pump variable from 0.8 eV to 4.1 eV and the probe photon energy at 1.55 eV are discussed. The main results are summarized in Fig. 6.6. All the spectra have been taken with a pump polarization direction mainly parallel to the CNT long-axis, with a depolarization effect due to the

optical elements in the pump-probe line. In any case no difference has been measured in dependence on the pump polarization direction. Moreover the optical response does not reveal any dependence on the probe polarization. This can be connected to the high pump fluence, which ranges from 4 to 15 mJ/cm^2, corresponding to an estimate of the photon number per cm^2 in the range of $1 \times 10^{16} < N_0/cm^2 < 7 \times 10^{16}$. For these values two scenarios are possible: a breakdown of the excited excitons; a possible description in an excitonic model and in this case, as pictured in chapter 4, the non-linear effects prevails, justifying the quenching of the photabsorption process shown in chapter 3. Again, addressing the problems described in the previous subsection, is crucial and, as already explained, they will be considered in the next future. However a more detailed analysis, evidences that, in particular for the pump photon energies ranging from 3.3 eV to 4.1 eV, the employed pump fluences correspond to N_0/cm^2 value of $\sim 1 \times 10^{16}$. In ref. [2] an excitonic description is used in this regime. For this reason, in the following, I will still consider an excitonic model, aware of the fact that the results have to be confirmed with other measurements on different systems.

Figure 6.6a shows two spectra collected with pump photon energies at 0.8 eV and 1.0 eV. The 0.8 eV spectrum is fitted with only one exponential curve convoluted with a gaussian. The decay time is about 140 fs, within the pulse temporal width. A pump power scan, from 0.2 mW, corresponding to $N_0/cm^2 \sim 1 \times 10^{16}$, has been performed (not reported here), revealing that the behavior is the same for all the incident fluences. The photobleaching effect at these pump energies can be justified considering that the pump fills a E_{11} state and for scattering processes also the E_{22} states can be filled, producing the photobleaching of the probe pulse at 1.55 eV. The decay from E_{22} is very rapid and in the temporal width of the pump pulse. Several attempts have been performed in order to improve the model and the fitting procedure, but the lack of features of these spectra makes these attempts little meaningful.

In the Fig. 6.6b three spectra with the pump energy ranging from 1.5 eV to 2 eV are reported and the 1.6 eV fit is shown. Also in this case a gaussian is convoluted with a simple exponential curve. The decay time is still about 150 fs. A detailed discussion on the spectra corresponding to these pump photon energies have been already reported in the first section of this chapter.

$\Delta T/T$ with a pump photon energy ranging from 3.3 eV to 4.1 eV gives more information.

In Fig. 6.6c the spectra collected from 3.3 eV to 3.7 eV are shown. All these

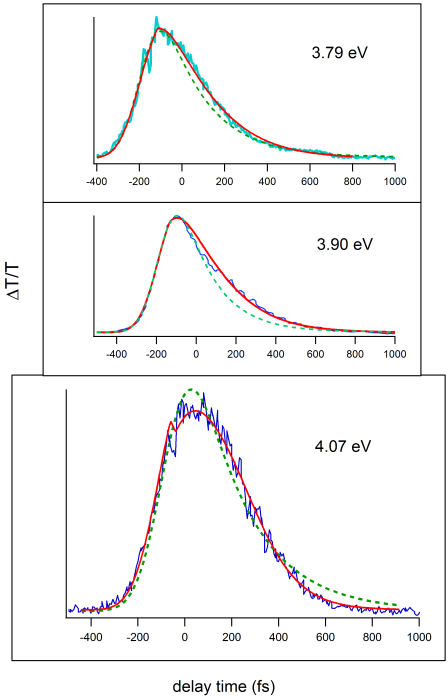

Figure 6.10: The spectra for 3.79 eV, 3.90 eV and 4.07 eV. The reported fits are from the equation 1 in the text. In the spectrum with 4.07 eV pump photon energy, also the fit with a simple exponential curve is reported, evidencing the failure of this fitting procedure.

spectra can be fitted with a simple exponential curve as indicated for the 3.38 eV fit.
In Fig. 6.6d the spectra collected with the pump photon energies of 3.79 eV, 3.90 eV and 4.07 eV are shown. An evident structure is present after the maximum. Figure 6.7 is the cross correlation of the pulse at 4.07 eV photon energy with the pulse at 1.55 eV photon energy. The cross correlation can be fitted with a gaussian curve and this shape of the pulse does not justify the structure appearing in the spectra of the Fig. 6.6d. The cross correlations performed with other photon energies (not reported here) present the same gaussian behavior. At the bottom of Fig. 6.6d, the spectra are presented with two possible fit procedures, the exponential not well interpolating the $\Delta T/T$

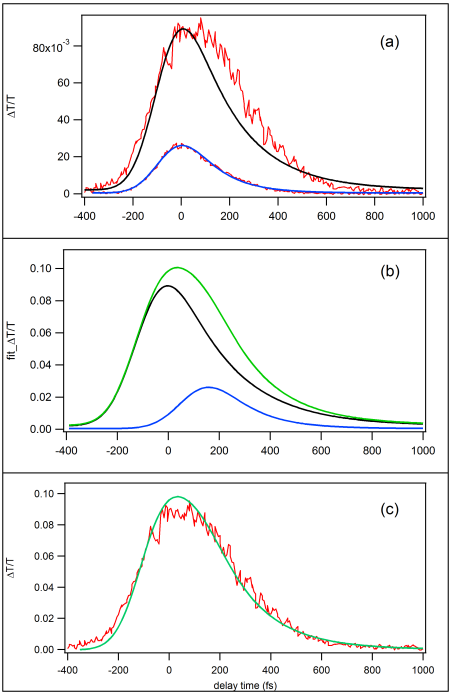

Figure 6.11: (a) $\Delta T/T$ of 4.07 eV and 3.34 eV spectra with the correspondent two exponential fits. (b) The two fitting curves are reported and the 3.34 eV curve is delayed compared to the other one by $\sim$ 150 fs. The green curve is the sum of the two exponential fits. (c) The sum is employed as a fit for the 4.07 eV spectra.

data and a different fit derived from a much more complex fitting procedure that will be discussed later. The not good result of the $\Delta T/T$ exponential fits evidences that the spectra for the pump photon energy > 3.80 eV present a singular character to be studied.

In Fig. 6.6e all the spectra with pump photon energies $> 3.3eV$ are reported and normalized at the same maximum value, in order to graphically evidence the structure present in spectra corresponding to the highest pump energies. The $\Delta T/T$ have been collected at different pump powers, because the generation of the 4th harmonic from the TOPAS is a tricky procedure and it is not possible to have the same power for all the pump photon energies. For

this reason a calibration curve at two energies, 3.39 eV and 3.5 eV, has been traced and Fig. 6.8 shows the power scan of the $\Delta T/T$ for pump photon energy of 3.5 eV (the other calibration curve has the same behavior). Then in the Fig. 6.6f the spectra normalized with the calibration curve are presented and also in this case the structures discussed above are evident.
A possible interpretation of these features can be obtained from the literature. In particular in [10] the Multiple Exciton Generation (MEG) has been found in SWCNT. The MEG process is known in systems of small dimensions, as nanocrystals [92, 93, 94]. The MEG origin can be an impact excitation of multiple excitons by a photoexcited single exciton [95]. In ref. [96] a single photon of energy larger than twice the fundamental excited state, can generate, in this fundamental state, two excitons. In ref. [10] the MEG has been revealed on SWCNT comparing the EEA effect on E_{11} under two conditions, in high fluence regime with a pump photon energy resonant with the E_{22} state, and in low fluence regime with a pump photon energy of 3.1 eV, close to twice of the first excited state ($2E_g$).
Considering this model, I suggest two possible interpretations.
The first interpretation can be formulated as follows.
When the pump photon energy ranges from 3.3 eV to 3.7 eV, because of a cascade effect, also the state at 1.55 eV can be populated, the photobleaching effect is revealed and a relaxation process can be interpolated by a simple exponential curve with a fast decay time ($\sim$ 100 fs). Instead, when the pump photon energy is >3.7 eV, a picture reported in the left part of the Fig. 6.9 can describe the process. When the pump excites the system, for a MEG effect an instantaneous generation of excitons in the E_{11} level occurs and also an instantaneous exciton-exciton annihilation populate the E_{22} level. In a subsequent temporal range (starting from t_1, as indicated in Fig. 6.9), the relaxation process from E_{22} to E_{11} takes places. In a later temporal range (starting from t_2 as reported in the picture) the refilling process of the E_{22} state occurs again for EEA event. This last non-linear process depends on the population of the E_{11} state which, in turn, depends on the population on E_{22} decayed to E_{11}. Obviously the high density makes all these processes very fast and in a temporal width of $\sim$ 500 fs the excitation is quenched. In order to quantitatively describe this interpretation we consider the following equation:

$$\frac{dN_2}{dt} = A \cdot G(t) - \delta(t - t_1) \cdot D \cdot N_2 + \delta(t - t_2) \cdot EEA \cdot N_2^2 \qquad (6.3)$$

describing the temporal evolution of the population in the E_{22} state. In the right-hand side the first term, G=$(\sigma\sqrt{2\pi})^{-1}e^{-\frac{t^2}{2\sigma^2}}$, represents a source of the excitons that, for MEG, are generated on E_{11} and, for EEA, are excited in E_{22}, giving rise to a photobleaching effect. Both these processes can be assumed instantaneous and within the width of the pump pulse. This source term has a temporal profile of the pump pulse. The G term is a linear term because there is a direct proportionality between the number of photons and the number of excitons generated in the E_{11} state.
Then the linear decay process from E_{22} occurs after a delayed time. In the rate equation the delta function corresponds to this retard and the $t_1 - t_0$ value is about 50 fs. The D^{-1} parameter, corresponding to decay time from E_{22} to E_{11}, is $\sim$ 100 fs, consistent with the values found in this thesis and in the literature for this decay process.
The quadratic term corresponds to the non-linear process which repopulates the E_{22} state for EEA event on E_{11}. It is directly the square of the N_2 population, because the N_1 population is strictly connected with the excitonic density present on E_{22} state. Also this process can be considered delayed compared to the MEG event and the instant $t_2 - t_0$ is about 70 fs from the center of a gaussian term (near the delay time $t_1 - t_0$).
The cascade process, considered for the spectra with a pump energy < 3.7 eV, here is not present, because the high exciton density generated by MEG effect dominates the global process.
The decay from N_1 state is not taken into account (as, on the contrary, in chapter 4), because again the high exciton density makes the events so fast that all the process ends into the first 550 fs. The fit based on the rate equation is good, as reported also in Fig.6.10, in which the exponential fit failure is also evident.
The result of this approximated model contains two useful indications, the presence of delayed dynamics, which influence the population on E_{22} and the presence of a non-linear term. Other analysis are necessary.
But the previous interpretation presents some critical elements. First of all, the delay time $t_1 - t_0$ and $t_2 - t_0$ are not justified in a solid theoretical framework and in the measurements of chapter 4, no delay enters into the used rate equations. In the present case the instantaneous MEG effect can play a role, which does not exists in the previous results, but a quantitative evaluation and a clear model is missing. Moreover, in the proposed model, the excitation at high pump photon energies is compared to the direct excitation of

the E_{11} state, without other differences. But, analyzing the spectra obtained with the pump photon energies on E_{11} around 1 eV (Fig. 6.6a) the shape of the spectra does not reveal any particular structure, as discussed before. Therefore, the proposed interpretation, with a fitting procedure from the rate equation, can be useful in order to give interesting information, however further efforts are necessary to a deeper understanding.
Now in order to formulate the second interpretation, the right panel of the Fig. 6.9 is considered. In this picture the excitation > 3.8 eV determine instantaneously a MEG process on the level E_{11} and, through the EEA process, the E_{22} level is filled. The population on E_{22} relaxes in a fast decay time. But, in this picture, the cascade process, from the higher excited states, can not be neglected and occurs in a time delayed compared to the instantaneous MEG process (t_1-t_0 in Fig. 6.9). In order to support this interpretation, the Fig. 6.11 has to be considered. In the Fig. 6.11a the two $\Delta T/T$ at 4.07 eV and at 3.34 eV pump energies are reported. The spectra are normalized at the same pump fluence (see also Fig. 6.6f). The fitting procedure is the exponential fit convoluted with a gaussian curve, both for the 4.07 eV (not in good agreement as already discussed) and for the 3.34 eV $\Delta T/T$. The two spectra are reported with the maximum value at the same instant $t = 0fs$. The fitting procedure of the 3.34 eV represents the population of the E_{22} state for a cascade process and a subsequent exponential relaxation. The fitting procedure of the 4.07 eV spectra represents the population of the E_{22} state through EEA on the E_{11}, filled by MEG process, and the subsequent exponential relaxation. Similarly, the population of the E_{22} state from the E_{11}, directly excited by the pump pulse at ~ 1 eV, was described by a fitting procedure with an exponential curve convoluted with a gaussian, as in Fig. 6.6a.
In Fig. 6.11b the fit curves are reported, but in this case the fit of the 3.34 eV spectrum is delayed of ~ 150 fs compared to the spectrum of 4.07 eV pump energy. The sum of the two fit curves gives rise to a green fit. Therefore the green curve can represent the sum of two processes. The first is the instantaneous MEG, which fills E_{11} and, through EEA, populates E_{22}. The second process, delayed from the first, is the population of E_{22}, due to a cascade of the excited carriers from the higher states. The total relaxation is the combination of the two relaxations. In fact in Fig. 6.11c, the sum fit curve is superimposed to the $\Delta T/T$ at 4.07 eV, obtaining a good result. The most pronounced peak of the fit compared to the $\Delta T/T$ spectrum can be explained as follows. Summing the considered fits, we assume that both

the population processes, due to the MEG and to the cascade event, can be described with a gaussian source. It can be right for the MEG process, because the excitons multiple generation is strictly connected to the gaussian shape of the pulse. Instead it is not clear if the population source of E_{22}, connected to the scattering process (cascade event) can be described as a gaussian source. Moreover the height of the 4.07 eV exponential fit could be overestimated because indeed the $\Delta T/T$ total response is the contribution of both the population mechanisms. In general an evaluation of the cross section for the two process has to be done and, for the moment, it is missing. In Fig. 6.6f, with spectra normalized to the same fluence, the $\Delta T/T$ at 4.07 eV is the most pronounced spectrum, revealing that the effect of the possible MEG process enhances the optical response, but the previous analysis excludes a total quenching of the cascade process.
The overall analysis has to be improved and the open issues will be addressed in the next future.
Although, for the moment, this last interpretation does not correspond to an equation model, generating a fitting procedure, however it seems to present less critical elements than the previous one.
In any case important questions to be addressed are the following.
In the literature the thermodynamic limit for the MEG process is $\sim 2E_g$ (E_g is the lower optical transition). In our case the possible MEG occurs at $\sim 4E_{11}$. How to justify this difference? Probably the complex structure of the MWCNT can give a justification.
Moreover measurements in lower fluence regimes could be necessary, in order to avoid non-linear effects which can not be controlled. We have used the lowest pump powers and therefore one possibility to further reduce the pump fluence is to enlarge the pump spot diameter, decreasing the total fluence.
Furthermore the same measurements on other systems, as unaligned SWCNT, have to be performed in order to compare the results and obtain, from this comparison, useful information.
Finally a deeper theoretical knowledge should be improved, in order to formulate a model able to interpret the MEG process.
Aware of the approximate level of these last results, I underline the importance of this experimental evidence. In fact the possibility to disentangle the complex processes occurring in the photo-excited MWCNT also in the violet light region and the possibility to control effects as a multiple generation of excitons represent crucial challenges in order to improve the photovoltaic performances of MWCNT based devices.

CHAPTER 7

PHOTOINDUCED $\pi - \pi^*$ BAND GAP RENORMALIZATION IN GRAPHITE

7.1 ABSTRACT

As is well-known, the character of the π orbitals is of paramount importance for the chemical properties of the carbon allotropes and their derived compounds. While at equilibrium the nature of these orbitals is well understood, their photoinduced nonequilibrium behavior is under investigation. Here, we demonstrate that when a UV-laser pulse excites a carrier density larger than 10 per cent of the π^* density of states in graphite, a renormalization of the π-π^* band gap takes place. This result has been achieved by detecting the transient reflectivity and the associated decay time of an infrared probe following the excitation of a UV pump pulse tuned across the π-π^* absorption resonance. The pump photon energy at which both the transient reflectivity and the decay time are maximum is downshifted by 500 meV with respect to the relative absorption maximum at equilibrium. This finding is interpreted as a transient π-π^* band gap shrinking of similar magnitude, near the M point of the Brillouin zone.

7.2 INTRODUCTION

In the past few decades, several new carbon allotropes have been discovered [97, 98, 99, 100] while in the last several years, very important behavior has been revealed about the structural properties of carbon compounds excited by an ultrashort and intense light pulse [101, 84, 102, 103, 104, 105]. These important findings will set the path for new discoveries about the pho-

tochemical properties of carbon-based materials. However, we first need a clear understanding of the interaction between an intense ultrashort light pulse and carbon based compounds.

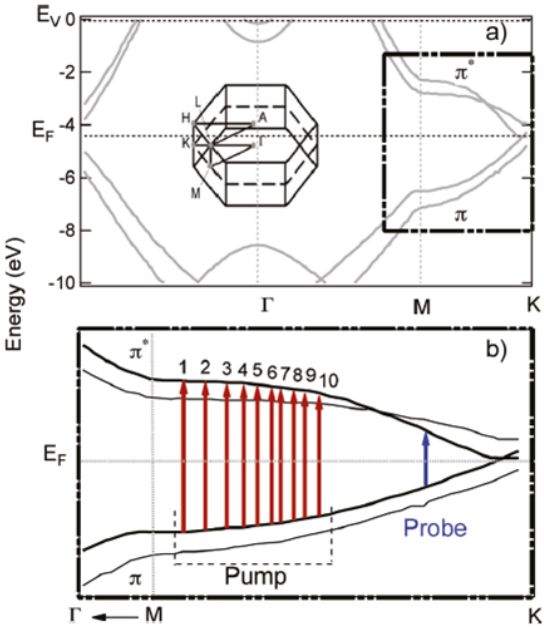

Figure 7.1: (a) Graphite electronic structure taken from ref [106]. The energies refer to the vacuum level $E_V = 0$. (b) Sketch of the transient reflectivity experiment. The laser pump photon energy is tuned across the numbered optical transitions (from 3.4 to 4.2 eV) close to the M-point of the graphite Brillouin zone. For each pump photon energy, the reflectivity of the probe, with a photon energy fixed at 1.5 eV, is acquired at different pump probe delay times (see Fig. 7.2).

The challenging mechanisms at the origin of this interaction rely on the fact that when an intense femtosecond laser pulse is absorbed by a solid, the electrons and the lattice are driven out of equilibrium, and both screening effects and rearrangement of the lattice occur because of the excitation of a large fraction of the valence electrons to the conduction band [107, 108, 109, 110, 111]. These processes are well-known in semiconductors, where the absorption of an ultrashort and intense light pulse suddenly

modifies the charge distribution, switching on screening effects resulting from Coulomb and exchange forces, while inducing a narrowing of the band gap (band gap renormalization, BGR) [112].
Typically by exciting about 10 per cent of the valence electrons, the lattice is destabilized and the band gap shrinks and eventually collapses to zero. This effect can be clearly revealed by detecting the nonequilibrium dielectric function, which exhibits a metallic character on a time-scale of 100-200 fs [112, 113, 114]. For these reasons, semiconductors have been the preferred materials for such studies [107]. Instead, in semimetals and gap-less compounds, such as graphite, the response to a sudden photoexcitation process, together with out of equilibrium behavior, remains unclear. Recently time-resolved electron diffraction and scanning tunneling microscopy studies on graphite [84, 102, 103] have shown that intense infrared (IR) femtosecond laser pulses can induce a new transient phase characterized by a pseudo sp^3-bonding configuration, but overall different from the known phases of diamond. The interplay between the dynamics of the structural changes induced by IR pulses and the reorganization of orbital charge has been also investigated by femtosecond electron energy loss spectroscopy and ab initio calculations [101, 104, 105, 115]. Because of the peculiar electronic structure of graphite, it could be interesting to study the photoexcitation with ultrashort coherent pulses in the ultraviolet (UV) spectral region. Here, we show that, when an UV-ultrashort optical pump excites about 2×10^{21} electrons/cm^3 across the $\pi - \pi^*$ band gap near the M point of the Brillouin zone (BZ), significant variations of the graphite optical properties occur. This transient change of the dielectric function takes place within 150 fs of the pump-pulse excitation and is consistent with a $\sim$500 meV gap renormalization of the π bands. Previous transient optical measurements on graphite [116] suggest the existence of a weak BGR in graphite (about 30 meV). This interesting, but limited information, has been obtained from experiments carried out using ultrashort IR pulses (800 nm, 1.55 eV). However, at these photon energies, the favorable coupling of the photoexcited carriers with a subset of high energy optical phonons (i.e., strongly coupled optical phonons, SCOP) [117, 118] can induce significant structural changes, preventing the detection of the bare electronic response [115]. By contrast, UV light pulses tuned across the $\pi - \pi^*$ optical resonance near the M point of the Brillouin zone (BZ) excite carriers whose relaxation does not involve significant SCOP effects. These experimental conditions allow the transient optical signal to be a straight forward fingerprint of the evolving electronic structure. More-

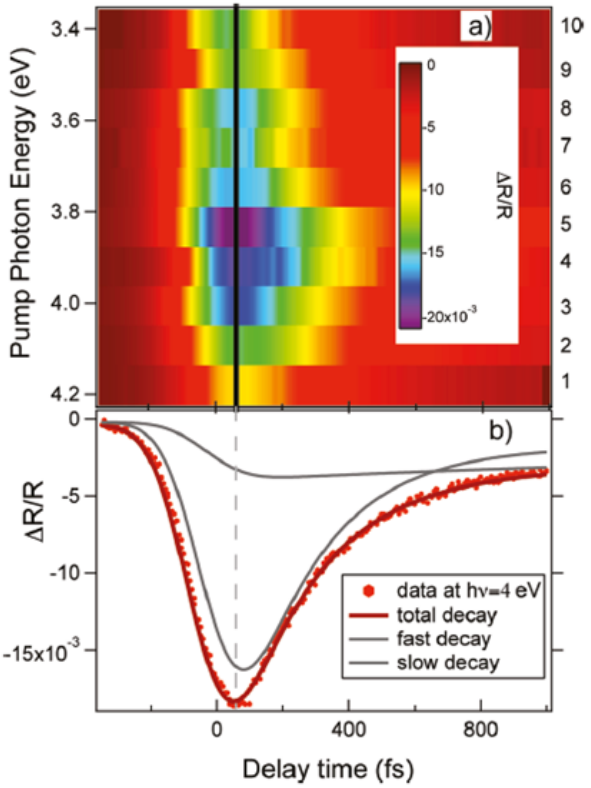

Figure 7.2: (a) Transient reflectivity spectra collected by tuning the pump photon energy from 3.4 to 4.2 eV and the probe photon energy fixed at 1.5 eV, as reported in Fig. 7.1. The pump fluence is 2.5 mJ/cm^2. (b) A representative analysis carried out on the transient reflectivity spectra to obtain information about the relaxation dynamics. The data are fitted with two exponential curves convolved with a Gaussian to take into account the laser pulsewidth.

over, at these photon energies, the strength of the electric dipole oscillator is expected to be larger than in the IR spectral region, inducing a significant π band structure rearrangement [119, 120, 121]. Therefore, the novelty of our time-resolved optical pump-probe experiment consists of studying the

transient electronic structure of a highly oriented pyrolytic graphite sample (HOPG) using a 3.4-4.2 eV tunable photon pump, while setting a spectator probe at 1.55 eV photon energy. Using this experimental approach, we are able to induce and reveal a strong BGR effect in a semimetal such as graphite.

7.3 EXPERIMENTAL DETAILS

The measurements are performed on a freshly cleaved HOPG sample using an amplified Ti:Sapphire laser system capable of delivering 150 fs light pulses at 1 kHz repetition rate, of 1 mJ energy at $\lambda = 790$ nm. A traveling wave optical parametric amplifier is then used to generate photons in the 1160-1460 nm (0.85-1.07 eV) spectral range. By quadrupling the output of the parametric amplifier, it is possible to span the photon energy from 3.4 to 4.2 eV. The resulting UV pulses (150 fs, 1-10 nJ), after being focused into a spot of 100 μm $\times$ 100 μm (equivalent to a laser fluence of 2.5 mJ/cm^2), are used to excite the HOPG sample. The transient optical reflectivity is measured by taking the difference between the probe reflectivity with and without the pump pulse. Optical absorption measurements with a continuous wave (CW) source were performed using a spectrometer.

7.4 RESULTS AND DISCUSSION

In the infrared and ultraviolet (IR-UV) spectral range, the possible bulk-band optical excitations in graphite are prevalently transitions between the $\pi - \pi^*$ bands (see Fig. 7.1a). At the K point of the reciprocal space, the electronic band structure displays a vanishing density of states (DOS) and a vanishing energy gap between the valence and conduction bands that shows, for a single layer, an identical linear k dispersion of the two π bands [106]. At the M point of the Brillouin zone, graphite behaves as a semiconductor. The electronic structure displays a Van Hove singularity in the joint DOS (JDOS), which is at the origin of a maximum in the absorption spectrum ($\pi - \pi^*$ resonance at 4.4 eV). In Fig. 7.1b, the red arrows represent the pump photon energies tuned from 3.4 to 4.2 eV, close to the M point of the BZ at equilibrium, that is, where the imaginary part ($\varepsilon_2(\omega)$) of the graphite dielectric function has a maximum. The probe transient reflectivity (TR) experimental data, taken at constant pump fluence and probe photon energy fixed at h$\nu = 1.55$ eV, are shown in a color map image in Fig. 7.2a. Under these experimental conditions, the effects correlated to the population relaxation [55] excited by the laser pump (3.4-4.2 eV) can be, in fact, excluded in the probe reflectivity

signal at 1.55 eV, because the decay of the carriers from the M-point toward the K-point near the Fermi level is unlikely, due to energy and momentum conservation [122]. To investigate the relaxation dynamics, each spectrum reported in Fig. 7.2a is fitted by two exponential functions convolved with a Gaussian to account for the laser pulse-width.

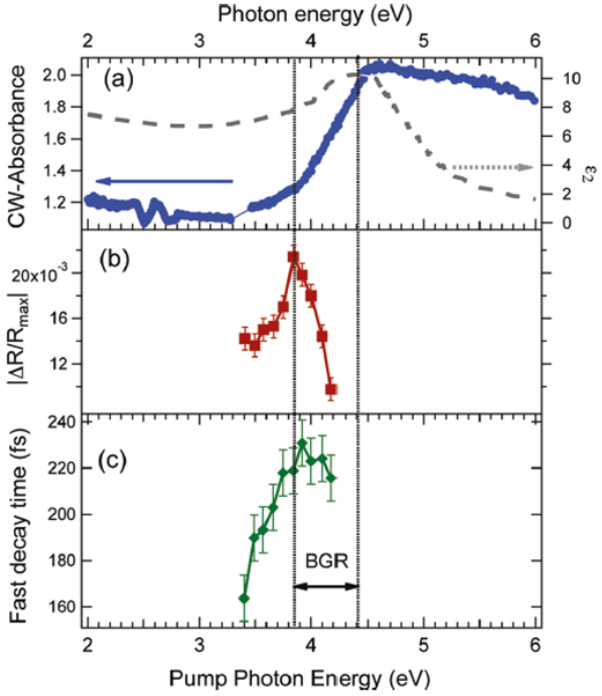

Figure 7.3: (a) Absorbance spectrum on graphite together with the imaginary part ($\varepsilon_2(\omega)$) of the graphite dielectric function from ref [120]. The maximum at 4.4 eV is due to the strong M-point optical transition. (b) the maximum of the transient reflectivity spectra shown in Fig. 7.2 versus the laser pump photon energy. (c) Dependence of the fast decay time on the laser pump photon energy. The shift between the maximum of the $\Delta R/R_{max}$ signal and the fast decay time with respect to that of $\varepsilon_2(\omega)$ represents the band gap renormalization value.

In Fig. 7.2b, the analysis of the decay times on a representative spectrum collected with the pump photon energy at 4 eV clearly shows both a fast

(τ_1 ≈200 fs) and a slow (τ_1 ≈2 ps) decay process, as will be discussed later. It is rather important to note that the maximum variation of $\Delta R/R_{max}$ and the longest τ_1 decay time are detected at about 3.9 eV. Because of the functional form of the reflectivity of solids at equilibrium [123], changes in the reflectivity signal are related to fractional change in both the real and the imaginary part of the dielectric function (ΔR=$\Delta R(\Delta\varepsilon_1,\Delta\varepsilon_2)$). Previous measurements on graphite show that TR signal is mainly dominated by the fractional change in the imaginary part of the dielectric function $\Delta\varepsilon_2$ at the probe photon energy [55]:

$$\frac{\Delta R(h\nu_{probe})}{R(h\nu_{probe})} \propto \frac{\Delta\epsilon(h\nu_{probe})}{\epsilon_2(h\nu_{probe})} \tag{7.1}$$

Hence, within the actual experimental conditions, the observed transient fractional variations of the reflectivity can originate only by transient modifications in the graphite dielectric function, which depend solely on the interaction between light and graphite electronic structure. Moreover, at constant pump fluence, the transient probe reflectivity variation, $\Delta R/R$, is only determined by the pump absorption. As a consequence of this model, the transient band structure changes are linked to the excited carriers density (N(E)), which is proportional to the pump pulse of fluence F, assuming an absorption coefficient $\alpha(h\upsilon_{pump})$:

$$\int_0^\infty N(E)dE = \frac{(1-R(h\nu_{pump}))F\alpha(h\nu_{pump})}{h\nu_{pump}} \tag{7.2}$$

Under these assumptions, the maximum of the transient reflectivity $\Delta R/R_{max}$ signal should be expected when the pump photon energy matches the energy of the $\pi-\pi^*$ excitations at the M-point of the BZ, where the absorption is maximum. At equilibrium, this energy is found to be 4.4 eV [119], which is in good correspondence to the relative maximum of the imaginary part of the dielectric function ($\epsilon_2(\omega)$) (Fig. 7.3a). A plot of $\Delta R/R_{max}$ versus pump photon energy (Fig. 7.3b) exhibits a maximum at 3.9 eV, 500 meV lower than the equilibrium value, implying that also the transient $\epsilon_2(\omega)$ maximum is shifted downward by the same amount. This finding is regarded as a clear evidence that the $\pi-\pi^*$ energy gap in graphite undergoes a band gap renormalization (BGR) when the estimated density of the photoexcited carriers is $2\times10^{21}/cm^3$. To avoid artifacts due to the quality of HOPG sample, absorption measurements at equilibrium are carried out on the same HOPG

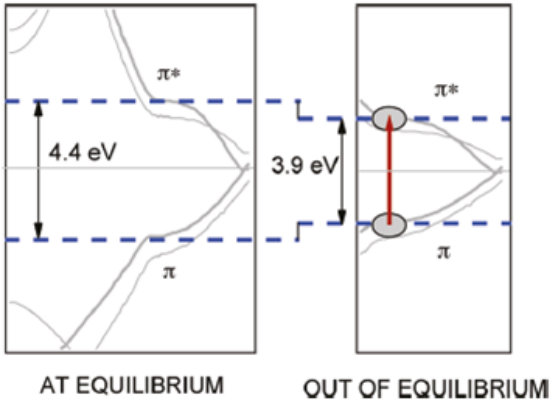

Figure 7.4: Sketch of the $\pi - \pi^*$ band gap renormalization in graphite.

sample used in the TR experiments. Figure 7.3a shows the spectrum of the CW-absorbance, defined as -ln(I_T/I_0), where I_T is the transmitted intensity and I_0 is the incident intensity, along with the $\epsilon_2(\omega)$ reported by Taft et al [120]. In agreement with the literature, the maximum of the absorption is detected at 4.4 eV. Further evidence of the observed BGR effect is provided by the study of the relaxation times. The TR spectra are well fitted by two different decay times (Fig. 7.2). The fast decay time ($\tau_1 = 200$ fs) is mainly due to electron-electron interactions, whereas the slow decay ($\tau_2 = 2$ ps) time is ascribed to the electron-phonon relaxation. These dynamics have to be compared to transient measurements performed by exciting the hot electron population close to the Fermi level (photon energy pump at 1.5 eV). Under this condition, the electron-electron scattering yields a thermalization of the excited electron population within 30 fs [116], relaxation mechanisms through SCOP assisted processes last for few hundreds of a femtosecond, whereas decay times on the picosecond time scale are attributed to photoinduced structural instabilities launched in the material [115]. In Fig. 7.3c, the dependence of the fast decay time on the laser pump photon energy is shown. The fast decay time increases with the photon energy up to 3.9 eV. Previous theoretical and experimental studies [122, 124] have shown that the lifetime of the excited carriers in graphite strongly depends on the wave vector of

the Brillouin zone. In contrast to electrons decaying from other regions of the band structure, electrons excited at the M point have comparatively long lifetimes. The dynamics of the TR signal are sensitive to the electronic band structure changes that depend on the lifetime of the excited carrier density. Therefore, a maximum of the TR decay time is expected at the M point optical transition energy where the carriers have a longer lifetime. The presence of a decay time maximum red-shifted of 500 meV with respect to the M optical transition at equilibrium represents the second experimental evidence of the π band gap shrinkage. The same shift of both the $\Delta R/R$ signal and the decay time maximum is the fingerprint of a photoinduced renomalization of the π band at the M point, as sketched in Fig. 7.4. In a phenomenological picture, the BGR effect can be explained by considering that, during the near-resonant pump laser pulsewidth, the excited carriers continue to modify the graphite band structure, altering the dielectric function and shifting the absorption peak about 500 meV toward the lower photon energies. This absorption shift can be monitored by the variation of the probe reflectivity, while the pump photon energy is tuned across the $\pi - \pi*$ transition. At a laser pump fluence of $\sim 2.5\ mJ/cm^2$ and photon energy of 4.0 eV, the carrier density excited in the $\pi*$ band is 10 per cent of the density of states around the M-point at equilibrium ($1.8 \times 10^{22} electrons/cm^3$) [106]. Hence, under the present experimental conditions, when $2 \times 10^{21} electrons/cm^3$ are injected into the π^* band, the $\pi - \pi*$ gap shrinks by 500 meV within 150 fs. These findings are in agreement with BGR observed in semiconductors when a carrier density of $10^{21} electrons/cm^3$ is induced by optical excitations [112]. Unfortunately, the experimental conditions prevented changing the laser pump fluence to verify the dependence of the BGR value on the excited carrier density. The present results can be fitted in a more general scenario, where the nonequilibrium structural properties of graphite produced by ultrafast coherent light excitations are considered. At the present, most of the studies reported in the literature concern experiments performed at 800 nm (7-9) or in the THz spectral region [125]. At these photon energies, the $\pi - \pi*$ excitations are close to the K-point of the graphite band structure (see Fig. 7.1b), where a selective coupling of the excited carriers to coherent phonons (SCOP) takes place in 100-500 fs. [115] Such structural vibrations could also modify the equilibrium optical properties of graphite. Single color pump-probe experiments at 800 nm (1.5 eV) show a change of the sign of the transient probe transmissivity ($\Delta T/T$). These findings have been the matter of two alternative interpretations [115, 116]. The first ascribes the

change of the transient transmission sign to SCOP-induced oscillations of the graphene planes along the c-axis, the second to a weak BGR effect (30 meV) that leads to a red-shift of the interband absorption. Unfortunately, by photoexciting the graphite in the near IR, it is not possible to decouple the electronic excitations from the SCOP effects. Instead, this is possible using near-UV photons. At these photon energies, in fact, transient changes of the dielectric function are mostly induced by $\pi - \pi*$ excitations near the M-point where the electron-SCOP coupling is weak. This phenomenological picture explains the strong BGR observed in the present experiment. In addition, the dynamics of the BGR suggest that electron-electron interactions, rather than structural effects, induce the band gap shrinkage. Very likely, this discovery discloses new photoinduced properties of graphite different from those observed in the IR regime. Further structural dynamical studies, using laser pulses in the UV regime (around 4-4.5 eV), can help clarify this question.

7.5 CONCLUSION

We report a careful and novel study of the transient electronic structure induced in graphite by an ultrashort and intense UV laser pulse. The experiment has been performed using timeresolved optical spectroscopy employing as a pump an ultrashort laser pulse tunable in the 3.4-4.2 eV photon energy region and as a probe the fundamental emission of a Ti:sapphire amplified laser. By tuning the pump photon energy across the graphite Van Hove singularity and exciting $\sim 2 \times 10^{21} electrons/cm^3$ across the $\pi - \pi*$ band gap at the M point of the BZ, we clearly show that a significant variation of the equilibrium graphite dielectric function occurs. This transient dielectric function alteration, occurring within the 150 fs of the pump-pulse excitation, can be reconciled with a 500 meV gap renormalization of the π bands. Finally, this significant transient rearrangement of the electronic structure of graphite is expected to be central to novel chemical properties, leading to new studies and applications.

CHAPTER 8

CONCLUSIONS

In this thesis I studied ultra-fast electronic dynamics in several architectures of Carbon Nanotubes, unaligned, vertically or horizontally aligned Single Wall and Multi Wall. Charge transfer and linear and non-linear excitonic interactions are analyzed with time resolved optical techniques. The principal results are summarized here.

1 In unaligned SWCNT a free charge carrier response has been highlighted and an inter-tube charge transfer between semiconductor and metallic CNTs has been experimentally evidenced, as an original result.

2 In vertically aligned SWCNT an excitonic behavior has been revealed.

3 In horizontally or vertically aligned MWCNT an excitonic response has been shown.

4 The new result of point 3 corresponds to a description of the MWCNT electronic structure as a SWCNT-like system for an optical response under 3 eV. In fact in this thesis a long debated question about the HOPG-like or SWCNT-like behavior of MWCNT has been addressed. The result of the set of measurements, performed with different techniques, is that the MWCNT electronic structure under 3 eV present structured peaks as the Van Hove Singularities.

5 The potentials of pump-probe technique with variable pump photon energy is evidenced also by the discussion on HOPG. New results are presented concerning the band gap renormalization on this system.

Thus different CNT architectures clearly reveal different optical responses. Concerning the vertically and horizontally aligned architectures, two different excitonic processes have been evidenced and studied, i.e. linear (photobleaching and photoabsorption) and non-linear (exciton-exciton annihilation) processes. In particular in horizontally aligned MWCNT, controlling the light polarization direction with respect to the CNT long-axis, we are able to select and unveil different optical responses, evidencing linear rather than non-linear effects. The exciton-exciton annihilation non-linear processes can reveal other non-linear effects as Multiple Exciton Generation [10]. In this thesis the possible presence of MEG has been studied in MWCNT.

Concerning the experimental techniques, the time resolved optical measurements represent a powerful tool, able to grasp the excitonic dynamics in the femtosecond time domain. Time resolved reflectivity measurements ($\Delta R/R$) have been performed on unaligned SWCNT (chapter 3) and on HOPG (chapter 7). Time resolved transmittivity measurements ($\Delta T/T$) have been realized on horizontally aligned MWCNT (chapter 4 and chapter 6) and on vertically aligned SWCNT and MWCNT (chapter 5). These $\Delta R/R$ or $\Delta T/T$ measurements have been made with different time resolved techniques: monochromatic (1.55 eV) pump and probe; pump photon energy at 1.55 eV and supercontinuum as a probe; variable pump photon energies ranging from 0.8 eV to 4.1 eV and probe photon energy at 1.55 eV; IPCE on MWCNT.

The dynamics of charge transfer and of exciton interaction studied in this thesis are of crucial importance for several technological applications based on the CNT, ranging from energy storage, sensor devices, bio-medical engineering and photovoltaic technology.
Concerning this last field, the results here obtained represent an improvement in the knowledge of systems, which are very promising in photovoltaic applications, as discussed in the literature in the last years. In particular the analysis concerning the MWCNT is a meaningful result. In fact MWCNT, with high conductivity and high absorption efficiency, are main actors in the struggle for solar device improvements. Revealing the excitonic character, understanding the conditions for which a MEG can be realized and studying the underlying mechanism are key points in order to enhance the efficiency of photovoltaic devices based on MWCNT.

The study of different CNT architectures represents the first step of a wide project. The second step has already started and consists of the study of heterogeneous systems, in which the different CNT architectures are combined with nanoparticles or organic groups. Starting from the basic systems and adding, in subsequent steps, the different components up to the complete devices, our goal, in collaboration with international research groups, is to consider, for each step, the response in optical and photoemission measurements.
The first goal is to study unaligned SWCNT and MWCNT, combined with metal nanoparticles. These systems have already demonstrated very promising properties in photovoltaic response. Preliminary measurements have been performed in our laboratories. Interesting results have been obtained also on ZnO combined with unaligned SWCNT.
Then also the horizontally aligned MWCNT will be combined with metal nanoparticle and molecular groups will be deposited on the considered CNT architectures.
All the samples will be provided with metallic contacts, in order to perform also charge transport measurements.
The collaboration with theoretical groups enables to consider detailed models for a more complete analysis of the addressed issues.
In addition to the optical measurements, also time resolved and angular resolved photoemission measurements can be realized in our laboratory. This technique allows to obtain information about the electronic dynamics, the chemical bonding and the charge transfer processes. In particular the role of unoccupied states (as image states) at the interface between CNT and the other components of the heterogeneous systems will be explored. In general the time resolved photoemission spectroscopy will be very useful in order to analyze the interactions between the different components of heterogeneous systems.

In conclusion, in this project and therefore in this thesis, the effort to understand the fundamental dynamics of charge carrier interactions and the charge transfer processes is applied on samples increasingly similar to the solar cell devices. In fact we believe that a significant improvement on the photovoltaic research can be achieved only if a deeper understanding of the fundamental processes is realized, on the single components and then on the complete heterogeneous system at the basis of the photovoltaic device.

Ringraziamenti

Dire grazie per me è sempre stata questione molto seria. Anche se il fatto di pronunciare spesso questa parola potebbe far pensare a qualcuno che io la tratti in modo poco "attento": non è così. Anzi, quando la rigenero, quasi ogni volta penso al suo significato e ai motivi per cui mi sono permesso di farne uso. E così da lei sono rigenerato. All'inizio di questo anno 2012 è spirato un grande scrittore, sacerdote operaio della contemplazione, disarmato, come può esserlo un uomo di fede essenziale, per questo forte, come è chi cerca solo il vestito della misericordia, don Luisito Bianchi. Il giorno dopo la sua morte, una cara amica l'ha ricordato con alcune sue parole: ′La gratuità prende tutto... come un oceano infinito nel quale l'essere vive, respira, si bagna di gratuità... è la gratuità che presiede alla vita... Sì, la gratuità è la totalità, il principio e il termine, la vita... Tutti i nostri perché s'infrangono, si sciolgono contro di essa. È la sola parola che potrebbe racchiudere tutte le altre, mentre queste ultime, senza gratuità, perdono il loro significato originario. La gratuità è pace; una pace non gratuita non è vera. La gratuità è amore; senza di essa, l'amore è defraudato della sua dimensione più profonda. Potrei enumerare tutte quelle parole che sono indicatrici, per convenzione, di valori: giustizia, bellezza, onestà, gioia... Che ne è di esse senza la gratuità? ... una parola terribile che sovverte la vita′
(Luisito Bianchi, Dialogo sulla gratuità)
Ecco perchè per me la parola ′grazie′ è parola creatrice, perchè davvero la gratuità e il riconoscere la gratuità sono il senso della nostra esistenza, del nostro conoscere e lavorare e amare e incontrare.

Devo dire grazie a tante persone per questi anni di dottorato.

A Stefania, cara amica alla quale devo molto, devo la strada fatta insieme, devo ciò che mi ha insegnato con la sua bravura, la sua tenacia, il suo desiderio appassionato di competenza, la sua pronta intelligenza, devo ciò che abbiamo imparato insieme.
A Gabriele, cui mi legano forte stima e profonda riconoscenza, per la sua grandissima professionalità, la sua ampia cultura scientifica e non solo, la sua passione civile, che mi hanno inspirato in tutti questi anni. Ma la mia riconoscenza è anche perchè Gabriele e Sandra, così capace di relazioni umanamente profonde e vere, ci hanno fatto dono di un'amicizia intensa e gratuita, soprattutto in quei momenti, intensi e gratuiti, dolorosamente carichi di speranza, che hanno segnato la vita della mia famiglia negli ultimi anni.
A tanti giovani con cui ho lavorato, Stefano, Stefano, Andrea, Giovanni, Federico, Matteo e tanti altri. Da loro ho imparato molto, anche il fatto che il futuro del nostro paese può ancora essere raccontato grazie alla loro intelligenza e alla loro passione di conoscenza.
Alle persone del Dipartimento, Luigi, Claudio, Francesco, Luca, Fausto, Giuseppe, Angelo, Maurizio, Luca, Ernesto, Marco, Giovanna ... per il loro rigore, il loro impegno, che rendono il Dipartimento un laboratorio di progetti e di idee nella ricerca e un esempio di buona e seria didattica. Con alcuni di loro poi si tratta di amicizia e non si potrebbe chiedere di più ad un ambiente di lavoro: competenza da imparare e amicizia da sperimentare.
A tutte le persone che lavorano in Dipartimento; a Donatella e Cristina, perchè ogni segreteria con me deve avere pazienza e loro ne hanno, oltre che attenta precisione; a Paola, Roberta, Grazia, Michela perchè ci tengono al loro lavoro e la tazzina di caffè è più buona se accompagnata da due parole scambiate con gentilezza; a Morris, Roberto, Adriano per le discussioni sull'attualità e perchè si può capire, guardandoli, che cosa significa lavorare con cura.
A Fulvio, che mi volle qui a Brescia ormai tanti anni fa, anche per questo gli devo molto. Gli devo anche le riflessioni sulla vita e sul mondo che mi hanno aiutato e mi aiutano a pensare.
Tutti i grazie che devo e desidero dire, in realtà li porterò personalmente.

Ora chiedo a quelle poche persone che leggeranno queste righe, di avere ancora un attimo di pazienza, perchè vorrei usare queste pagine per considerazioni che mi stanno a cuore.

La mia vicenda è un poco particolare. Prima del dottorato lavoravo già

nel laboratorio di ricerca e contemporaneamente insegnavo in scuole superiori di Cremona. Dopo il dottorato farò lo stesso, lavorerò in laboratorio, continuando sul progetto iniziato in questi anni, e insegnerò al Liceo Scientifico di Cremona, la mattina a Cremona, il pomeriggio a Brescia. Insegnare è professione delicata, importante e difficile e non gode della giusta considerazione. Una società che non riconosce il ruolo centrale della professione docente, esercitata da adulti che, educando i più giovani, trasmettono e condividono sapere, è una società destinata a morire. Non tutti hanno attitudine (potrei quasi dire vocazione) per esercitare questa professione, poichè ogni professione richiede attitudini e disposizioni culturali e umane. Ho incontrato moltissimi colleghi di straordinario valore, che, spesso con spirito di volontariato, costruiscono esperienze bellissime e innovative e danno vita a percorsi didattici davvero intensi. Proprio per questo so che una condizione essenziale per trasmettere sapere educando è la formazione dei docenti. Ogni riforma del sistema scolastico dovrebbe partire da qui. Ai docenti deve essere data la possibilità e richiesto l'impegno (che molti già ora realizzano facendo salti mortali) di darsi i tempi opportuni per studiare e rinnovare le proprie conoscenze e le proprie motivazioni, non come optional, ma come condizione essenziale per fare il loro mestiere. Questi tempi di formazione non possono essere solo incastrati tra un consiglio e l'altro, o tra un pacco di compiti da correggere e l'altro, ma devono trovare i giusti periodi. Questo costa, si dirà. Certo, ma avere una scuola di qualità richiede investimenti, l'alternativa è la fine di una speranza di futuro per una nazione. Queste righe non serviranno per nulla a cambiare il corso delle scelte, ma sento il dovere di scriverle, perchè è necessario lavorare, in ogni occasione, per far crescere un sentire comune nell'intera società. Insieme ad auspicate, rinnovate e lungimiranti scelte politiche, è indispensabile infatti una società consapevole dell'importanza delle priorità e dei valori su cui fondare la convivenza.

La seconda riflessione riguarda l'università. Negli anni di lavoro presso il nostro Dipartimento (più di dieci ormai), ho visto competenze davvero alte, alta professionalità, grande impegno, idee nuove e volontà di realizzarle. Ma ho visto anche la fatica di un sistema di ricerca che non sa avere la giusta fiducia in se stesso e non sa fare scelte decise per il futuro. Prepara giovani di valore, poi chiede loro di fare esperienza all'estero, non tanto come scelta necessaria per costruire un curriculum internazionale, ma soprattutto come àncora di salvezza rispetto ad un vuoto di prospettive in Italia... E pochi

ricercatori vengono da altri paesi: per un ricercatore non italiano conviene lavorare con gli italiani all'estero, piuttosto che venire in Italia con poche risorse e pochi vantaggi. Progetti importanti sono pensati e strumenti di misura sono anche pronti ad essere usati, ma le persone per realizzare i progetti e permettere agli strumenti di indagare sistemi innovativi sono poche. Mancano persone, perchè mancano un sistema paese coeso, un sistema università forte, una cultura capace di capire quanto sia essenziale promuovere risorse intellettuali e competenze di ricerca, tagliando pensatezze burocratiche e liberando efficienza e creatività. Errori interni ed esterni al sistema universitario, inefficienze che vengono dal passato, posizioni di potere mal gestito, metalità e atteggiamenti da cambiare pesano su questa situazione, oggi più che mai, in un periodo di crisi così acuta. Oggi è necessario un deciso cambiamento, perchè su università e ricerca occorre investire prioritariamente per il futuro. Certo, anche questa seconda riflessione non servirà a nulla, ma ancora sento il dovere di farla, pur da un luogo così piccolo come sono queste pagine.

Penso ci attendano tempi molto difficili, complessi, forse bui, noi avremo bisogno di coraggio e di intelligenza, in particolare avremo bisogno di pensiero, che sappia immaginare il futuro, che sappia inventare e reinventare una convivenza secondo giustizia. Tutti i luoghi di pensiero e di formazione al pensiero hanno oggi una responsabilità acuta, quella di costruire idee e metterle al servizio di un bene condiviso, quella di formare coscienze di donne e uomini umanamente ricchi, di cittadini che conoscano il valore della responsabilità. Innanzitutto la scuola e l'università sono tra questi luoghi: occorre lavorare perchè siano all'altezza del loro compito.

Concludo con un ultimo grazie, inteso e profondo.
Innanzitutto a mia mamma, a mio papà, a mia sorella Cristina, per me modello di forza, saggezza e dedizione, e a mia zia Lina così generosa; verso di loro ho un debito infinito di affetto e di riconoscenza, che non riuscirò mai a saldare e di cui posso solo rendere grazie. Il mio grande desiderio è di provare ad essere per i miei figli, almeno un pò, ciò che i miei genitori sono per me.
Alla mia famiglia tutta, i miei suoceri, cognati e nipoti, perchè è porto sicuro e saldo.
Ad Anna, perchè se fossi anziano vorrei incontrare una fisioterapista così, se fossi bambino vorrei avere il suo sorriso che mi aiuta a crescere, se fossi malato vorrei poter stringere la sua mano, se fossi amico vorrei avere un'amica così.

Io sono suo sposo, lei è per me il profumo di eterno, quello che costruisco, lo costruiamo insieme.
A Marco e a Giovanni, perchè sono la mia speranza e il mio futuro e quando li guardo non potrei desiderare altro, sono figli, ma anche esempi per me e compagni di strada a cui mi affido, proprio mentre cerco di educare al cammino.
A Chiara Maria perchè è un fiore strabiliante con petali di entusiasmo e fragilità, di coraggio e tenerezza; ce ne prendiamo cura, ma in realtà è il suo fiore a bagnare la nostra esistenza con acqua e spirito, spirito di debolezza, acqua di essenzalità.
Alla sapienza, perchè conoscere e ricercare è davvero il senso di una vita.

Bibliography

[1] S. Reich, C. Thomsen, and J. Maultzsch. *Carbon Nanotubes. Basic Concepts and Physical Properties.* Wiley, 2004.

[2] L. Valkunas, Y-Z. Ma, and G. Fleming. Exciton-exciton annihilation in single-walled carbon nanotubes. *Physical Review B*, 73(11):115432–115443, March 2006.

[3] F. Wang, G. Dukovic, L. E. Brus, and T. Heinz. The optical resonances in carbon nanotubes arise from excitons. *Science (New York, N.Y.)*, 308(5723):838–41, May 2005.

[4] D. Eder. Carbon nanotube-inorganic hybrids. *Chemical reviews*, 110(3):1348–85, March 2010.

[5] A. I. Romanenko, O. B. Anikeeva, T. I. Buryakov, E. N. Tkachev, K. R. Zhdanov, V. L. Kuznetsov, I. N. Mazov, and a. N. Usoltseva. Electrophysical properties of multiwalled carbon nanotubes with various diameters. *Physica Status Solidi (B)*, 246(11-12):2641–2644, December 2009.

[6] P.V. Kamat. Meeting the Clean Energy Demand: Nanostructure Architectures for Solar Energy Conversion. *Journal of Physical Chemistry C*, 111(7):2834–2860, February 2007.

[7] M. Scarselli, C. Scilletta, F. Tombolini, P. Castrucci, M. Diociaiuti, S. Casciardi, E. Gatto, M. Venanzi, and M. De Crescenzi. Multiwall Carbon Nanotubes Decorated with Copper Nanoparticles: Effect on

the Photocurrent Response. *The Journal of Physical Chemistry C*, 113(14):5860–5864, April 2009.

[8] Ph. Avouris, Zh. Chen, and V. Perebeinos. Carbon-based electronics. *Nature nanotechnology*, 2(10):605–15, October 2007.

[9] S. Agrawal, M.S. Raghuveer, R. Ramprasad, and G. Ramanath. Multishell Carrier Transport in Multiwalled Carbon Nanotubes. *IEEE Transactions on Nanotechnology*, 6(6):722–726, November 2007.

[10] Sh. Wang, M. Khafizov, X. Tu, M. Zheng, and D.K. Todd. Multiple exciton generation in single-walled carbon nanotubes. *Nano letters*, 10(7):2381–6, July 2010.

[11] G. Galimberti, S. Pagliara, S. Ponzoni, S. Dal Conte, F. Cilento, G. Ferrini, S. Hofmann, M. Arshad, C. Cepek, and F. Parmigiani. The photoinduced charge transfer mechanism in aligned and unaligned carbon nanotubes. *Carbon*, 49(15):5246–5252, December 2011.

[12] S. Pagliara, G. Galimberti, S. Mor, M. Montagnese, G. Ferrini, M. S. Grandi, P. Galinetto, and F. Parmigiani. Photoinduced π-π^* band gap renormalization in graphite. *Journal of the American Chemical Society*, 133(16):6318–22, April 2011.

[13] J. M. Dudley, G. Genty, and S. Coen. *Reviews of Modern Physics*, 78:1135–1184, 2006.

[14] F. Cilento, C. Giannetti, G. Ferrini, S. Dal Conte, T. Sala, G. Coslovich, M. Rini, A. Cavalleri, and F. Parmigiani. Ultrafast insulator-to-metal phase transition as a switch to measure the spectrogram of a supercontinuum light pulse. *Applied Physics Letters*, 96(2):021102, 2010.

[15] M S Dresselhaus, G Dresselhaus, and Ph Avouris. Carbon Nanotubes.

[16] L. Perfetti, T. Kampfrath, F. Schapper, A. Hagen, T. Hertel, C. Aguirre, P. Desjardins, R. Martel, C. Frischkorn, and M. Wolf. Ultrafast Dynamics of Delocalized and Localized Electrons in Carbon Nanotubes. *Physical Review Letters*, 96(2):027401–027404, January 2006.

[17] T. Pichler, M. Knupfer, M. Golden, J. Fink, A. Rinzler, and R. Smalley. Localized and Delocalized Electronic States in Single-Wall Carbon Nanotubes. *Physical Review Letters*, 80(21):4729–4732, May 1998.

[18] C.D. Spataru, S. Ismail-Beigi, L.X. Benedict, and S.G. Louie. Quasiparticle energies, excitonic effects and optical absorption spectra of small-diameter single-walled carbon nanotubes. *Applied Physics A: Materials Science & Processing*, 78(8):1129–1136, May 2004.

[19] C. D. Spataru, S. Ismail-Beigi, L. Benedict, and S. Louie. Excitonic Effects and Optical Spectra of Single-Walled Carbon Nanotubes. *Physical Review Letters*, 92(7):077402–077405, February 2004.

[20] H. Zhao and S. Mazumdar. Electron-Electron Interaction Effects on the Optical Excitations of Semiconducting Single-Walled Carbon Nanotubes. *Physical Review Letters*, 93(15):157402–157405, October 2004.

[21] J. Lefebvre and P. Finnie. Excited excitonic states in single-walled carbon nanotubes. *Nano letters*, 8(7):1890–5, July 2008.

[22] O. Korovyanko, C.-X. Sheng, Z. Vardeny, A. Dalton, and R. Baughman. Ultrafast Spectroscopy of Excitons in Single-Walled Carbon Nanotubes. *Physical Review Letters*, 92(1):017403–017406, January 2004.

[23] C.-X. Sheng, Z. Vardeny, A. Dalton, and R. Baughman. Exciton dynamics in single-walled nanotubes Transient photoinduced dichroism and polarized emission. *Physical Review B*, 71(12):125427–125437, March 2005.

[24] A. Hagen, M. Steiner, M. Raschke, Ch. Lienau, T. Hertel, H. Qian, A. Meixner, and A. Hartschuh. Exponential Decay Lifetimes of Excitons in Individual Single-Walled Carbon Nanotubes. *Physical Review Letters*, 95(19):197401–197404, October 2005.

[25] T. Hertel, R. Fasel, and G. Moos. Charge-carrier dynamics in single-wall carbon nanotube bundles: a time-domain study. *Applied Physics A: Materials Science & Processing*, 75(4):449–465, October 2002.

[26] A. Hagen, G. Moos, V. Talalaev, and T. Hertel. Electronic structure and dynamics of optically excited single-wall carbon nanotubes. *Applied Physics A: Materials Science & Processing*, 78(8):1137–1145, May 2004.

[27] S. Reich, M. Dworzak, A. Hoffmann, C. Thomsen, and M. Strano. Excited-state carrier lifetime in single-walled carbon nanotubes. *Physical Review B*, 71(3):033402–033405, January 2005.

[28] F. Wang, G. Dukovic, L. E. Brus, and T.F. Heinz. Time-Resolved Fluorescence of Carbon Nanotubes and Its Implication for Radiative Lifetimes. *Physical Review Letters*, 92(17):177401–177404, April 2004.

[29] L. Lüer, J. Crochet, T. Hertel, G. Cerullo, and G. Lanzani. Ultrafast excitation energy transfer in small semiconducting carbon nanotube aggregates. *ACS nano*, 4(7):4265–73, July 2010.

[30] C. Manzoni, A. Gambetta, E. Menna, M. Meneghetti, G. Lanzani, and G. Cerullo. Intersubband Exciton Relaxation Dynamics in Single-Walled Carbon Nanotubes. *Physical Review Letters*, 94(20):207401–207404, May 2005.

[31] G. Ostojic, S. Zaric, J. Kono, M. Strano, V. Moore, R. Hauge, and R. Smalley. Interband Recombination Dynamics in Resonantly Excited Single-Walled Carbon Nanotubes. *Physical Review Letters*, 92(11):117402–117405, March 2004.

[32] Y-Z. Ma, J. Stenger, J. Zimmermann, S. M. Bachilo, R. E. Smalley, R. B. Weisman, and G. R. Fleming. Ultrafast carrier dynamics in single-walled carbon nanotubes probed by femtosecond spectroscopy. *The Journal of chemical physics*, 120(7):3368–73, February 2004.

[33] J-S. Lauret, C. Voisin, G. Cassabois, C. Delalande, Ph. Roussignol, O. Jost, and L. Capes. Ultrafast Carrier Dynamics in Single-Wall Carbon Nanotubes. *Physical Review Letters*, 90(5):057404–057407, February 2003.

[34] M. C. Beard, K. P. Knutsen, P. Yu, J. M. Luther, Q. Song, W. K. Metzger, R. J. Ellingson, and A. J. Nozik. Multiple exciton generation in colloidal silicon nanocrystals. *Nano letters*, 7(8):2506–12, August 2007.

[35] Y. Murakami and J. Kono. Existence of an upper limit on the density of excitons in carbon nanotubes by diffusion-limited exciton-exciton annihilation: Experiment and theory. *Physical Review B*, 80(3):035432–035441, July 2009.

[36] M. Bockrath. Single-Electron Transport in Ropes of Carbon Nanotubes. *Science*, 275(5308):1922–1925, March 1997.

[37] V. Derycke, R. Martel, J. Appenzeller, and Ph. Avouris. Carbon Nanotube Inter- and Intramolecular Logic Gates. *Nano Letters*, 1(9):453–456, September 2001.

[38] A. Rao, J. Chen, E. Richter, U. Schlecht, P. Eklund, R. Haddon, U. Venkateswaran, Y.-K. Kwon, and D. Tománek. Effect of van der Waals Interactions on the Raman Modes in Single Walled Carbon Nanotubes. *Physical Review Letters*, 86(17):3895–3898, April 2001.

[39] S. Reich, J. Maultzsch, C. Thomsen, and P. Ordejón. Tight-binding description of graphene. *Physical Review B*, 66(3):035412–035416, July 2002.

[40] F. Borondics, K. Kamarás, M. Nikolou, Z. H. Tanner D.B. Chen, and A.G. Rinzler. Charge dynamics in transparent single-walled carbon nanotube films from optical transmission measurements. *Physical Review B*, 74(4):045431–045436, July 2006.

[41] U. Venkateswaran, A.M. Rao, E. Richter, M. Menon, A. Rinzler, R.E. Smalley, and P.C. Eklund. Probing the single-wall carbon nanotube bundle: Raman scattering under high pressure. *Physical Review B*, 59(16):10928–10934, April 1999.

[42] D. Kahn and J. Lu. Vibrational modes of carbon nanotubes and nanoropes. *Physical Review B*, 60(9):6535–6540, September 1999.

[43] L. Henrard, E. Hernández, P. Bernier, and A. Rubio. Van der Waals interaction in nanotube bundles: Consequences on vibrational modes. *Physical Review B*, 60(12):R8521–R8524, September 1999.

[44] J. Kürti, G. Kresse, and H. Kuzmany. First-principles calculations of the radial breathing mode of single-wall carbon nanotubes. *Physical Review B*, 58(14):R8869–R8872, October 1998.

[45] P. Delaney, H. J. Choi, J. Ihm, S. G. Louie, and M. L. Cohen. Broken symmetry and pseudogaps in ropes of carbon nanotubes. *Nature*, 60(11):7899–7904, September 1999.

[46] Y-K. Kwon, S. Saito, and D. Tománek. Effect of intertube coupling on the electronic structure of carbon nanotube ropes. *Physical Review B*, 58(20):R13314–R13317, November 1998.

[47] L. Alvarez, A. Righi, T. Guillard, S. Rols, E. Anglaret, D. Laplaze, and J-L. Sauvajol. Resonant Raman study of the structure and electronic properties of single-wall carbon nanotubes. *Chemical Physics Letters*, 316(3-4):186–190, January 2000.

[48] X. Blase, L.X. Benedict, E.L. Shirley, and S.G. Louie. Hybridazation Effects and Metallicity in Small Radius Carbon Nanotubes. 72(12):1878–1881, 1994.

[49] M. Zheng and E. D. Semke. Enrichment of single chirality carbon nanotubes. *Journal of the American Chemical Society*, 129(19):6084–5, May 2007.

[50] S. Hofmann, R. Sharma, C. Ducati, G. Du, C. Mattevi, C. Cepek, M. Cantoro, S. Pisana, A. Parvez, F. Cervantes-Sodi, A. C. Ferrari, R. Dunin-Borkowski, S. Lizzit, L. Petaccia, A. Goldoni, and J. Robertson. In situ observations of catalyst dynamics during surface-bound carbon nanotube nucleation. *Nano letters*, 7(3):602–8, March 2007.

[51] Y-Z. Ma, L. Valkunas, S. Dexheimer, S. Bachilo, and G. Fleming. Femtosecond Spectroscopy of Optical Excitations in Single-Walled Carbon Nanotubes: Evidence for Exciton-Exciton Annihilation. *Physical Review Letters*, 94(15):157402–157405, April 2005.

[52] K. Kato, K. Ishioka, M. Kitajima, J. Tang, R. Saito, and H. Petek. Coherent phonon anisotropy in aligned single-walled carbon nanotubes. *Nano letters*, 8(10):3102–8, October 2008.

[53] Y. Murakami, E. Einarsson, T. Edamura, and Sh. Maruyama. Polarization Dependence of the Optical Absorption of Single-Walled Carbon Nanotubes. *Physical Review Letters*, 94(8):087402–087405, March 2005.

[54] Y. Hashimoto, Y. Murakami, S. Maruyama, and J. Kono. Anisotropic decay dynamics of photoexcited aligned carbon nanotube bundles. *Physical Review B*, 75(24):245408–245412, June 2007.

[55] K. Seibert. Femtosecond carrier dynamics in graphite. *Physical Review B*, 42(5):2842–2851, 1990.

[56] T. Hertel and G. Moos. Electron-phonon interaction in single-wall carbon nanotubes: A time-domain study. *Physical Review Letters*, 84(21):5002–5, May 2000.

[57] M.S. Dresselhaus, G. Dresselhaus, R. Saito, and A. Jorio. Raman spectroscopy of carbon nanotubes. *Physics Reports*, 409(2):47–99, March 2005.

[58] M. Lin. Optical spectra of single-wall carbon nanotube bundles. *Physical Review B*, 62(19):13153–13159, November 2000.

[59] H. Bao, X. Ruan, and T. S Fisher. Optical properties of ordered vertical arrays of multi-walled carbon nanotubes from FDTD simulations arrays of multi-walled carbon nanotubes from FDTD simulations. *Optics Express*, 18(6):6347–6359, October.

[60] B. Kozinsky and N. Marzari. Static Dielectric Properties of Carbon Nanotubes from First Principles. *Physical Review Letters*, 96(16):166801–166806, April 2006.

[61] J. Choi, S. M. Lee, Y. C. Choi, H. Y. Lee, and J.C. Jiang. Electronic band dispersion of vertically aligned multiwall carbon nanotubes. *Chemical Physics Letters*, 349(3-4):185–190, November 2001.

[62] Y-K. Kwon and D. Tománek. Electronic and structural properties of multiwall carbon nanotubes. *Physical Review B*, 58(24):R16001–R16004, December 1998.

[63] V. Zólyomi, J. Koltai, Á. Rusznyák, J. Kürti, Á. Gali, F. Simon, H. Kuzmany, Á. Szabados, and P. Surján. Intershell interaction in double walled carbon nanotubes: Charge transfer and orbital mixing. *Physical Review B*, 77(24):245403–245402, June 2008.

[64] P. Castrucci, C. Scilletta, S. Del Gobbo, M. Scarselli, L. Camilli, M. Simeoni, B. Delley, A. Continenza, and M. De Crescenzi. Light harvesting with multiwall carbon nanotube/silicon heterojunctions. *Nanotechnology*, 22(11):115701, March 2011.

[65] P. Castrucci, F. Tombolini, M. Scarselli, E. Speiser, S. Del Gobbo, W. Richter, M. De Crescenzi, M. Diociaiuti, E. Gatto, and M. Venanzi. Large photocurrent generation in multiwall carbon nanotubes. *Applied Physics Letters*, 89(25):253107, 2006.

[66] F. Shyu and M. Lin. Loss spectra of graphite related systems A multi wall carbon nanotube, a single wall carbon nanotube bundle,

and graphite layers. *Physical Review B*, 62(12):8508–8516, September 2000.

[67] M. E. Brennan, J. N. Coleman, A. Drury, B. Lahr, T. Kobayashi, and W. J. Blau. Nonlinear photoluminescence from van Hove singularities in multiwalled carbon nanotubes. *Optics letters*, 28(4):266–8, February 2003.

[68] A. Pratap, A. L. Shah, A. R. Singh, S. Pal, R. K. Tyagi, A. L. Dawar, P. Chaturvedi, S. Lamba, and M. Bal. Linear and non-linear optical transmission from multi-walled carbon nanotubes. *Journal of Materials Science*, 40(16):4185–4188, August 2005.

[69] Zh. Wang, Ch. Liu, H. Xiang, Zh. Li, Q. Gong, Y. Qin, Zh. Guo, and D. Zhu. Ultrafast third-order nonlinear optical response of two soluble multi-wall carbon nanotubes. *Journal of Physics D: Applied Physics*, 37(7):1079–1082, April 2004.

[70] M. Zamkov, N. Woody, B. Shan, Z. Chang, and P. Richard. Lifetime of Charge Carriers in Multiwalled Nanotubes. *Physical Review Letters*, 94(5):056803–056806, February 2005.

[71] Ph. Poncharal, C. Berger, Y. Yi, Z. L. Wang, and W. A. De Heer. Room Temperature Ballistic Conduction in Carbon Nanotubes. *Journal of Physical Chemical*, 16:12104–12118, 2002.

[72] C. Schönenberger, A. Bachtold, C. Strunk, J. Salvetat, and L. Forr. Interference and Interaction in multi-wall carbon nanotubes. *Applied Physics A*, 69:283–295, August 1999.

[73] S. Agrawal, M. S. Raghuveer, H. Li, and G. Ramanath. Defect-induced electrical conductivity increase in individual multiwalled carbon nanotubes. *Applied Physics Letters*, 90(19):193104, 2007.

[74] C. Ni and P.R. Bandaru. Enhanced optical absorption cross-section characteristics of multi-wall carbon nanotubes. *Carbon*, 47(12):2898–2903, October 2009.

[75] B. K. Sarker, M. Arif, P. Stokes, and S. I. Khondaker. Diffusion mediated photoconduction in multiwalled carbon nanotube films. *Journal of Applied Physics*, 106(7):074307, 2009.

[76] Q. Ngo, D. Petranovic, S. Krishnan, A.M. Cassell, Q. Ye, J. Li, M. Meyyappan, and C.Y. Yang. Electron Transport Through Metal Multiwall Carbon Nanotube Interfaces. *IEEE Transactions On Nanotechnology*, 3(2):311–317, June 2004.

[77] M. F. Lin, F. L. Shyu, and R. B. Chen. Optical properties of well-aligned multiwalled carbon nanotube bundles. *Physical Review B*, 61(20):14114–14118, 2000.

[78] Y-Z. Ma, T. Hertel, Z. V. Vardeny, G. R. Fleming, and L. Valkunas. Ultrafast Spectroscopy of Carbon Nanotubes. *Topics Applied Physics*, 111:321–352, 2008.

[79] K. Jiang, Q. Li, and S. Fan. Spinning continuous carbon nanotube yarns. *Nature*, 419:801, 2002.

[80] Garcia Vidal. Effective medium theory of the optical properties of aligned carbon nanotubes. *Physical Review Letters*, 78:4289–4292, 1997.

[81] A. Gambetta, C. Manzoni, E. Menna, M. Meneghetti, G. Cerullo, G. Lanzani, S. Tretiak, A. Piryatinski, A. Saxena, R. L. Martin, and A. R. Bishop. Real-time observation of nonlinear coherent phonon dynamics in single-walled carbon nanotubes. *Nature Physics*, 2(8):515–520, July 2006.

[82] S.I. Anisimov, B.L. Kapeliovich, and T.L. Perelman. Electron emission from metal surfaces exposed to ultrashort laser pulses. *Sov. Phys. JETP*, pages 375–77.

[83] W. Lü, J. Dong, and Z-Y. Li. Optical properties of aligned carbon nanotube systems studied by the effective-medium approximation method. *Physical Review B*, 63(3):033401–033404, December 2000.

[84] F. Carbone, P. Baum, P. Rudolf, and Ah. Zewail. Structural Preablation Dynamics of Graphite Observed by Ultrafast Electron Crystallography. *Physical Review Letters*, 100(3):035501–035504, January 2008.

[85] M. Damnjanović, I. Milošević, T. Vuković, and R. Sredanović. Full symmetry, optical activity, and potentials of single-wall and multiwall nanotubes. *Physical Review B*, 60(4):2728–2739, July 1999.

[86] A. Srivastava and J. Kono. Diffusion-limited exciton-exciton annihilation in single-walled carbon nanotubes: A time-dependent analysis. *Physical Review B*, 79(20):205407–205413, May 2009.

[87] T. Hertel, V. Perebeinos, J. Crochet, K. Arnold, M. Kappes, and Ph. Avouris. Intersubband decay of 1-D exciton resonances in carbon nanotubes. *Nano letters*, 8(1):87–91, January 2008.

[88] G. Dukovic, F. Wang, D. Song, Y. Sferi, T. F. Heinz, and E. Brus. *Nano Letters*, 5:2314–2318, 2005.

[89] D. Song, F. Wang, G. Dukovic, M. Zheng, E. D. Semke, L. E. Brus, and T. F. Heinz. Direct Measurement of the Lifetime of Optical Phonons in Single-Walled Carbon Nanotubes. *Physical Review Letters*, 100(22):225503–225506, June 2008.

[90] A. E. Aliev, M. H. Lima, E. M. Silverman, and R. H. Baughman. Thermal conductivity of multi-walled carbon nanotube sheets: radiation losses and quenching of phonon modes. *Nanotechnology*, 21(3):035709, January 2010.

[91] G. Ostojic, S. Zaric, J. Kono, V. Moore, R. Hauge, and R. Smalley. Stability of High-Density One-Dimensional Excitons in Carbon Nanotubes under High Laser Excitation. *Physical Review Letters*, 94(9):097401–097404, March 2005.

[92] A. Shabaev, A. L. Efros, and A. J. Nozik. Multiexciton generation by a single photon in nanocrystals. *Nano letters*, 6(12):2856–63, December 2006.

[93] J. A. McGuire, J. Joo, J. M. Pietryga, R. D. Schaller, and V. I. Klimov. New aspects of carrier multiplication in semiconductor nanocrystals. *Accounts of chemical research*, 41(12):1810–9, December 2008.

[94] G. Nair, S. Geyer, L-Y. Chang, and M. Bawendi. Carrier multiplication yields in PbS and PbSe nanocrystals measured by transient photoluminescence. *Physical Review B*, 78(12):125325–125334, September 2008.

[95] L. Marty, E. Adam, L. Albert, R. Doyon, D. Ménard, and R. Martel. Exciton Formation and Annihilation during 1D Impact Excitation of Carbon Nanotubes. *Physical Review Letters*, 96(13):136803–136806, April 2006.

[96] R. D. Schaller, V. M. Agranovich, and V. I. Klimov. High-efficiency carrier multiplication through direct photogeneration of multi-excitons via virtual single-exciton states. *Nature Physics*, 1(3):189–194, November 2005.

[97] W. Andreoni. *The Physics of Fullerene-Based and Fullerene-Related Materials*. Dordrecht, 2000.

[98] D. Li and R. B. Kaner. Materials science. Graphene-based materials. *Science (New York, N.Y.)*, 320(5880):1170–1, May 2008.

[99] Th. E. Weller, M. Ellerby, S. S. Saxena, R. P. Smith, and N. T. Skipper. Superconductivity in the intercalated graphite compounds C6Yb and C6Ca. *Nature Physics*, 1(1):39–41, September 2005.

[100] A. K. Geim. Graphene: status and prospects. *Science (New York, N.Y.)*, 324(5934):1530–4, June 2009.

[101] F. Carbone, Oh-H. Kwon, and Ah. H. Zewail. Dynamics of chemical bonding mapped by energy-resolved 4D electron microscopy. *Science (New York, N.Y.)*, 325(5937):181–4, July 2009.

[102] J. Kanasaki, E. Inami, K. Tanimura, H. Ohnishi, and K. Nasu. Formation of sp3-Bonded Carbon Nanostructures by Femtosecond Laser Excitation of Graphite. *Physical Review Letters*, 102(8):087402–087405, February 2009.

[103] K. R. Raman, Y. Murooka, Ch-Y. Ruan, T. Yang, S. Berber, and D. Tománek. Direct Observation of Optically Induced Transient Structures in Graphite Using Ultrafast Electron Crystallography. *Physical Review Letters*, 101(7):077401–077404, August 2008.

[104] Fabrizio Carbone, Brett Barwick, Oh-Hoon Kwon, Hyun Soon Park, J. Spencer Baskin, and Ahmed H. Zewail. EELS femtosecond resolved in 4D ultrafast electron microscopy. *Chemical Physics Letters*, 468(4-6):107–111, January 2009.

[105] A. Acocella, F. Carbone, and F. Zerbetto. Quantum study of laser-induced initial activation of graphite-to-diamond conversion. *Journal of the American Chemical Society*, 132(35):12166–7, September 2010.

[106] S. Tatar, R.C.and Rabii. Electronic properties of graphite: A unified theretical study. *Physical Review B*, 25(6):4126, 1982.

[107] S. K. Sundaram and E. Mazur. Inducing and probing non-thermal transitions in semiconductors using femtosecond laser pulses. *Nature materials*, 1(4):217–24, December 2002.

[108] A. Cavalleri, Cs. Tóth, C. Siders, J. Squier, F. Ráksi, P. Forget, and J. Kieffer. Femtosecond Structural Dynamics in VO2 during an Ultrafast Solid-Solid Phase Transition. *Physical Review Letters*, 87(23):237401–237404, November 2001.

[109] M. Rini, R. Tobey, N. Dean, J. Itatani, Y. Tomioka, Y. Tokura, R. W. Schoenlein, and A. Cavalleri. Control of the electronic phase of a manganite by mode-selective vibrational excitation. *Nature*, 449(7158):72–4, September 2007.

[110] Matthieu Chollet, Laurent Guerin, Naoki Uchida, Souichi Fukaya, Hiroaki Shimoda, Tadahiko Ishikawa, Kazunari Matsuda, Takumi Hasegawa, Akira Ota, Hideki Yamochi, Gunzi Saito, Ryoko Tazaki, Shin-Ichi Adachi, and Shin-Ya Koshihara. Gigantic photoresponse in 1/4-filled-band organic salt (EDO-TTF)2PF6. *Science (New York, N.Y.)*, 307(5706):86–9, January 2005.

[111] G. Sciaini, H. Maher, S. G. Kruglik, Th. Payer, Ch. T. Hebeisen, F-J. M. zu Heringdorf, M. Yamaguchi, M. Horn-von Hoegen, R. Ernstorfer, and R. J. D. Miller. Electronic acceleration of atomic motions and disordering in bismuth. *Nature*, 458(7234):56–9, March 2009.

[112] K. F. Berggren and B. E. Sernelius. *Physical Review B*, 24:1971, 1981.

[113] H. Kalt. Band gap renormalization in semiconductors with multiple inequivalent valleys. *Physical Review B*, 45(3):1139–1154, 1992.

[114] A. Kim, J. Callan, C. Roeser, and E. Mazur. Ultrafast dynamics and phase changes in crystalline and amorphous GaAs. *Physical Review B*, 66(24):245203–245215, December 2002.

[115] Fabrizio Carbone. The interplay between structure and orbitals in the chemical bonding of graphite. *Chemical Physics Letters*, 496(4-6):291–295, August 2010.

[116] M. Breusing, C. Ropers, and Th. Elsaesser. Ultrafast Carrier Dynamics in Graphite. *Physical Review Letters*, 102(8):086809–086812, February 2009.

[117] R. Saito, A. Jorio, A. G. Souza Filho, G. Dresselhaus, M. S. Dresselhaus, and M. A. Pimenta. Probing Phonon Dispersion Relations of Graphite by Double Resonance Raman Scattering. *Physical Review Letters*, 88(2):027401–027404, December 2002.

[118] J. Maultzsch, S. Reich, C. Thomsen, H. Requardt, and P. Ordejón. Phonon Dispersion in Graphite. *Physical Review Letters*, 92(7):075501–075504, February 2004.

[119] Greenaway, D.L. and Harbeke, G. and Bassani, F. and Tosatti, E. Anisotropy of the Optical Constants and the Band Structure of Graphite. *Physical Review*, 178(3):1340–1348, 1969.

[120] A. B. Djurisic and E. H. Li. *Journal of Applied Physics*, 85:7404, 1999.

[121] R. Ahuja, S. Auluck, J. M. Wills, M. Alouani, B. Johansson, and O. Eriksson. Optical properties of graphite from first-principles calculations. *Physical Review B*, 55(8):4999–5005, 1997.

[122] G. Moos, C. Gahl, R. Fasel, M. Wolf, and T. Hertel. Anisotropy of Quasiparticle Lifetimes and the Role of Disorder in Graphite from Ultrafast Time-Resolved Photoemission Spectroscopy. *Physical Review Letters*, 87(26):267402–267405, December 2001.

[123] F. Wooten. *Optical Properties of Solids*. Academic Press inc.: New York, 1972.

[124] C. D. Spataru, M. A. Cazalilla, A. Rubio, L. X. Benedict, P. M. Echenique, and S. G. Louie. Anomalous Quasiparticle Lifetime in Graphite: Band Structure Effects. *Physical Review Letters*, 87(24):246405–246408, November 2001.

[125] T. Kampfrath, L. Perfetti, F. Schapper, Ch. Frischkorn, and M. Wolf. Strongly Coupled Optical Phonons in the Ultrafast Dynamics of the Electronic Energy and Current Relaxation in Graphite. *Physical Review Letters*, 95(18):187403–187406, October 2005.